EFFECT OF TEMPERATURE AND STEAM ENVIRONMENT ON FATIGUE BEHAVIOR OF AN OXIDE-OXIDE CONTINUOUS FIBER CERAMIC COMPOSITE

THESIS

Chalene A. Eber, First Lieutenant, USAF

AFIT/GA/ENY/05-M09

DEPARTMENT OF THE AIR FORCE
AIR UNIVERSITY

AIR FORCE INSTITUTE OF TECHNOLOGY

Wright-Patterson Air Force Base, Ohio

The views expressed in this thesis are those of the author and do not reflect the official policy or position of the United States Air Force, Department of Defense, or the U.S. Government.

AFIT/GA/ENY/05-M09

EFFECT OF TEMPERATURE AND STEAM ENVIRONMENT ON FATIGUE BEHAVIOR OF AN OXIDE-OXIDE CONTINUOUS FIBER CERAMIC COMPOSITE

THESIS

Presented to the Faculty

Department of Aeronautical and Astronautical Engineering

Graduate School of Engineering and Management

Air Force Institute of Technology

Air University

Air Education and Training Command

In Partial Fulfillment of the Requirements for the

Degree of Master of Science in Astronautical Engineering

Chalene A. Eber, BS

First Lieutenant, USAF

March 2005

AFIT/GA/ENY/05-M09

EFFECT OF TEMPERATURE AND STEAM ENVIRONMENT ON FATIGUE BEHAVIOR OF AN OXIDE-OXIDE CONTINUOUS FIBER CERAMIC COMPOSITE

Chalene A. Eber, BS

First Lieutenant, USAF

Approved:

_____/signed/_____	_____
Dr. Marina B. Ruggles-Wrenn (Chairman)	Date
_____/signed/_____	_____
Dr. Shankar Mall (Member)	Date
_____/signed/_____	_____
Dr. Theodore Nicholas (Member)	Date

Abstract

Aerospace components require structural materials that have superior long-term mechanical properties and can be exposed to severe environmental conditions, such as ultra-high temperature, high pressure, or water vapor. Ceramic-matrix composites (CMCs), capable of maintaining excellent strength and fracture toughness at high temperatures, continue to attract attention as candidate materials for aerospace applications. This research effort investigates fatigue behavior of an oxide-oxide continuous fiber ceramic composite (CFCC) consisting of a porous alumina matrix reinforced with laminated, woven mullite/alumina fibers (Nextel 720) at 1200 and 1330°C in laboratory air and in 100% steam environments. This composite has no interface between the fiber and matrix, and relies on the porous matrix for flaw tolerance. Tension-tension fatigue behavior was studied for fatigue stresses ranging from 100 to 170 MPa at 1200°C, and for fatigue stresses of 50 and 100 MPa at 1330°C. At 1200°C, the CFCC exhibited excellent fatigue resistance in laboratory air. However, the presence of steam caused noticeable degradation in fatigue performance at 1200°C. Fatigue resistance at 1330°C was poor. Results demonstrate that effects of steam environment on fatigue performance cannot be neglected.

Dedication

I dedicate this thesis to my husband for the love and patience he showed me throughout this process and for encouraging me to spend the necessary time to complete it.

Acknowledgements

I would like to express appreciation to my faculty advisor, Dr. Marina Ruggles-Wrenn, for her guidance and support throughout the course of this thesis effort. Her insight and timely help was invaluable. I am also grateful for the help and insight of my fellow student Captain Lee Harlan, and for the assistance of the lab technicians.

Chalene A. Eber

Table of Contents

Page

Page

List of Figures

Figure Page

Figure Page

Figure Page

Figure Page

List of Tables

EFFECT OF TEMPERATURE AND STEAM ENVIRONMENT ON FATIGUE BEHAVIOR OF AN OXIDE-OXIDE CONTINUOUS FIBER CERAMIC COMPOSITE

I. Introduction and Background

Advanced aerospace applications are driving the development of new materials to meet their specific requirements. These requirements include the capability to maintain mechanical properties at elevated temperatures and in oxidizing environments. Reusable space launch vehicles and turbine engine components, such as combustor walls and nozzle flaps, motivate new development (25:214; 29:410). Required characteristics of a potential material for these applications include low density, good oxidation resistance and high strength at high temperature, and avoidance of the brittle nature of monolithic ceramics (3:139, 14:503). Continuous fiber ceramic composites are attracting attention as candidate materials for use in these aerospace applications due to their non-catastrophic failure and capacity to maintain strength and fracture toughness in high temperature environments (2:451, 32:159, 37:70).

Despite the demonstrated capability of ceramic matrix composites (CMCs) to maintain strength in high temperature environments, the anticipated service requirements demand more than simple mechanical loading at high temperatures. One example of the more complex environments in which they are used is that of a typical reusable rocket engine turbopump rotor, which would expose the CMC to hydrogen, oxygen, and steam at high pressure (33:1536). Another example is a gas-turbine combustion environment, which would expose the CMC to ultra-high temperatures, high pressure, and as much as 10% water vapor (8:951). When mechanical loading is applied, microcracking and fiber/matrix debonding occur, exposing the load-bearing fibers in the composite to the destructive conditions present in these service environments (15:1720). Because these applications require exposing the CMCs to oxidizing environments, it is important to consider oxidation resistance in design and selection of CMCs.

Oxidation limits the service life of many components that are exposed to steam and is the primary mechanism of environmental degradation in CMCs. Because oxidation has such an effect on performance, significant effort has been invested in developing CMCs that will not degrade in humid environments.

Many damage-tolerant CMCs rely on a “weak” interphase between the fibers and the matrix. The purpose of the interphase is to produce debonding of the fiber from the matrix resulting in increased toughness (36:327). However, there is a limited choice of interphase materials (31:417). In some early CMC systems, the weak fiber/matrix interface contained carbon, but the carbon layer can be easily oxidized in high-temperature and humid environments (37:70). In an effort to reduce the problems

associated with oxidation, fiber coatings were applied. The most common fiber coating attempted was monolithic boron nitride (12:393, 37:70). Unfortunately, this was not sufficiently effective because once matrix cracking occurred, the oxidation process was accelerated due to the exposure of the interphase to the corrosive environmental conditions (17:1797, 36:327). Boron nitride (BN) oxidizes to a liquid oxide (B_2O_3) above 450°C and in the presence of water vapor a further reaction results in SiO_2 glass where the BN had been. This weakens the mechanical properties of the composite due to the degradation of the fiber properties and because the BN interphase has been replaced with the brittle SiO_2 glass (13:1473, 21:2777).

Numerous studies have focused on the performance of silicon carbide (SiC) composites in combustion environments (7, 11, 20-24). However, SiC/SiC is an example of a CMC that employs BN as an interphase layer between the fiber and matrix, which embrittles and weakens the composite as previously discussed. Silicon Carbide CMCs have been tested in turbine components, and accelerated degradation is observed after just a few hours of hot time. This has been attributed to oxidation of the fibers and the BN fiber coatings in the moist environment (38:1282).

A current approach to overcoming the limitations caused by oxidation is to use an all-oxide based composite (25:212). Oxide-oxide CMCs are inherently oxidation-saturated, so they are chemically stable in oxidative and corrosive environments (2:451, 6:63). By using a material that is not subject to the weakening effects of oxidation, the environmental degradation can be minimized. Because the fibers are already oxidized, microcracking in the matrix does not cause the fibers to be weakened by their exposure to

steam. These oxide-oxide CMCs do not require an interphase (typically the weakest link in oxidation resistance) to protect the fibers from oxidation, because their exposure to the moisture from the environment does not have the same detrimental effect (21:2777). Thus, oxide-oxide CMCs exhibit damage tolerance combined with inherent oxidation resistance (1:565).

Another key consideration in developing CMCs that exhibit high strength and fracture toughness, as well as non-catastrophic failure, is the fine, uniformly distributed porosity of the matrix. The microstructure must have low toughness to enable crack deflection through the matrix, yet maintain enough strength for interlaminar properties (19:2077, 37:71). In oxide-oxide CMCs, this porosity and a weak fiber/matrix interface (not requiring an interphase) allow the strong, brittle fibers to be isolated from each other and provide a path along which cracks can propagate without damaging the fibers. This eventually results in non-catastrophic failure (16:2333). In essence, the porosity creates a matrix that is already cracked, so increasing microcracking due to mechanical loading does not degrade the overall performance of the composite. The porosity allows the cracks to propagate along the fiber/matrix interface instead of through the fibers (9:607).

Previous oxide/oxide CMCs studied consisted of Nextel 610 or 720 fibers with a porous aluminosilicate matrix. These showed excellent fatigue performance in air up to 1100°C, but at greater temperatures a rapid decline in fatigue performance was observed, attributed to the oxidizing presence of silica in the matrix. This motivated the further development of an oxide/oxide material with a matrix that was all alumina and not aluminosilicate (30:695).

The material studied in this thesis, consisting of Nextel 720 fibers and a porous alumina matrix, resulted from a Small Business Innovative Research contract awarded to Composite Optics, Inc. (29:Sec 2, 28-29). This oxide-oxide material developed by Composite Optics, Inc. (COI) is a result of this search for materials that are not subject to the corrosive effects of steam (35:1628). The material is also being considered as a candidate for high temperature gas turbine components due to its potential to reduce NO_x and CO emissions, an advantage that is not further studied in this research effort (34:183, 38:1282).

The fibers of the N720/A studied in this effort are the commercially available Nextel 720 (manufactured by 3M Corporation). Levi, et al. investigated the performance of all-oxide ceramic composites with both Nextel 610 and Nextel 720 fibers. While the Nextel 610 fibers have higher strength and Young's modulus, the Nextel 720 fibers have greater stability against coarsening (19:2078). Antti, et al. suggests this leads to improved thermal stability (1:566).

Fatigue loading is an important test of strength because in the anticipated applications the material is subjected to cyclic loading situations. It characterizes performance in materials tested in a manner similar to their expected service life conditions (4:246-247). However, simple fatigue loading is not sufficient to determine the expected life of the components. As previously stated, anticipated applications also subject the material to ultra-high temperatures and a steam environment with repetitive loading.

To address the suitability of N720/A in any potential applications, it is necessary to develop a complete understanding of its mechanical properties. While the performance of N720/A at elevated temperature and with intermittent exposure to moisture has been investigated in the past, the effect of a constant steam environment has not been researched (38:1282). The objective of this study is to expand on current understanding by looking at how the presence of constant steam affects N720/A behavior at elevated temperature. Tension-tension fatigue performance of an oxide-oxide composite at elevated temperatures and in the presence of a 100% steam environment will be investigated.

II. Experimental Arrangements

2.1. Material and Specimen

The materiel studied in the thesis, Nextel 720/Alumina (N720/A), was developed by Ceramics Optics, Inc. (COI). It resulted from Small Business Innovative Research (SBIR) contract to develop a CMC for applications up to 1200°C (29:Sec 2, 28). The primary objective of the initiative was to develop an oxide matrix composite that would retain more than 90% of its original strength after 100 hours of exposure to 1200°C.

The matrix of the N720/A material is alumina, which is resistant to oxidation because it is already oxidized. The matrix is porous, allowing for crack deflection and longer durability, and for the load-bearing fibers to be isolated from damage caused by mechanical loading. The need for fiber coatings is eliminated because the N720/A relies on controlled matrix porosity for toughness (5).

Figure 1 shows a scanning electron microscope (SEM) micrograph of the Nextel 720/Alumina material showing the porous nature of the matrix. See Section 2.2.3 for background on the equipment used to obtain micrographs.

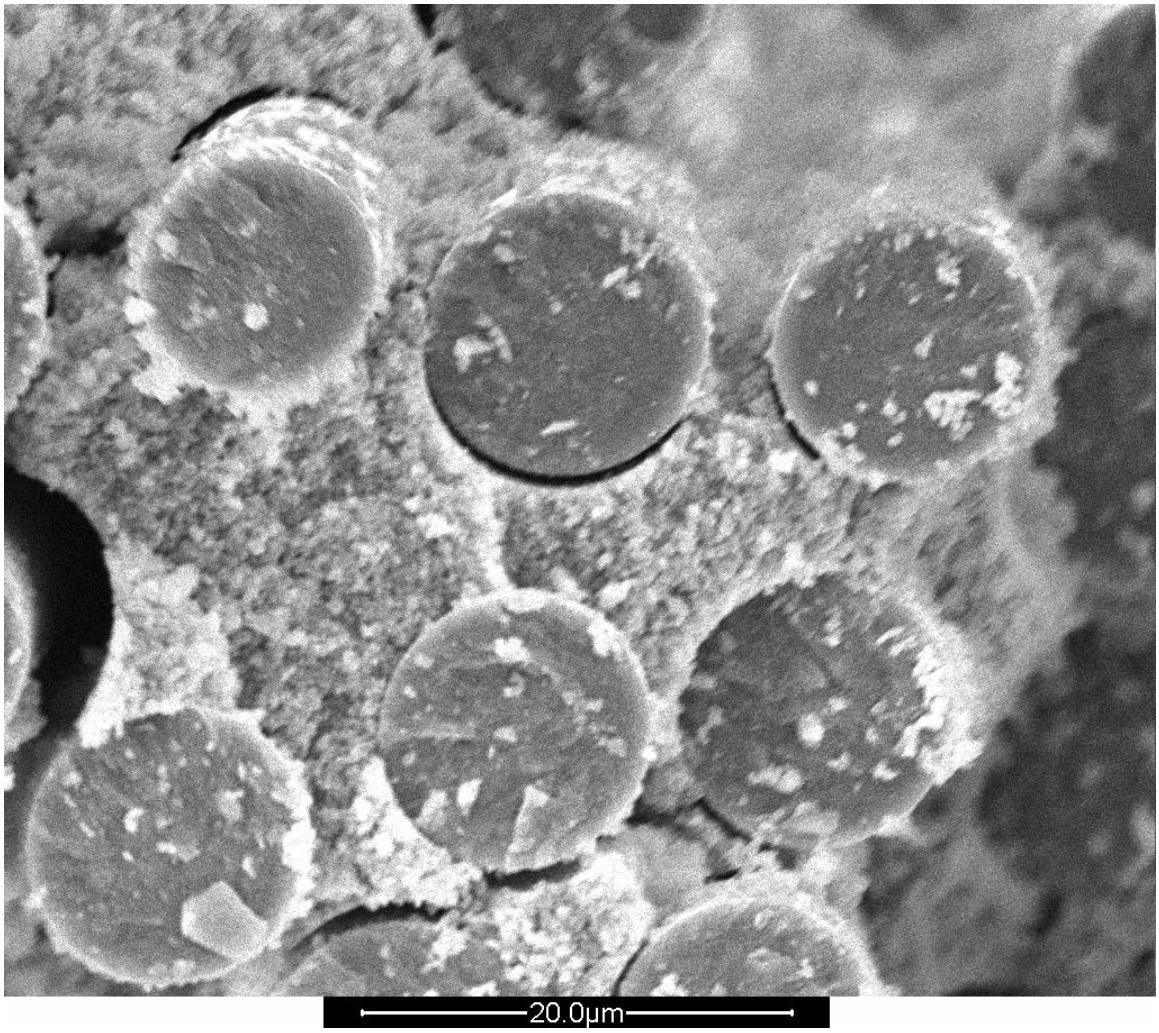

Figure 1. SEM micrograph of N720/A, showing porous matrix between fibers.

The continuous fibers in the oxide-oxide material used in this effort are the commercially available Nextel 720 fibers. These fibers are a mixture of fine-grained mullite ($3Al_2O_3 \cdot 2SiO_2$) and alumina, and serve as the principal load-bearing component of the CMC (16:2333, 19:2078).

The manufacturing process for N720/A is relatively low cost because it does not require pyrolysis steps or repetitive re-infiltration (5). The fiber is infiltrated into the matrix using a sol-gel process and dried under low pressure and low temperature,

resulting in pressureless sintering (1:567). Figure 2 shows a 0° fiber bundle infiltrated with the matrix material.

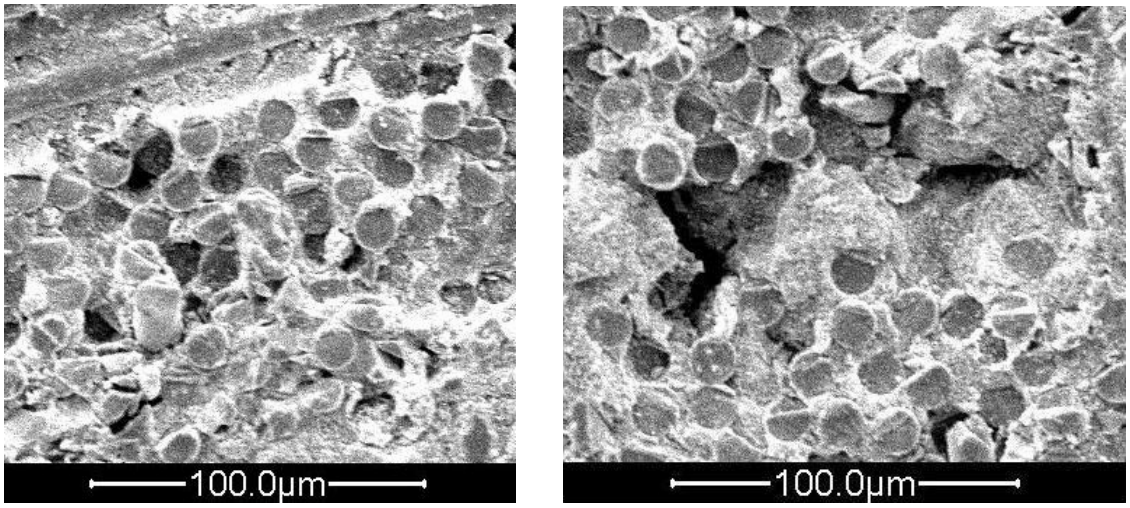

Figure 2. As-received material showing (a) successful infiltration in fiber bundle and (b) incomplete infiltration.

Figure 2a shows an area where matrix infiltration was successful. An area of incomplete infiltration is seen in figure 2b.

During the manufacturing process, shrinkage cracks are introduced during sintering, which are visible in the matrix of the untested material. These cracks are typically oriented perpendicular to the fibers (19:2080). Thus, the new material comes with inherent cracks. These shrinkage cracks are visible in the SEM micrograph shown in Figure 3. The cracks shown are oriented perpendicular to the fibers, in between the fiber tows.

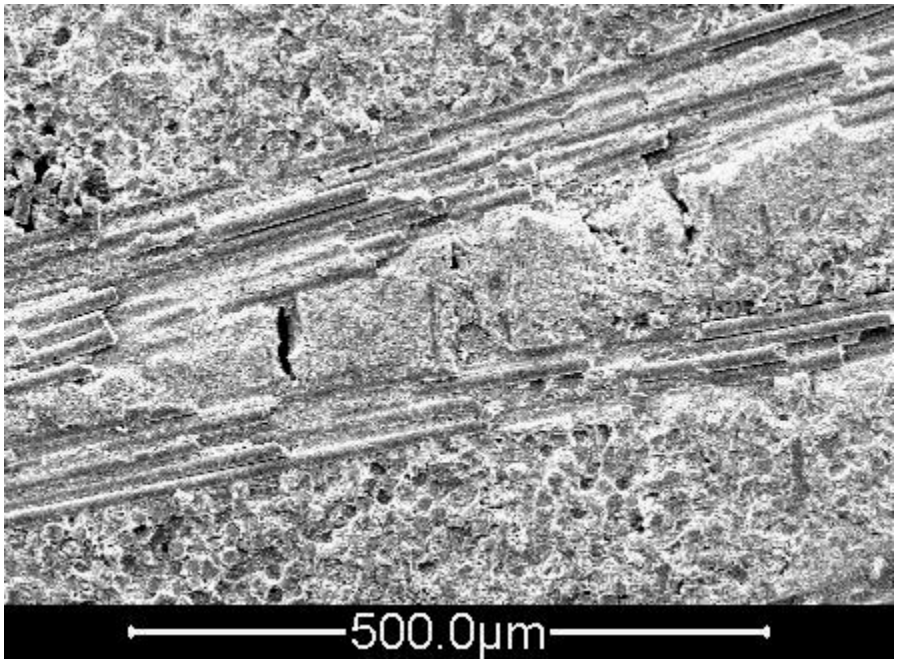

Figure 3. As-received material showing shrinkage cracks.

2.1.1. Specimen Preparation.

The N720/A material was provided in two panels, number 3342 and 3307-1, each consisting of 12 0°/90° woven layers. Panel thickness was 2.8 mm, with a porosity of ~24% and a fiber volume of ~44%. Specimens were machined to specifications shown in Figure 4.

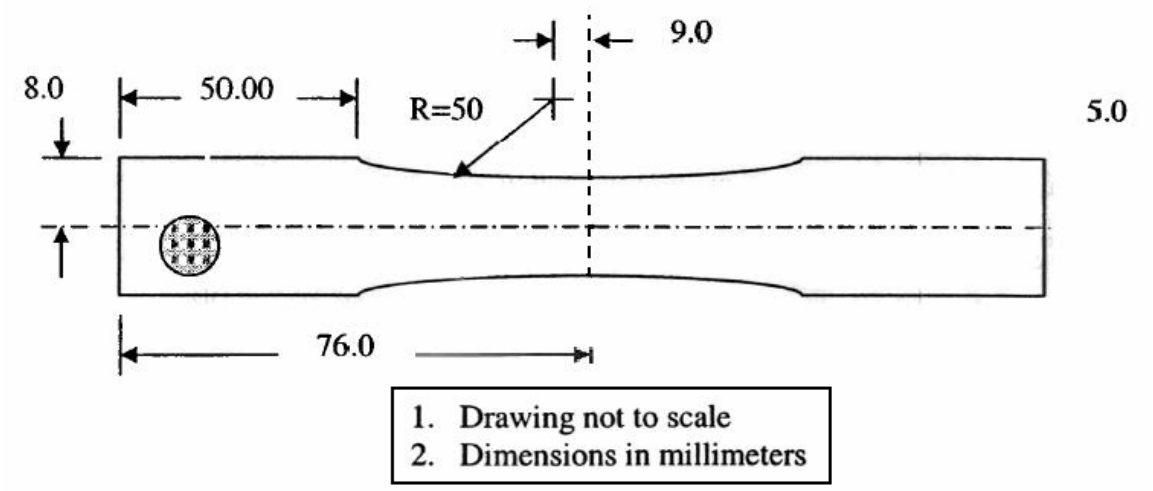

Figure 4. Tension-tension fatigue specimen, with cut-out showing fiber orientation.

The dogbone shape prevented grip failures and encouraged the failure to occur in the gage section, where the environmental conditions were applied.

The specimens were fit with fiberglass tabs to prevent grip failures or slipping. They were held in place by several drops of M-bond 200, manufactured by Measurements Group Inc.

Figure 5 shows one of the specimens used, with the fiberglass tabs bonded to the grip ends. The specimens were gripped at 600 psi. Neither grip failures nor specimen slipping occurred during this experimental investigation.

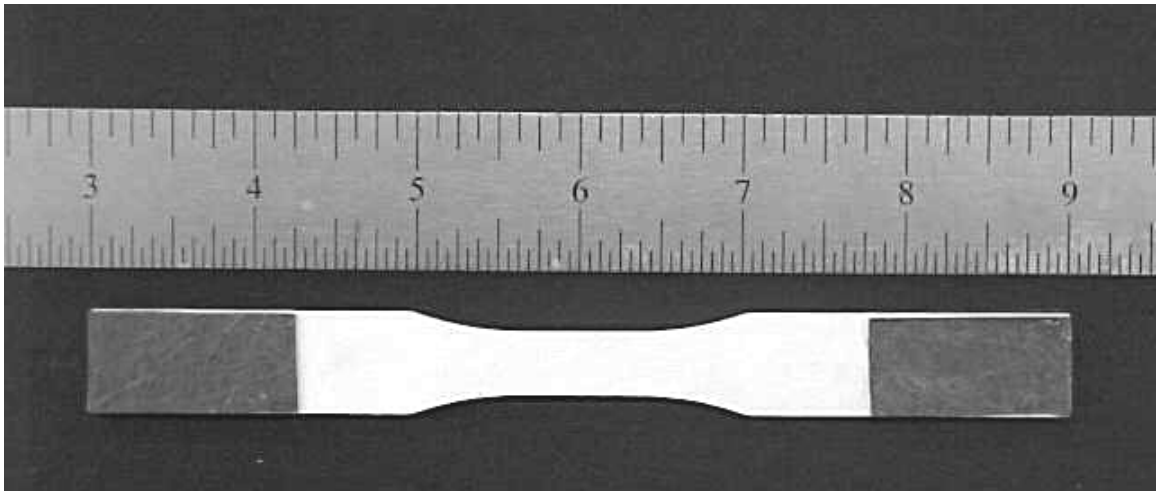

Figure 5. Nextel 720/A specimen with fiberglass tabs in place.

2.2. Testing and Characterization Equipment

2.2.1. Mechanical Testing Apparatus.

A 5 kip (5000 lb) MTS (MTS Systems Corporation) 810 Material Test System vertical servohydraulic machine with water-cooled hydraulic wedge type clamping grips were used. A grip pressure of 600 psi was used in all tests. The MTS Test Star II controller was used for input signal generation and data acquisition.

Standard MTS procedures and equipment were used to ensure and periodically verify grip alignment.

Strain measurement was accomplished with an MTS high-temperature extensometer, model #632.53E-14, with a gauge section of 0.5 in.

2.2.2. Environmental Control Equipment.

Testing at elevated temperatures was accomplished using an Amteco two-zone furnace. The furnace had two independently controlled zones, one on each side. The zones were each monitored using S type thermocouples. Figure 6 shows the experimental set-up.

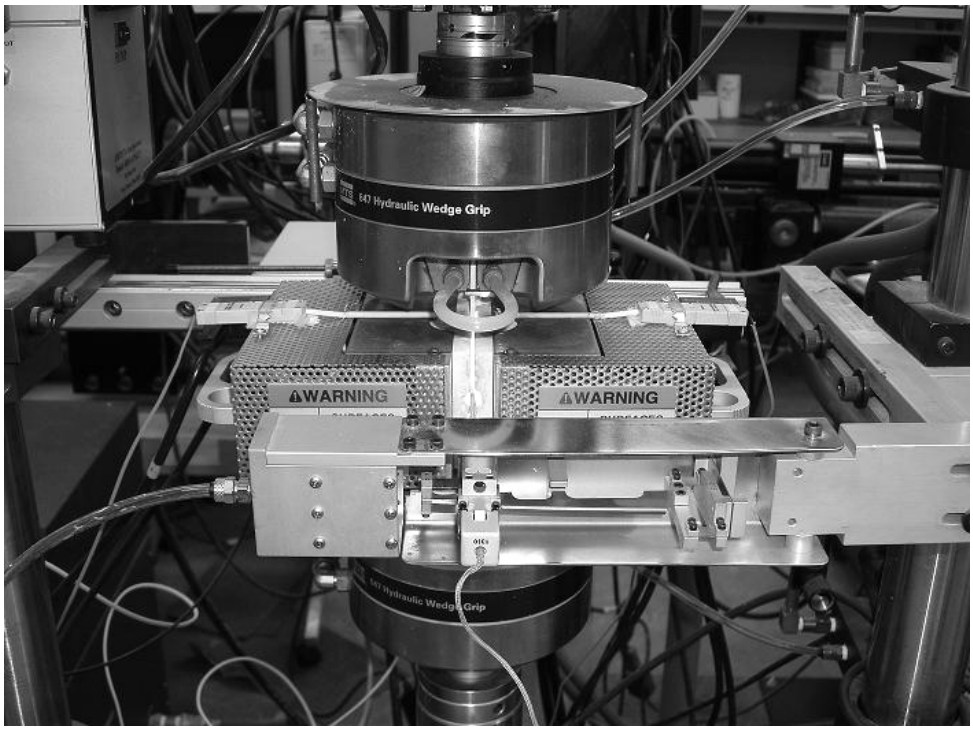

Figure 6. Experimental set-up.

In order to determine the temperature controller settings, one specimen was outfitted with two S type thermocouples. The thermocouples were attached directly to the specimen using Zircar Alumina Cement. The furnace temperature was raised in increments until the temperature of the specimen reached the desired test temperature. At that point, the controller settings were recorded and used in the tests. This procedure was

repeated for the steam conditions. For the duration of the tests, the temperature remained within ±3°C of the nominal temperature.

Tests at elevated temperature in the steam environment were accomplished using a steam generator and pump made by Amteco, Inc, model #HRFS-STMGEN, which was supplied with de-ionized water. Inside the oven was a susceptor, which served to create a more uniform environment immediately about the test specimen. Figure 7 shows the susceptor inside the oven. The extensometer rods are also visible.

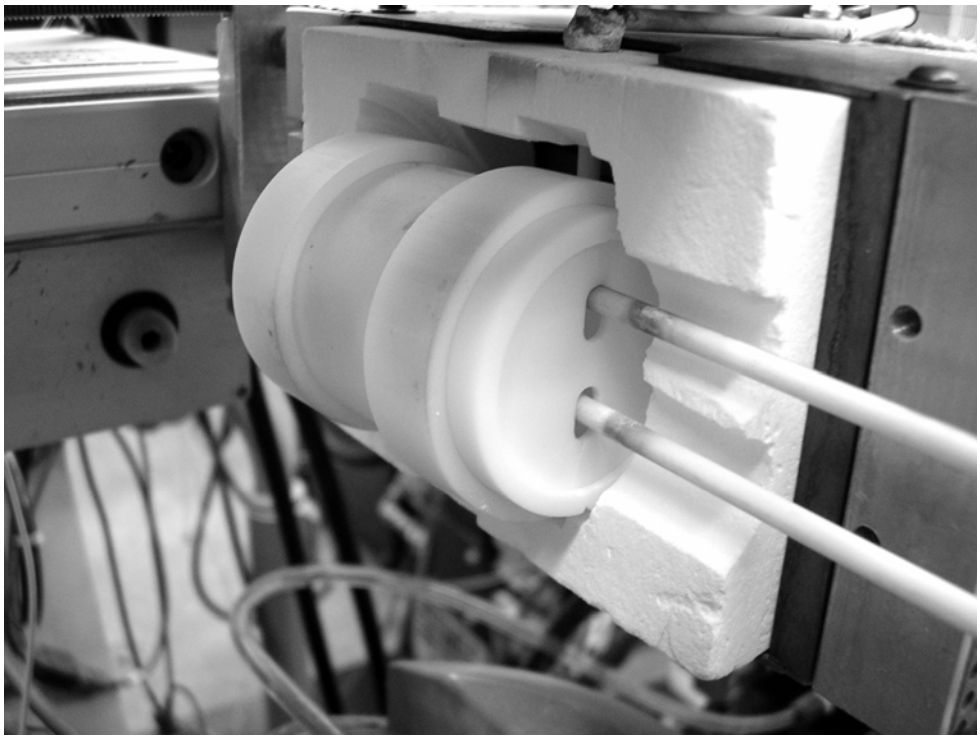

Figure 7. Susceptor inside oven, with extensometer rods visible.

The steam is fed directly into the susceptor through a tube. The susceptor is not sealed, thus creating a 100% steam environment as the dry air is forced out through the constant introduction of steam.

2.2.3. Microstructural Characterization.

To characterize the fracture surfaces, both an optical microscope and a scanning electron microscope (SEM) were used. The optical microscope was a Zeiss model Stemi SV II, and the SEM was a Quanta 200 manufactured by the FEI Company.

No preparation of the specimen was necessary to view the fracture surfaces under the optical microscope. To examine fracture surfaces under the SEM, further preparation was necessary. Because the CMC is non-conductive, specimens had to be coated with gold prior to viewing under the SEM. The fracture surface of the specimen was isolated using a diamond saw, a Buehler Isomet 1000. Following the cut, the specimen was sputter coated using a Spi-module Sputter Coater on the 110 second setting.

2.3. Test Procedures

In the 1200°C elevated temperature tests, the oven ramped up to the set point over a period of 25-30 min., and then was allowed to soak at temperature for 15 min. In the 1330°C elevated temperature tests, the oven ramped up in 35-50 min., and again allowed to soak at temperature for 15 min. Once the specimen was thermally equilibrated, thermal strain was measured and the coefficient of thermal expansion determined. The strain was re-zeroed prior to the mechanical test.

2.3.1. Monotonic Tension to Failure.

The tension tests were performed in displacement control with a constant rate of 0.05 mm/sec. Tension tests to failure were performed at 23, 1200, and 1330°C in laboratory air. No tension tests were conducted in the 100% steam environment.

2.3.2. Tension-Tension Fatigue Tests.

The tension-tension fatigue tests with an R ratio (minimum stress divided by the maximum stress) of 0.05 were performed in load control with the frequency of 1 Hz. Tension-tension fatigue tests were carried out at 1200 and 1330°C, in laboratory air and in 100% steam environments.

Fatigue run-out was defined as survival of 10^5 cycles at 1 Hz. Specimens which achieved run-out were subjected to a tensile test to failure to determine retained strength and stiffness. Environmental conditions of the fatigue test were maintained during measurement of retained properties. The test was conducted in the same manner as the monotonic tension test described in Section 2.4.1.

2.3.3. Data Collection

In all tests, time, segment number (1 segment = ½ cycle), displacement, temperature, strain, and load were measured and recorded. On the monotonic tension tests, data was collected at a rate of 20 Hz (20 data points per second). During the fatigue tests, the peak/valley data was collected for every cycle until failure. On selected cycles, the complete loop was recorded with the data collected at a rate of 32 Hz. These selected cycles included the first 25 cycles, and thereafter every 100^{th} cycle until cycle number

5000. From cycle 5000 to cycle 25,000, the complete loop was recorded for 500th cycle, and after 25,000 cycles the complete cycle was collected every 5000 cycles.

III. Results and Discussion

3.1. Chapter Overview

This chapter will outline the results that were obtained, and discuss the effects of temperature and steam on the performance of the Nextel 720/Alumina composite material. Section 3.2 discusses the thermal expansion of the material. Section 3.3 summarizes the results of the monotonic tests to failure. Section 3.4 outlines the results of the tension-tension fatigue tests conducted in laboratory air at elevated temperatures, and is followed by section 3.5, which compares the laboratory-air results to those obtained in the 100% steam environment at elevated temperatures. Section 3.6 examines the microstructure of the fracture surfaces of the failed specimens

3.2. Thermal Expansion

Nine tests were carried out at 1200°C and six tests at 1330°C. In each high-temperature test, thermal strain was recorded at the conclusion of the heating stage. Thermal strain measurements were used to determine the linear thermal expansion coefficient of the material. Thermal expansion results are summarized in Table 1, where test temperature, corresponding thermal strain and coefficient of linear thermal expansion

are presented for most specimens tested. Expansion of the extensometer extension rods contributes to the total measured strain, but it is expected that this contribution was negligible.

Table 1. Thermal Expansion of Nextel 720/A Composite between 23°C and Test Temperature

Test Temperature = 1200°C		
Specimen #	Thermal Strain (%)	α (10^{-6}/°C)
2	0.85	7.22
6	0.85	7.21
7	0.93	7.87
9	0.83	7.09
14	0.84	7.12
15	0.85	7.18
	Average	7.28
	Standard Deviation	0.29
Test Temperature = 1330°C		
Specimen #	Thermal Strain (%)	α (10^{-6}/°C)
3	0.96	7.32
4	1.02	7.82
10	1.00	7.63
11	0.99	7.57
	Average	7.59
	Standard Deviation	0.21

The coefficient of thermal expansion, α, obtained in the 1200°C tests compare well to that obtained in the 1330°C tests. These results are consistent with the coefficient of thermal expansion of 6.3×10^{-6}/°C, reported by the material manufacturer (COI).

3.3. Monotonic Loading

Results of monotonic tests are summarized in Table 2. Given in Table 2 are test temperature, elastic modulus, ultimate tensile strength (UTS), failure strain (ε_f), and failure location. It is noteworthy that all specimens failed within the extensometer gage section.

Table 2. Summary of Monotonic Tension Test Results

Specimen #	Temperature (°C)	E (GPa)	UTS (MPa)	ε_f (%)	Failure Location
1	23	66.8	168.8	0.35	gage section
2	1200	74.7	192.2	0.38	gage section
3	1330	33.4	118.4	1.43	gage section
4	1330	28.0	122.8	1.96	gage section

Results presented in Table 2 demonstrate a significant reduction, almost by a factor of two, in elastic modulus at 1330°C compared to that obtained at 1200°C. Ultimate tensile strength at 1330°C is likewise considerably lower than the UTS obtained at 1200°C. It should be noted that UTS obtained at 1200°C is greater than that produced at room temperature. Material exhibits improved strength and stiffness at 1200°C compared to room-temperature properties. Strength and stiffness data reported by the material manufacturer (COI) are presented in table 3 (5).

Table 3. Monotonic Tension Data Provided by COI

Temperature (°C)	E (GPa)	UTS (MPa)	ε_f (%)
23	71.7	175.7	0.31
1200	76.1	218.7	0.43

The strength and modulus data obtained in this effort were consistent with results reported by COI. The lower UTS at 1330°C is consistent with expectations.

Figures 8-10 show tensile stress-strain curves obtained at 23, 1200, and 1330°C.

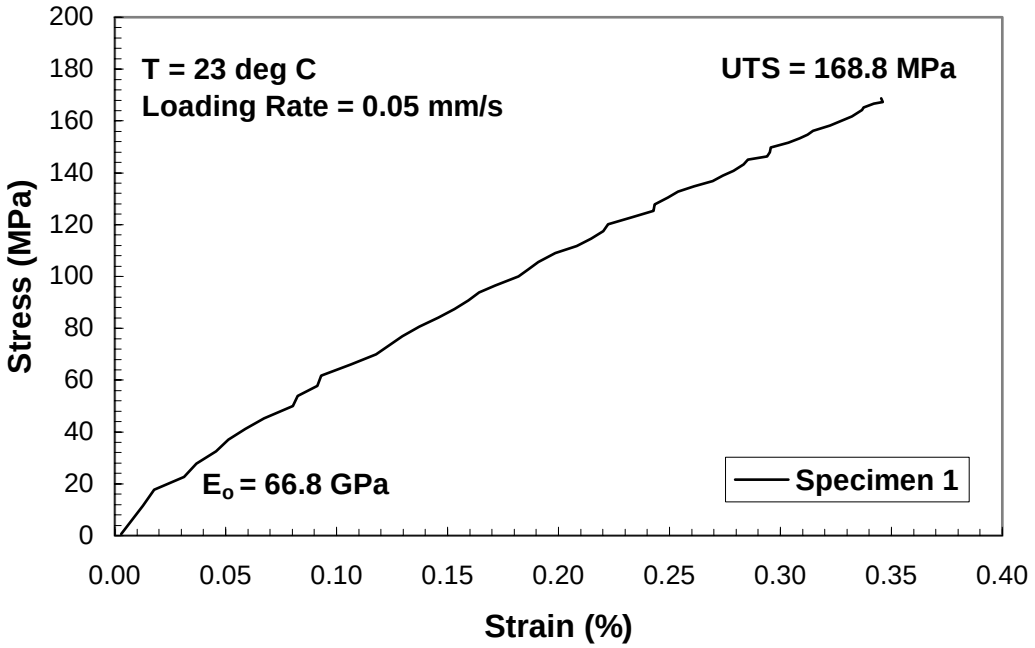

Figure 8. Tensile stress versus strain behavior for Nextel 720/A at 23°C.

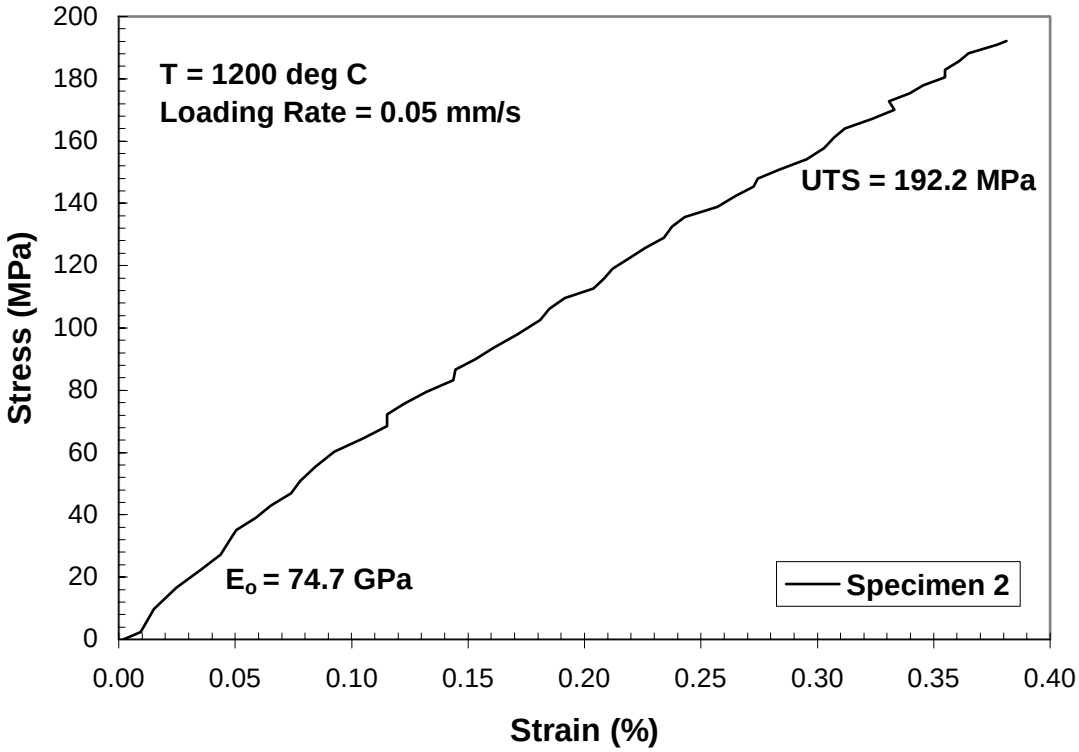

Figure 9. Tensile stress versus strain behavior for N720/A at 1200°C.

Stress-strain curves at 23 and 1200°C are nearly linear to failure. Conversely, the stress-strain curve at 1330°C (shown in Figure 10) reveals inelastic behavior; a distinct "knee" in the stress-strain curve is seen at ~95 MPa.

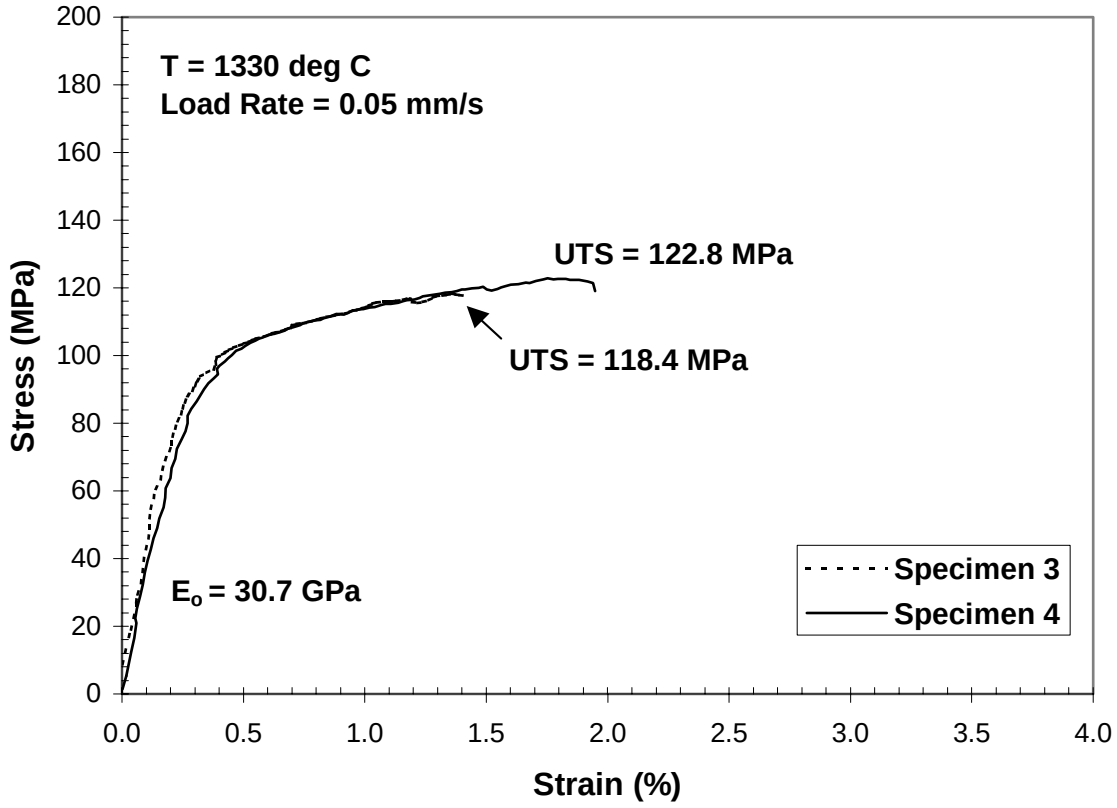

Figure 10. Tensile stress versus strain behavior for N720/A at 1330°C.

3.4. Tension-Tension Fatigue at Elevated Temperatures in Laboratory Air

Fatigue tests conducted in the laboratory air environment are summarized in Table 4, where test temperature, maximum stress level, number of cycles to failure, and failure location are given for each specimen. In discussions below, tests conducted in laboratory air will be referred to as tests in air or in-air tests.

Table 4. Fatigue Tests in Air at Elevated Temperatures

Specimen #	Maximum Stress (R=0.05)		Cycles to Failure	Failure Location
	MPa	% UTS		
Test Temperature = 1200°C				
6	100	52	>120,199	run-out
7	125	65	>146,392	run-out
8	150	78	>167,473	run-out
9	170	88	>109,436	run-out
Test Temperature = 1330°C				
10	50	41	97,282	gage section
11	100	83	1,519	gage section

Figure 11 shows the maximum stress versus cycles to failure for fatigue tests conducted in air at 23, 1200 and 1330°C. All 1200°C tests in air achieved a run-out condition, defined at 10^5 cycles. Conversely, at 1330°C the run-out was not achieved; all 1330°C tests failed before reaching 10^5 cycles. At 1330°C, the 50 MPa test failed at 97,282 cycles, just before reaching the run-out condition. The material exhibits excellent fatigue resistance at 1200°C in air. At 1330°C, however, fatigue performance is significantly diminished.

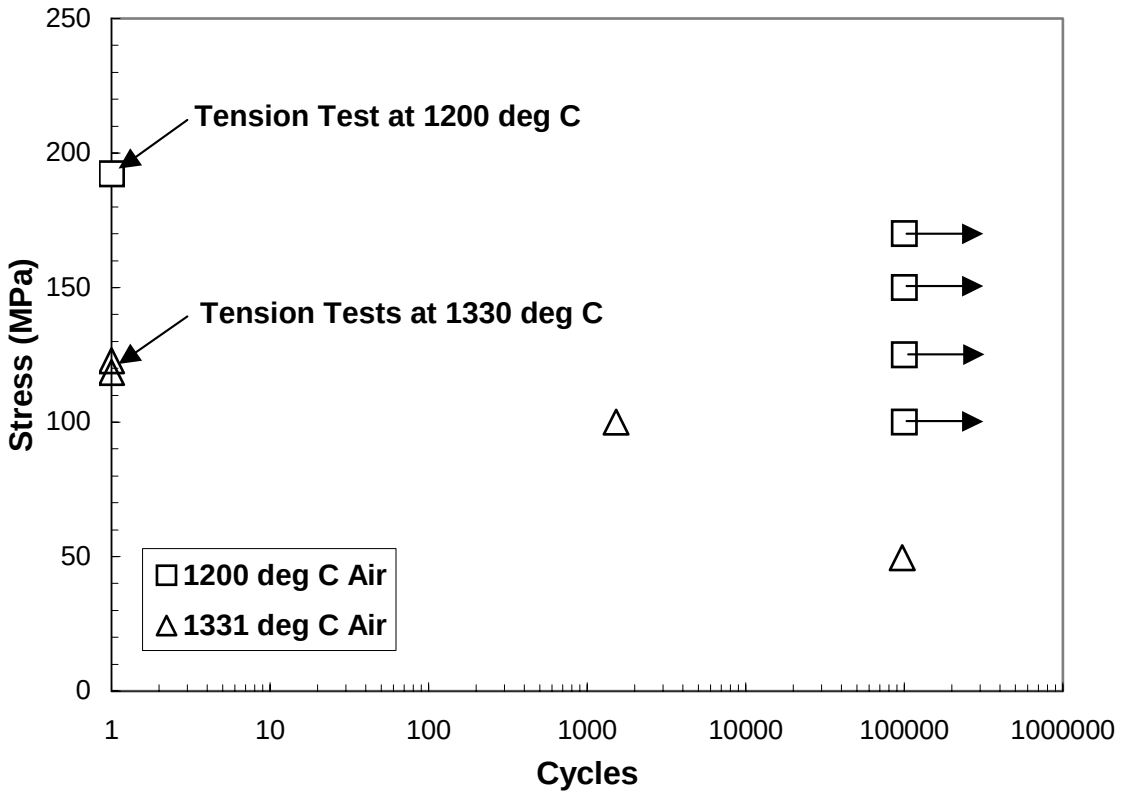

Figure 11. Fatigue plot for Nextel 720/A showing maximum stress versus cycles to failure for fatigue tests in air at 1200 and 1330°C.

3.4.1. Secant Modulus Evolution.

The secant modulus, the slope of a line from the maximum to the minimum point in each cycle, is a measure of damage development in the material. A decrease in the secant modulus may be an indication of damage growth. Ideally, the reduction in modulus should not exceed 10% during the expected service life of the material (26:738). In this oxide-oxide material, the secant modulus decreases gradually as the cycling progresses, the decrease becoming more rapid when approaching failure.

Figure 12 shows the normalized modulus versus fatigue cycles at 1200°C. The modulus is normalized by the modulus of the first complete cycle (Eo). Not shown are the results from the 125 MPa in-air test at 1200°C and the 50 MPa in-air test at 1330°C. Due to an extensometer slip during these tests, strain data was incomplete.

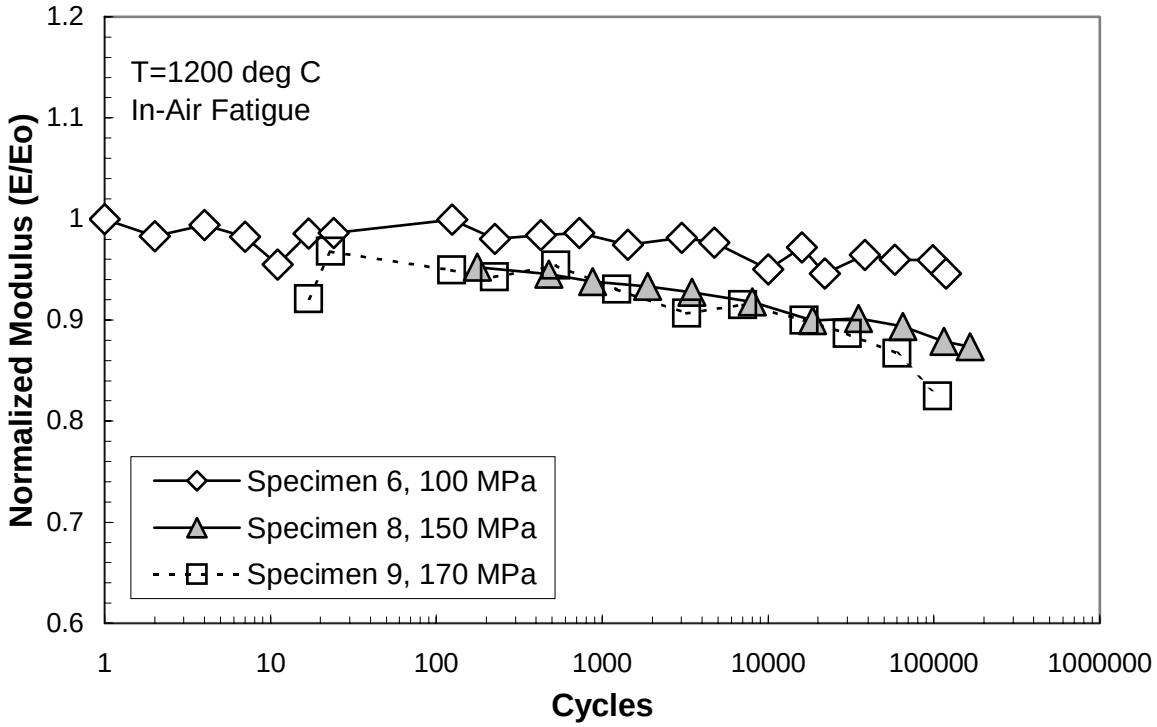

Figure 12. Normalized modulus versus fatigue cycles for specimens tested at 1200°C in air.

Note that although all three tests depicted in Figure 12 were run-outs, a decrease in the normalized modulus is observed. Reductions in normalized modulus were 20, 12, and 5% for the 170, 150, and 125 MPa tests, respectively.

Figure 13 depicts a more rapid decrease in normalized modulus in the 1330°C test. At 1330°C, modulus loss in the 100 MPa test was ~15%. This suggests that fatigue damage is accumulating faster at the higher temperature.

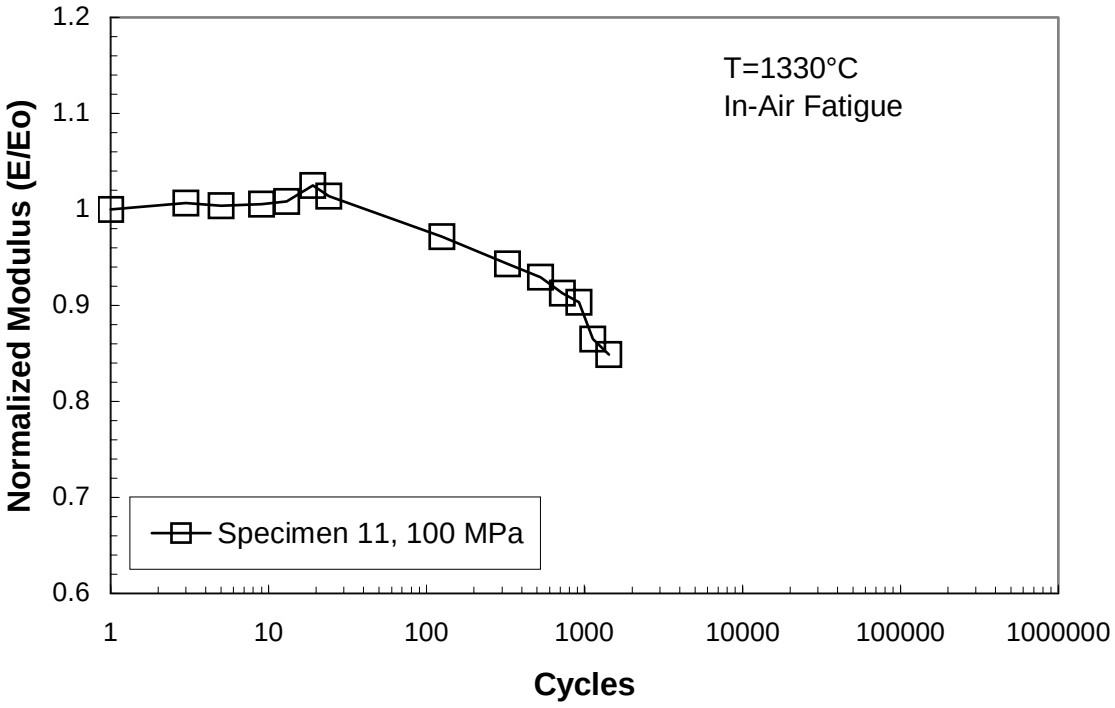

Figure 13. Normalized modulus versus fatigue cycles for specimen tested at 1330°C in air. Specimen failed at 1519 cycles.

Compared to the 5% decrease in modulus observed at a stress level of 100 MPa at 1200°C (Figure 12), the decrease of ~15% is substantial and is an indication of the accelerated fatigue damage leading to an earlier failure.

3.4.2. Energy Dissipation.

Presented in Figure 14 are the cyclic hysteresis loops obtained for various cycles in the 100 MPa fatigue test conducted in air. The plot is representative of the cyclic hysteresis loop evolution observed in all fatigue tests conducted in this effort.

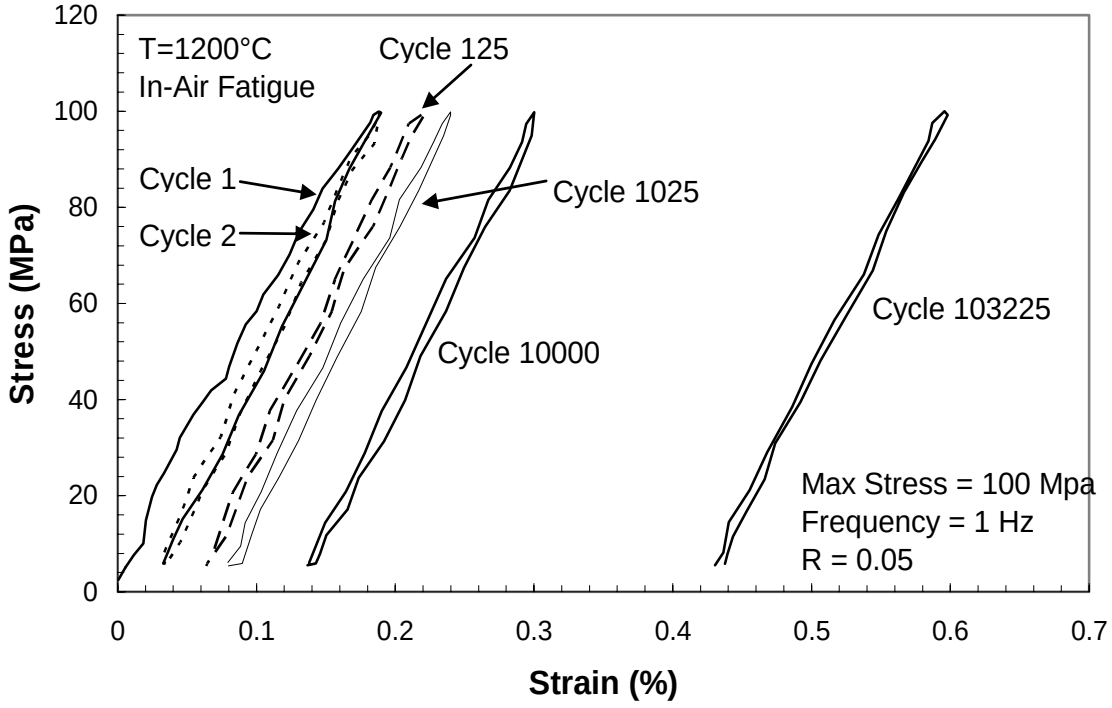

Figure 14. Evolution of hysteresis stress-strain loops with fatigue cycles for Specimen 6, tested in tension-tension fatigue at 100 MPa in air at 1200°C.

Generally, energy is dissipated during fatigue in the form of heat when plastic deformation is present. Thus, during each cycle some energy is dissipated. The energy lost as the cycles progress is characterized by the change in the area enclosed by the hysteresis loops (18:374, 27:54). The area of each hysteresis loop can be expressed in mm/mm*MPa, which is equivalent to kJ/m^3, referred to as hysteretic energy density

(HED). Thus, the energy loss per cycle, or ΔW, can be assessed by examining the change in area of the hysteresis loops.

In the case of the oxide-oxide material investigated, the hysteresis loops are narrow, so the shape of each loop can be approximated by a quadrilateral. To find the area of each loop, a best-fit line was found for both the ascending and the descending portion of the cycle. These lines represented two sides of the quadrilateral. The third and forth sides were the distance between these lines at the maximum and minimum points in the cycle.

Figure 15 depicts the hysteretic energy density versus fatigue cycles for specimens tested in air at 1200°C.

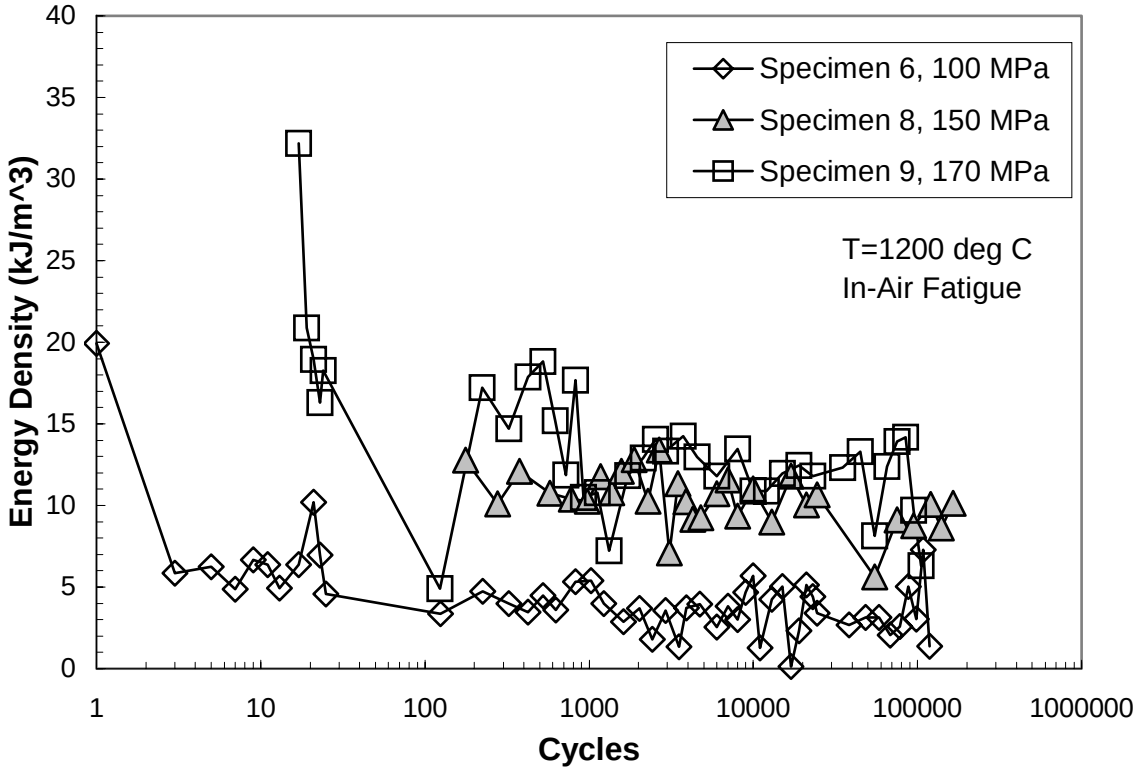

Figure 15. Hysteretic energy density versus fatigue cycles for specimens tested at 1200°C in air.

Figure 15 shows that HED decreases rapidly during the first few cycles. As the cycling progresses, less hysteretic energy is lost per cycle. The stabilized values of the HED in these tests were between 5 and 15 kJ/m^3.

The same qualitative behavior is observed for specimens tested at different maximum stress levels and temperatures. It is seen in Figure 16 that at 1330°C, the HED decreases in a similar fashion. A sharp decrease in HED is observed during the first few cycles. As cycling progresses, the HED values stabilize at about 20 kJ/m^3.

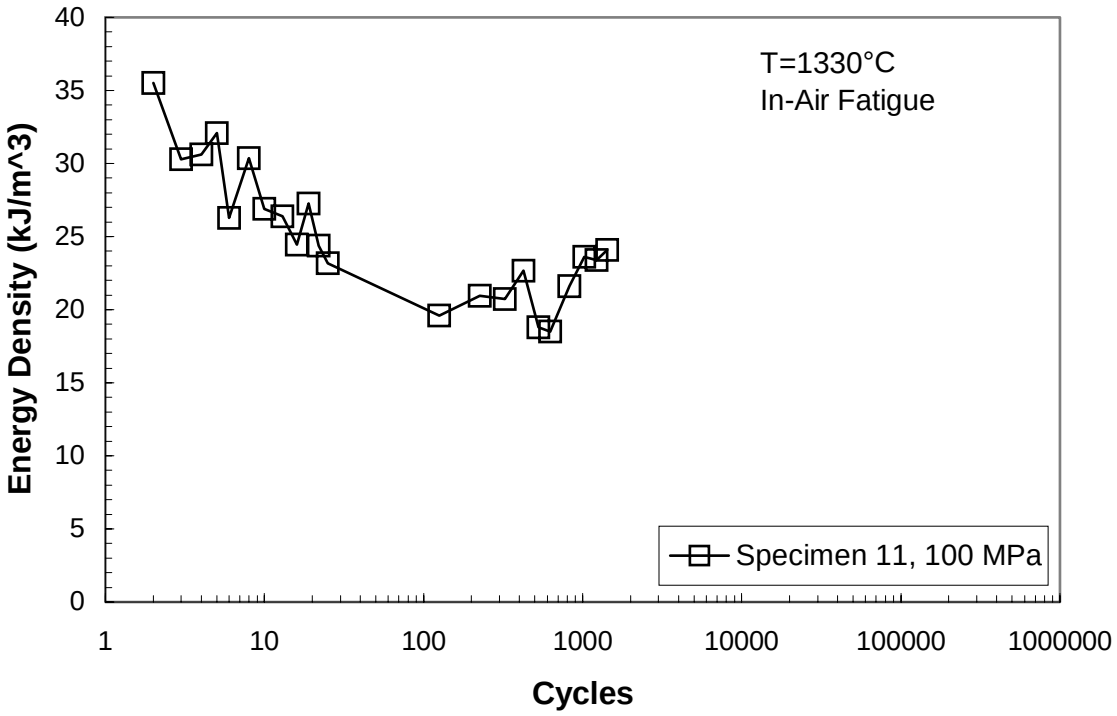

Figure 16. Hysteretic energy density versus fatigue cycles for specimen tested at 1330°C in air.

Note that at both 1200°C and 1330°C, the HED exhibits similar evolution with fatigue cycles. However, the saturated HED values are higher at 1330°C than at 1200°C, which indicates a more rapid damage growth with cycling at the higher temperature.

3.4.3. Strain Accumulation.

Fatigue damage growth can be assessed by monitoring the evolution of the maximum and minimum strain with fatigue cycles. Accumulation of strain is frequently an indication of development of fatigue damage in the material. Figures 17 and 18 show the evolution of the minimum and maximum strain with cycling at 1200 and 1330°C in air. Two curves are depicted for each specimen, which represent the maximum and minimum strain measured within each cycle.

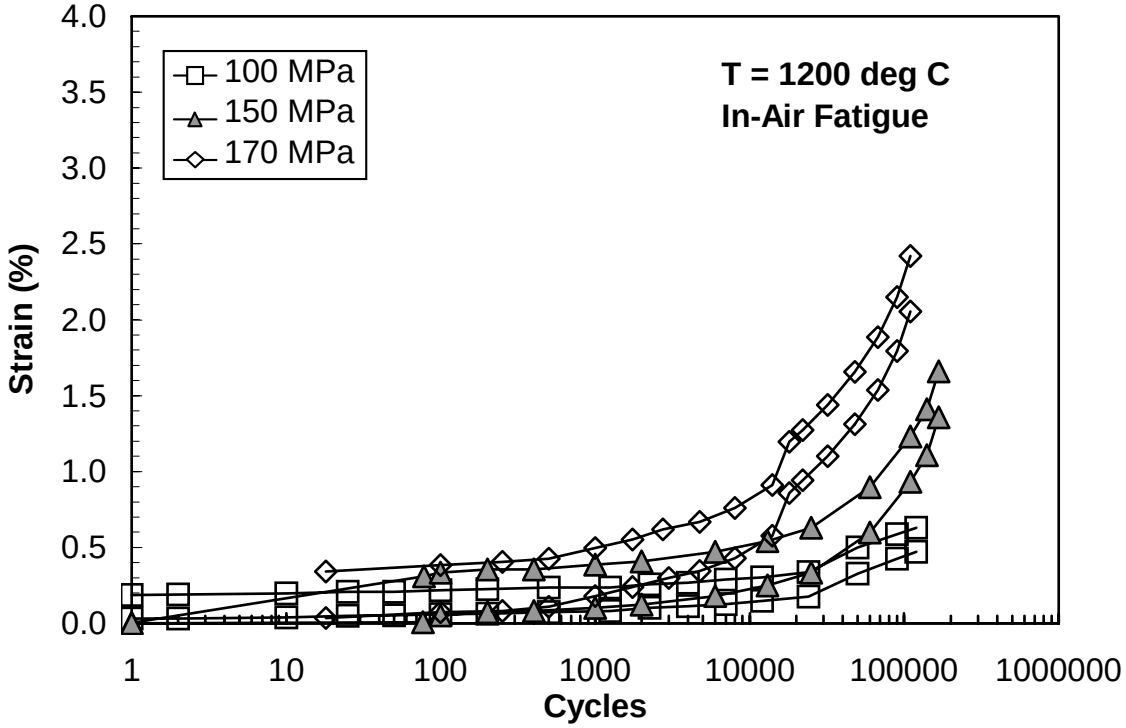

Figure 17. Maximum and minimum strain versus fatigue cycles at 1200°C in air. All three tests were run-outs.

Although all tests represented in Figure 17 were run-outs, there is still a noticeable accumulation of strain. The test conducted at the highest stress level, 170 MPa, has the greatest amount of strain accumulation. As the stress level decreases, so does the amount of strain accumulated. This indicates that as the maximum stress level decreases, a lesser amount of fatigue damage growth occurs as the cycles progress.

All three specimens tested at 1200°C and shown in Figure 17 maintain an insignificant amount of strain (less than 0.5%) until nearly 1000 cycles. Strain accumulated in the 150 MPa test remains below 0.5% until 6000 cycles, and the strain accumulated in the 100 MPa test doe so until more than 13,000 cycles.

Figure 18 shows the maximum and minimum strain as functions of cycle number for the 100 MPa test at 1330°C in air.

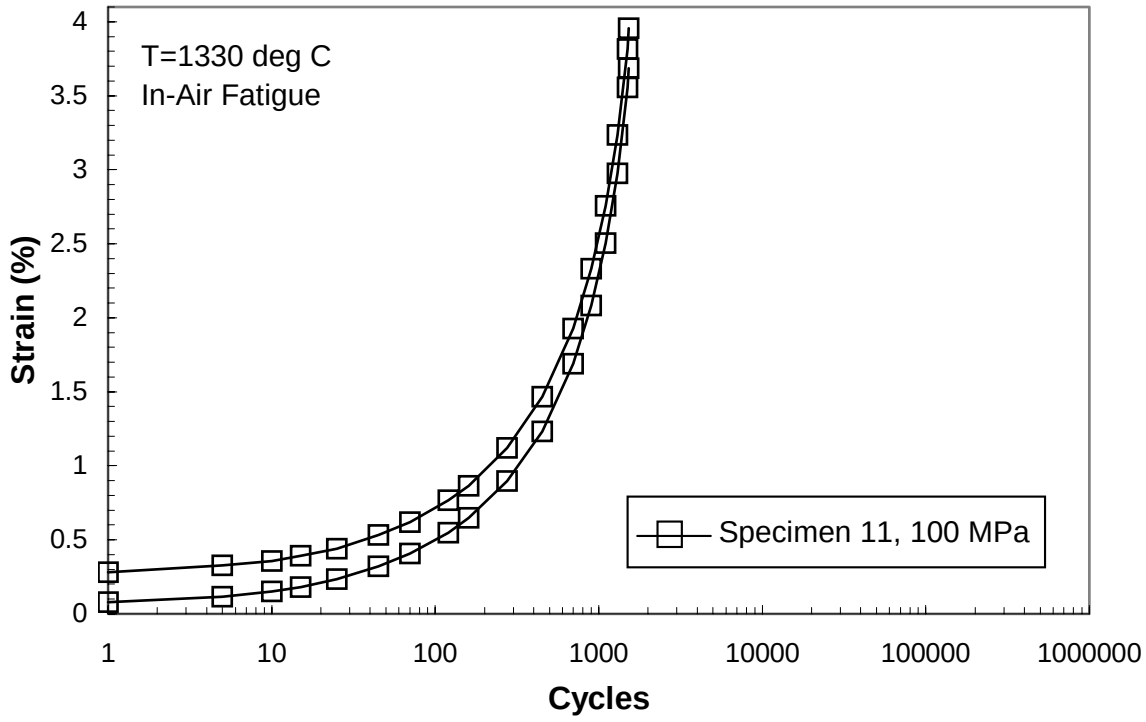

Figure 18. Maximum and minimum strain versus fatigue cycles at 1330°C in air. Specimen failed after 1519 cycles.

Figure 18 shows that the strain accumulates more rapidly at the higher temperature, indicating faster fatigue damage growth leading to the earlier failure. Also noteworthy is the higher level of strain attained in this test. All of the 1200°C tests, which achieved run-out, accumulated less strain than the 1330°C test that failed after 1519 cycles. Furthermore, the strain in the 1330°C test exceeded 0.5% at a significantly earlier 12 cycles.

Because this is a brittle material, progressive microcracking of the matrix and the breaking of individual fibers are responsible for development of larger strains. As the loading continues, fiber/matrix debonding, crack deflection at the fiber/matrix interface, and fiber pullout occur, ultimately leading to a non-catastrophic failure of the specimen (3:239).

3.4.4. Retained Strength and Stiffness Properties.

All of the 1200°C tests in air achieved run-out, defined as surviving 10^5 cycles at 1 Hz. Once run-out is achieved, retained strength and stiffness are measured in a tensile test to failure at 1200°C. Table 5 shows the residual strength and stiffness.

Table 5. Retained Properties of the N720/A Specimens Subjected to Prior Fatigue in Laboratory Air at 1200°C

Specimen #	Maximum Stress (MPa)	Fatigue Cycles	Residual Strength (MPa)	Residual Modulus (GPa)	Residual Failure Strain (%)
6	100	120,199	194.4	52.9	0.44
7	125	146,392	199.0	54.9	0.45
8	150	167,473	199.1	42.7	0.53
9	170	109,436	192.0	40.7	0.51

At 1200°C the material retained 100% of its strength. Results in table 5 illustrate that the residual strength of the specimens subjected to prior fatigue cycling in air is even higher than that of the as-received material. This is possibly due to straightening of fibers during the fatigue cycling. These results are consistent with those reported by Steel, who examined fatigue of this material at 1200°C in air for stress levels ≤ 122 MPa (29:Sec 4, 15,47).

3.5. Effect of Steam Environment on Tension-Tension Fatigue at Elevated Temperatures

The effect of the steam environment on the fatigue performance of oxide-oxide at elevated temperatures was investigated in six tests, four at 1200°C and two at 1330°C. Steam represents an oxidizing environment that the material would be exposed to in its service life. Fatigue tests conducted in the steam environment are summarized in table 6, where test temperature, maximum stress level, number of cycles to failure, and failure location are given for each specimen. It is noteworthy that all specimens failed in the gage section. In discussions below, tests conducted in 100% steam environment will be referred to as tests in steam or in-steam tests.

Table 6. Fatigue Tests in Steam at Elevated Temperatures

Specimen #	Maximum Stress (R=0.05)		Cycles to Failure	Failure Location
	MPa	% UTS		
Test Temperature = 1200°C				
12	100	52	>100,780	run-out
13	125	65	>166,326	run-out
14	150	78	11,782	gage section
15	170	88	202	gage section
Test Temperature = 1330°C				
16	50	41	25,852	gage section
17	100	80	347	gage section

Results are presented in Figure 19 as maximum cyclic stress versus cycles to failure. Figure 19 reveals that fatigue life increases with decreasing stress levels in both

the air and the steam environments. In addition, it is seen that the steam environment significantly reduces fatigue life.

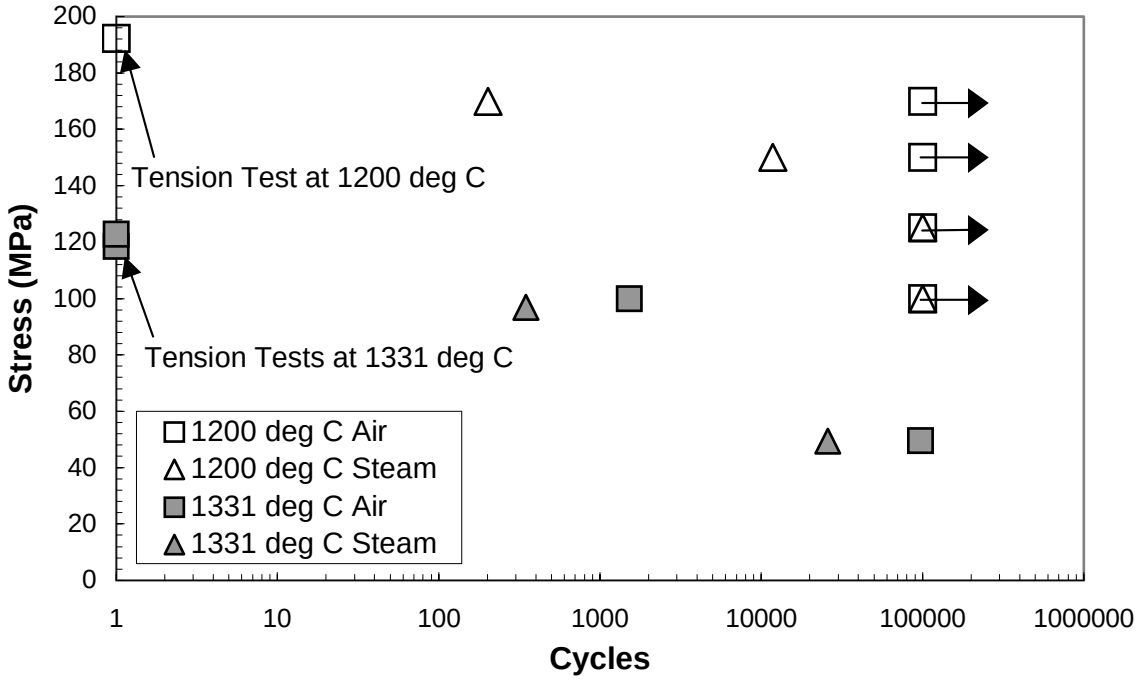

Figure 19. Effect of steam environment on fatigue life of Nextel 720/A at 1200 and 1330°C.

While all of the in-air tests at 1200°C achieved run-out, the 150 MPa and 170 MPa fatigue tests in steam failed prior to surviving 10^5 cycles.

The effect of steam is also apparent in the 1330°C fatigue tests. While all of the tests failed short of run-out due to the increased temperature, the tests conducted in steam again exhibited shorter fatigue life than those conducted in air. These tests show that steam does have a significant effect on the fatigue performance of the material.

It interesting to note that at 1330°C, the tests conducted at both 50 and 100 MPa resulted in a similar reduction in fatigue life when subjected to the steam environment.

The presence of steam at 100 MPa resulted in a 77% decrease in number of cycles to failure while at 50 MPa the decrease in fatigue life was 73%.

3.5.1. Modulus Evolution in Fatigue Tests Conducted in Steam Environment.

Figures 20 and 21 show evolution of the secant modulus evolution with fatigue cycling in steam environment at 1200 and 1330°C, respectively.

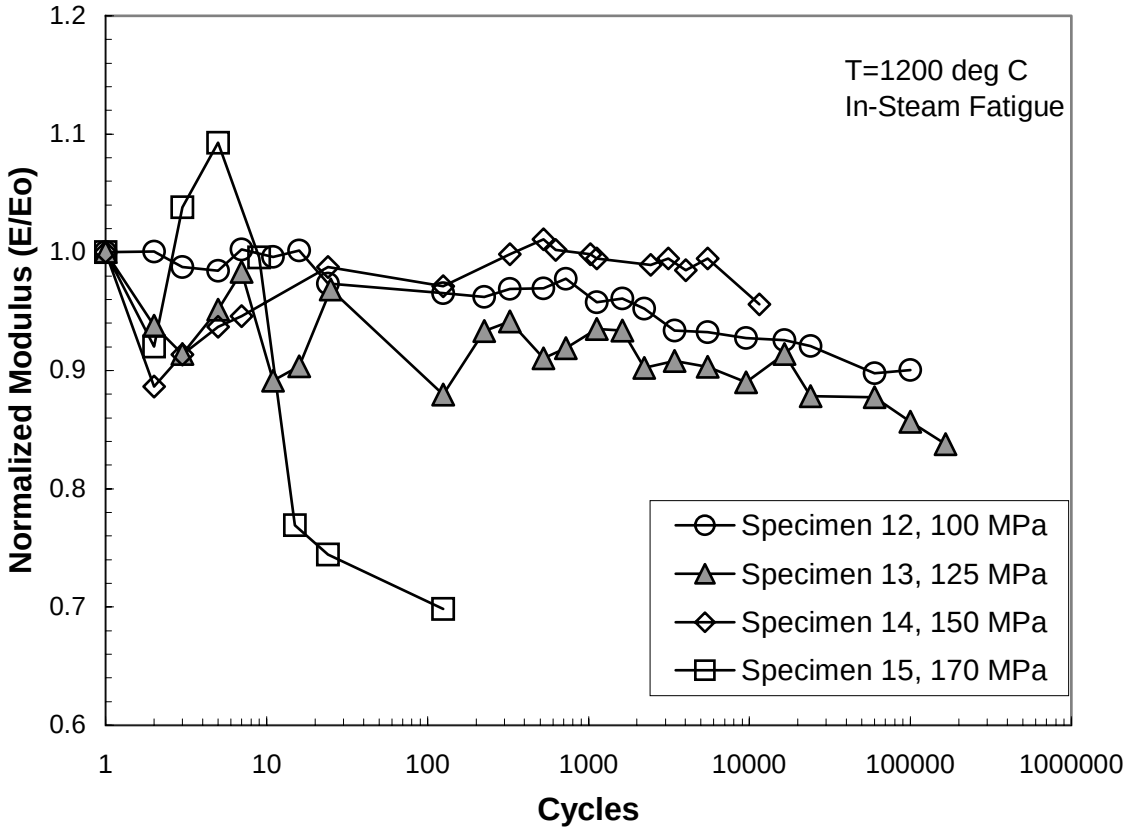

Figure 20. Normalized modulus versus fatigue cycles tested at 1200°C in steam environment.

As seen in Figure 20, both the 100 MPa and 125 MPa tests in steam achieved run-out. The 125 MPa test exhibited a modulus reduction of approximately 17%, while modulus reduction in the 100 MPa test was only 10%. As mentioned previously, it is

generally desirable that the modulus not decrease more than 10% during the service life of the material. Although the 125 MPa test achieved run-out, it did not meet this design criterion.

The normalized modulus for the 170 MPa fatigue test conducted in steam dropped a significant 30% prior to the specimen failing after 202 cycles. The modulus for the 150 MPa test, where the specimen failed at 11,782 cycles, decreased only ~5%. In several of the tests, the modulus slightly increased in some early cycles before subsequently decreasing. This phenomenon may be attributed to the straightening of ceramic fibers during the first few cycles of the test.

It is interesting to note that the specimen tested at 125 MPa (a run-out test) experienced a greater reduction in modulus than the specimen tested at 150 MPa that failed. Therefore, a decrease in modulus alone may not provide a conclusive indication of impending failure.

In comparing the results obtained in the in-steam tests at 1200°C to those obtained in the air environment, it is seen that greater decrease in modulus was produced in steam. The 150 MPa test conducted at 1200°C in steam represents an exception. The presence of steam appears to accelerate fatigue damage growth.

Figure 21 shows the decrease in normalized modulus with fatigue cycles for the specimens tested at 1330°C in steam.

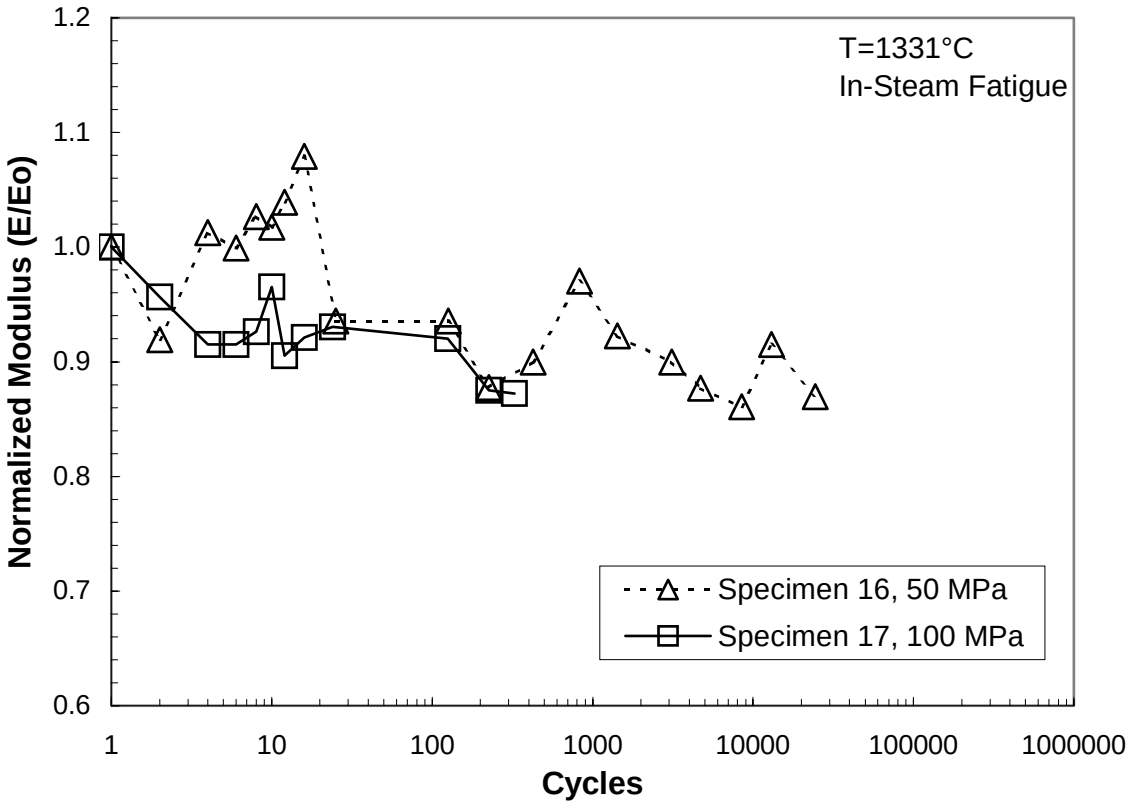

Figure 21. Normalized modulus versus fatigue cycles at 1330°C in steam environment.

Neither specimen represented in Figure 21 achieved run-out. The 100 MPa test failed after 202 cycles and the 50 MPa test after 97,282 cycles. Interestingly, modulus loss for both specimens was approximately 15%.

The specimen tested in air at 1330°C also lost approximately 15% in modulus (see Figure 13 in Section 3.4.1). This suggests that the reduction in modulus with fatigue cycles at 1330°C may be independent of the stress level or test environment.

3.5.2. Evolution of Hysteresis Energy Density in the Steam Environment.

The hysteresis loops for the specimens tested in steam had the same qualitative appearance as those tested in air. For their typical appearance, the reader is referred to Figure 14 in Section 3.4.2. The area of the hysteresis loops, representing the hysteretic energy density (HED), is calculated using the method described in Section 3.4.2.

Figure 22 shows the HED versus fatigue cycles for tests conducted in steam at 1200°C. The data obtained in the 170 MPa test is not shown due to its significantly higher scale. It illustrates the same general trend, but its depiction would overshadow the smaller HED values.

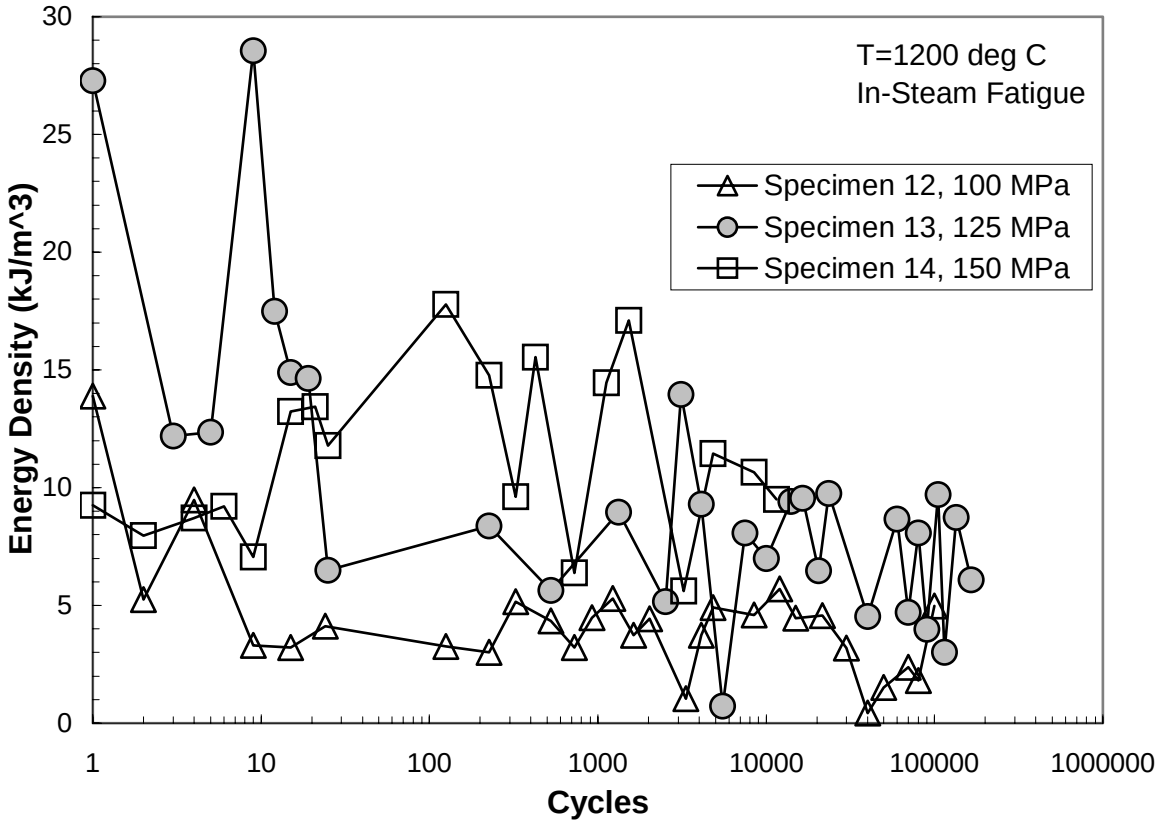

Figure 22. Hysteretic energy density versus fatigue cycles tested at 1200°C in steam environment.

Figure 22 shows that the HED exhibits a decreasing trend for each stress level when tested in steam. The HED in the 150 MPa test continued to decrease until failure at 11,782 cycles, while the HED in the 125 and 100 MPa tests became saturated at approximately 6 kJ/m^3 and 3 kJ/m^3, respectively.

These saturation values are similar to those obtained at 1200°C in the air environment. It does not appear that the HED behavior is affected by the steam environment at 1200°C.

Figure 23 shows the HED as a function of fatigue cycles in the steam environment at 1330°C.

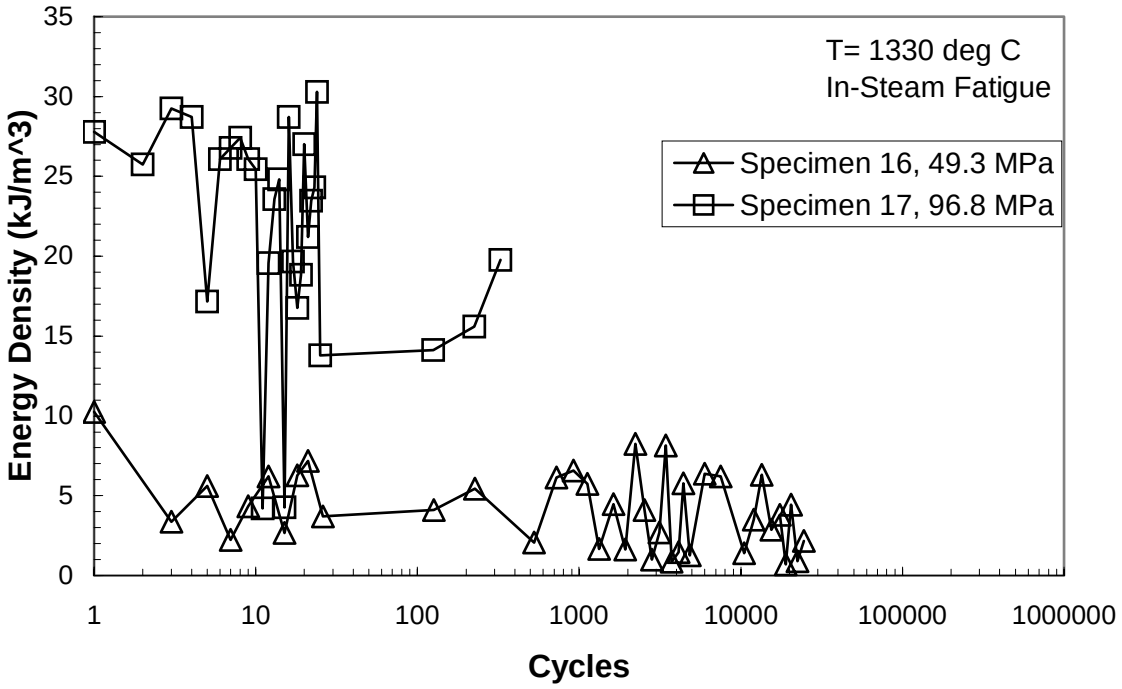

Figure 23. Hysteretic energy density versus fatigue cycles at 1330°C in steam environment.

The HED again decreases with fatigue cycles at 1330°C in a steam environment. This is similar to the behavior observed in air at 1330°C, indicating that the presence of steam does not significantly affect the HED behavior.

3.5.3. Strain Accumulation in the Steam Environment.

Figures 24 and 25 show the maximum and minimum strain as functions of cycle numbers at 1200 and 1330°C, in steam environment.

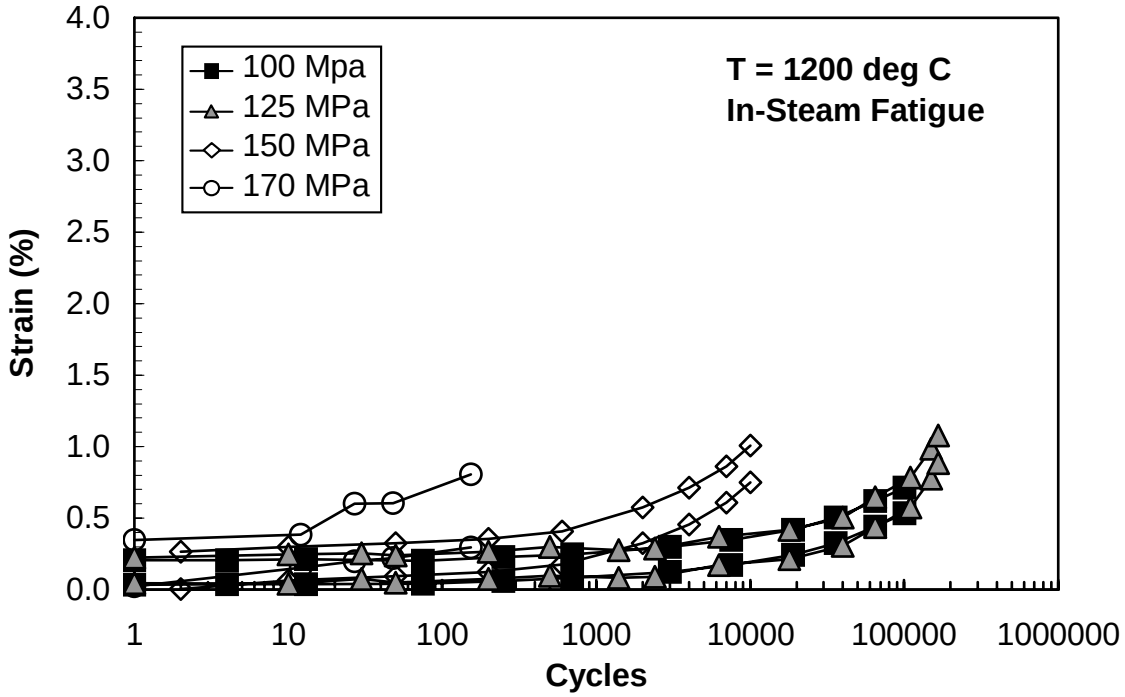

Figure 24. Maximum and minimum strain versus fatigue cycles at 1200°C in steam environment.

All specimens tested at 1200°C in steam had accumulated similar amounts of strain. The 100 and 125 MPa tests achieved run-out, while the 150 and 170 MPa tests failed. Interestingly, the strain accumulated in the 1330°C tests conducted in steam is less than that obtained in the in-air tests at 1200°C.

Figure 25 depicts the strain accumulated in the specimens tested at 1330°C in the steam environment. As in the case of the 1200°C tests in steam, both the 100 and 50 MPa tests produced similar amounts of strain. This suggests that in the steam environment, the material will only produce a certain amount of strain before failure.

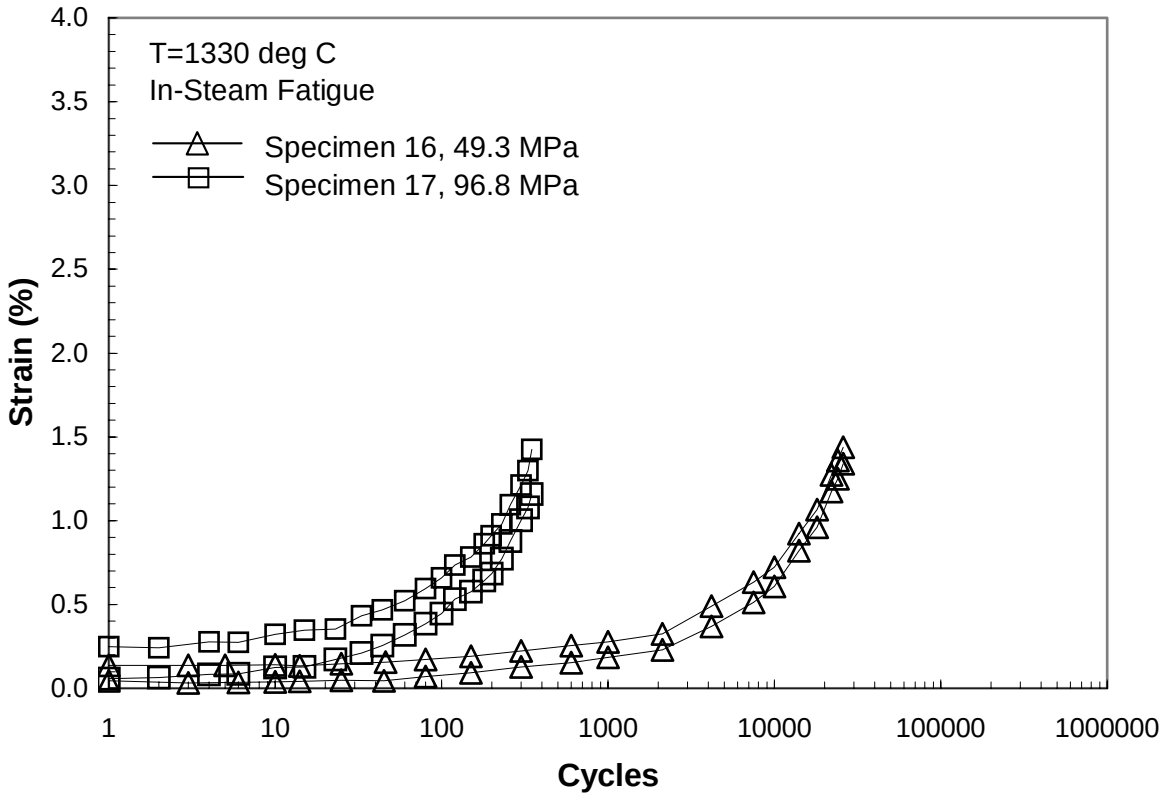

Figure 25. Maximum and minimum strain versus fatigue cycles at 1330°C in steam environment.

It is noteworthy that the specimens tested in air produced higher strain for a given number of cycles and maximum stress level than those tested in steam (see Section 3.4.3.). The in-air tests at 150 and 170 MPa achieved run-out conditions while the 150 and 170 MPa tests in steam failed after 11,782 and 202 cycles, respectively. This observation leads to a conclusion that lower strain accumulation (generally indicative of matrix microcracking) in the 150 MPa and 170 MPa in-steam tests may be attributed to early fiber bundle failures leading to specimen failures. Therefore, strain accumulation may not provide a reliable criterion for fatigue life prediction.

3.5.4. Retained Strength and Stiffness of Specimens Subjected to Prior Fatigue in Steam Environment.

Two tests conducted at 1200°C in the steam environment achieved run-out. None of the tests conducted at 1330°C in steam achieved run-out. Table 7 shows the residual strength and stiffness for specimens subjected to prior fatigue in steam.

Table 7. Retained Properties of Specimens Subjected to Prior Fatigue in Steam at 1200°C

Specimen #	Maximum Stress (MPa)	Fatigue Cycles	Residual Strength (MPa)	Residual Modulus (GPa)	Residual Failure Strain (%)
12	100	100,780	173.7	47.6	0.40
13	125	166,372	168.5	52.1	0.43

Compared to the residual strength produced in air (reported in section 3.4.4), prior fatigue in steam results in significant reduction in residual strength. Thus, although these tests achieved run-out, prior fatigue in steam caused a significantly greater degradation of properties than prior fatigue in air.

3.6. Microstructure Analysis

It is instructive to examine the fracture surfaces of the failed material at a microscopic level to evaluate the failure mechanisms involved.

Figures 26-29 show optical micrographs of the failed specimens, presented in order of increasing maximum stress, in both air and steam environments.

Figure 26 shows the fracture surfaces of specimens failed in monotonic tension.

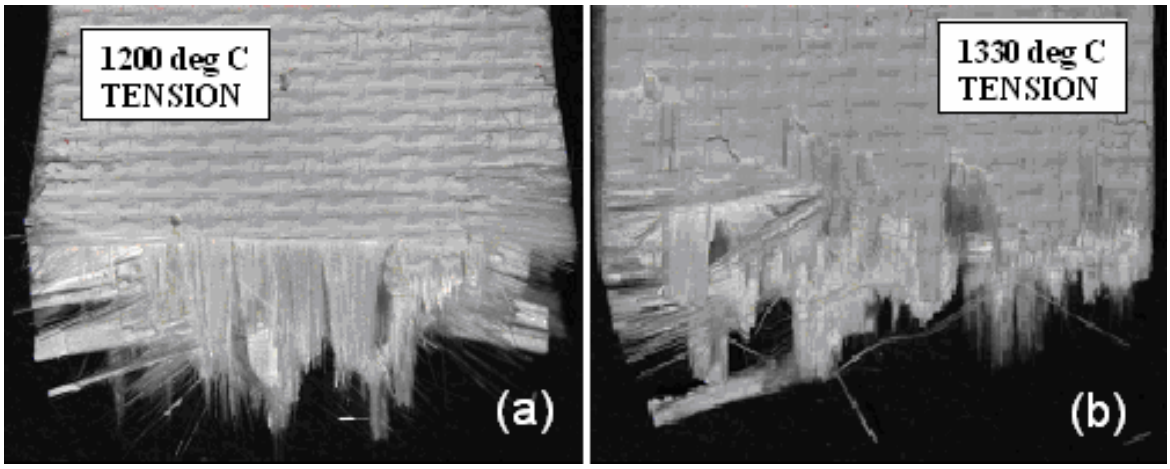

Figure 26. Optical micrograph of fracture surfaces of specimens subjected to monotonic tension at (a) 1200°C and (b) 1330°C.

Figure 27 shows the fracture surfaces of specimens subjected to fatigue in air at 1200°C, followed by monotonic tension to failure after achieving fatigue run-out. At 1200°C, with increasing stress levels there is no apparent trend in the fracture surfaces of the material. For each stress level, extensive pullout in the form of individual fibers and complete fiber bundles is observed.

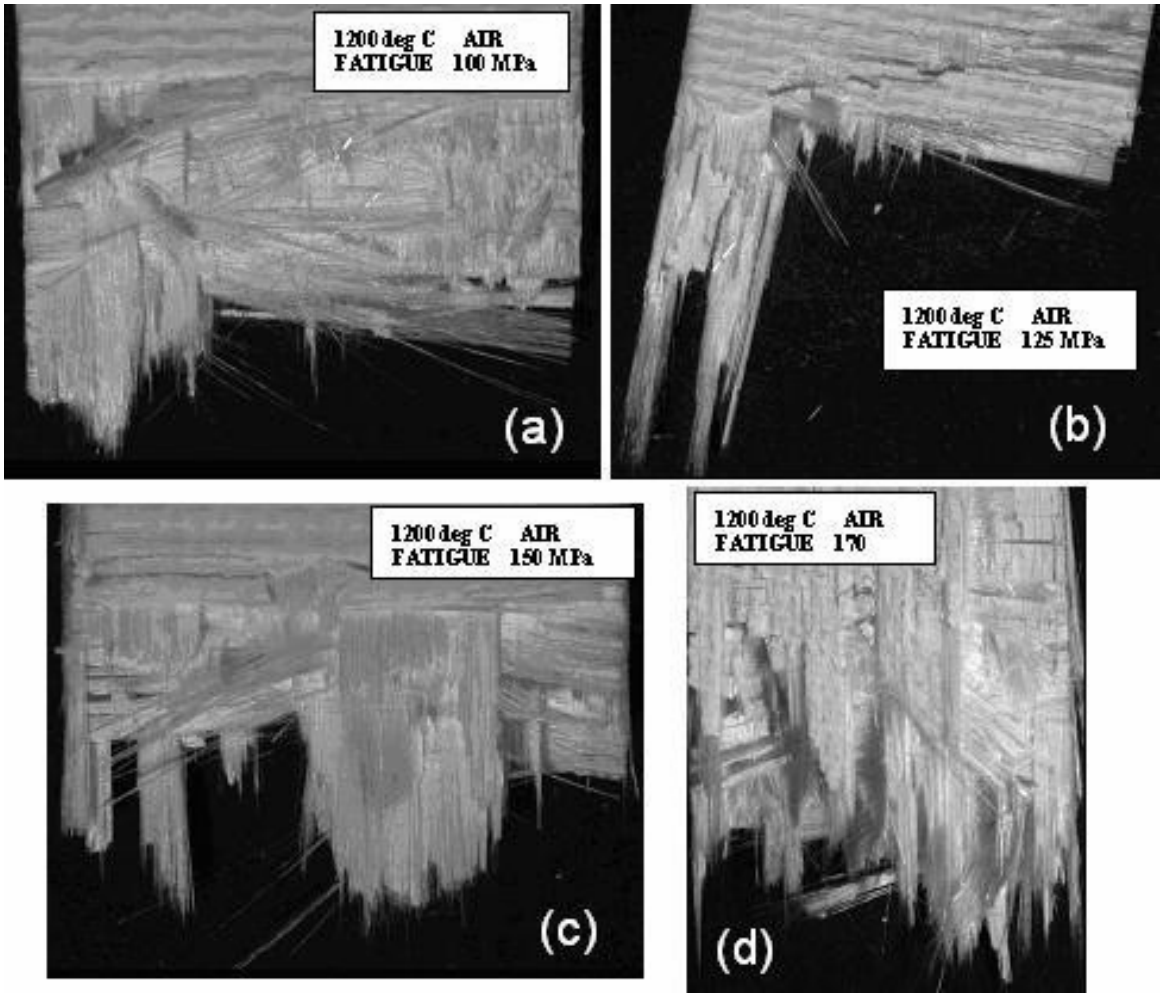

Figure 27. Optical micrographs of specimens tested in air at 1200°C in fatigue loading with maximum stress of (a) 100 MPa, (b) 125 MPa, (c) 150 MPa, and (d) 170 MPa. After achieving run-out specimens were subjected to monotonic tension to failure.

Figure 28 shows optical micrographs of the fracture surfaces of specimens tested in steam at 1200°C. The specimen tested at 100 MPa and 125 MPa achieved run-out, and were subsequently subjected to monotonic tension to failure.

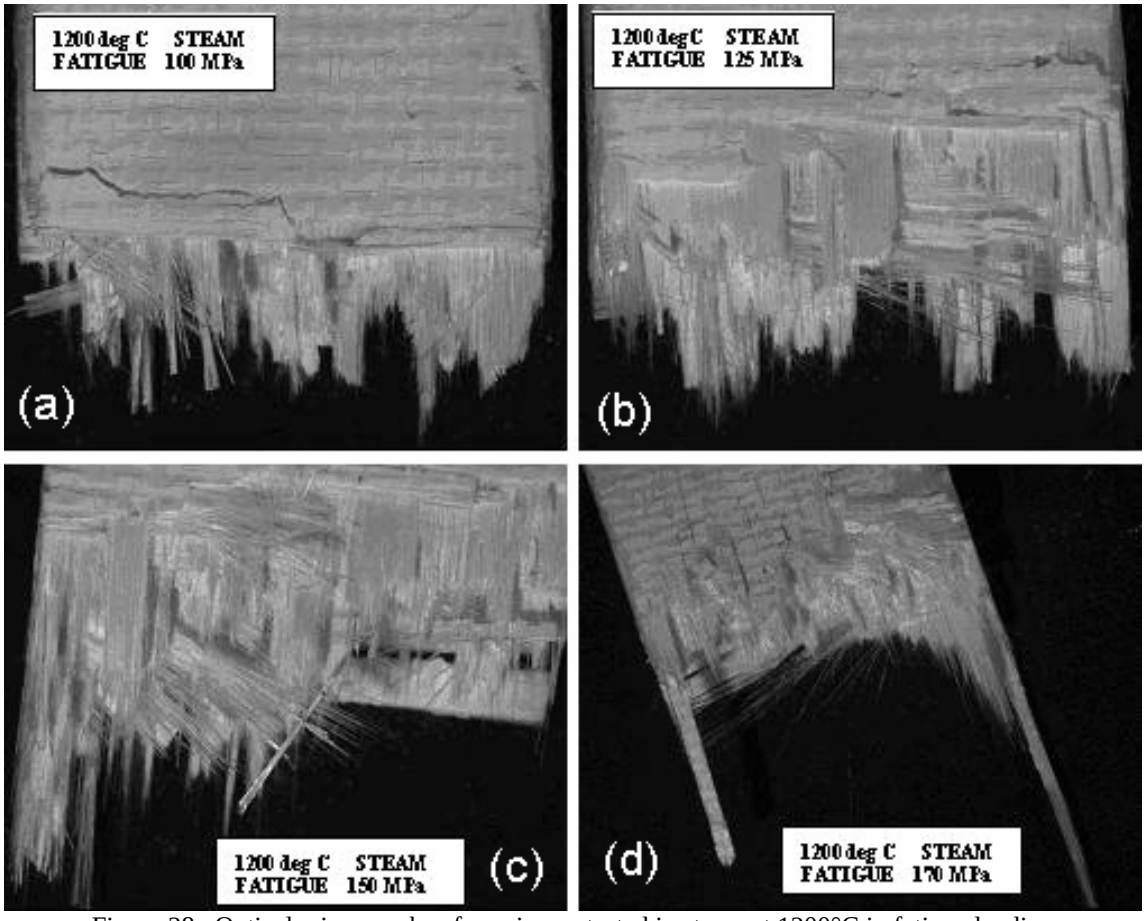

Figure 28. Optical micrographs of specimens tested in steam at 1200°C in fatigue loading with maximum stress of (a) 100 MPa, (b) 125 MPa, (c) 150 MPa, and (d) 170 MPa. After achieving run-out specimens shown in (a) and (b) were subjected to monotonic tension to failure.

As for the specimens that were subjected to fatigue in steam, there is again no apparent trend in the fracture surfaces. Figure 28 shows that the failure surfaces of the specimens are not uniform, with both individual fiber pullout and fiber bundle pullout. Furthermore, comparison of the in-steam failures (Figure 28) and the in-air failures (Figure 27) does not reveal any apparent differences. Tests conducted in the air and steam environments produced similar fracture surfaces.

Figure 29 shows the fracture surfaces of the specimens that were subjected to fatigue at 1330°C in air and in steam environments.

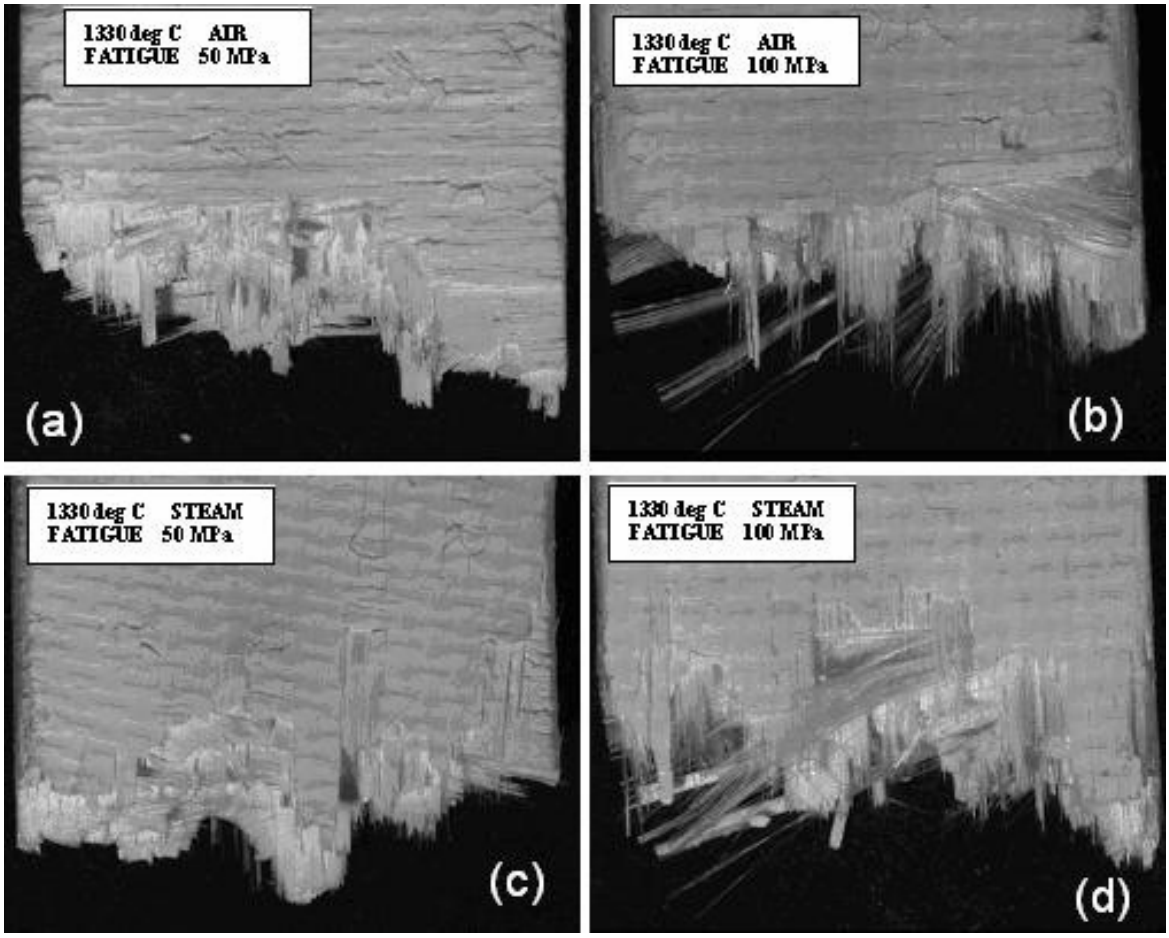

Figure 29. Optical micrographs of specimens tested at 1330°C in fatigue loading with maximum stress of (a) 50 MPa in air, (b) 100 MPa in air, (c) 50 MPa in steam, and (d) 100 MPa in steam.

The specimens tested at 1330°C, like those tested at 1200°C, do not exhibit distinctive trends in the appearance of fracture surfaces. As in the case of the 1200°C tests, specimens tested at 1330°C produce an irregular fracture surface with both individual fracture pullout and fiber bundle failure present.

A conclusion is drawn that there is no apparent trend in the appearance of the fracture surfaces of specimens tested at different fatigue stress levels, temperatures, or environments.

Figures 30-34 present fracture surfaces of various specimens tested in this study. Although each was subject to a different combination of maximum stress, temperature, and environment, produced fracture surfaces are similar in appearance.

Figure 30 shows a typical and representative fracture surface. The fracture surface includes areas that appear nearly flat, and others that show a great amount of fiber pullout.

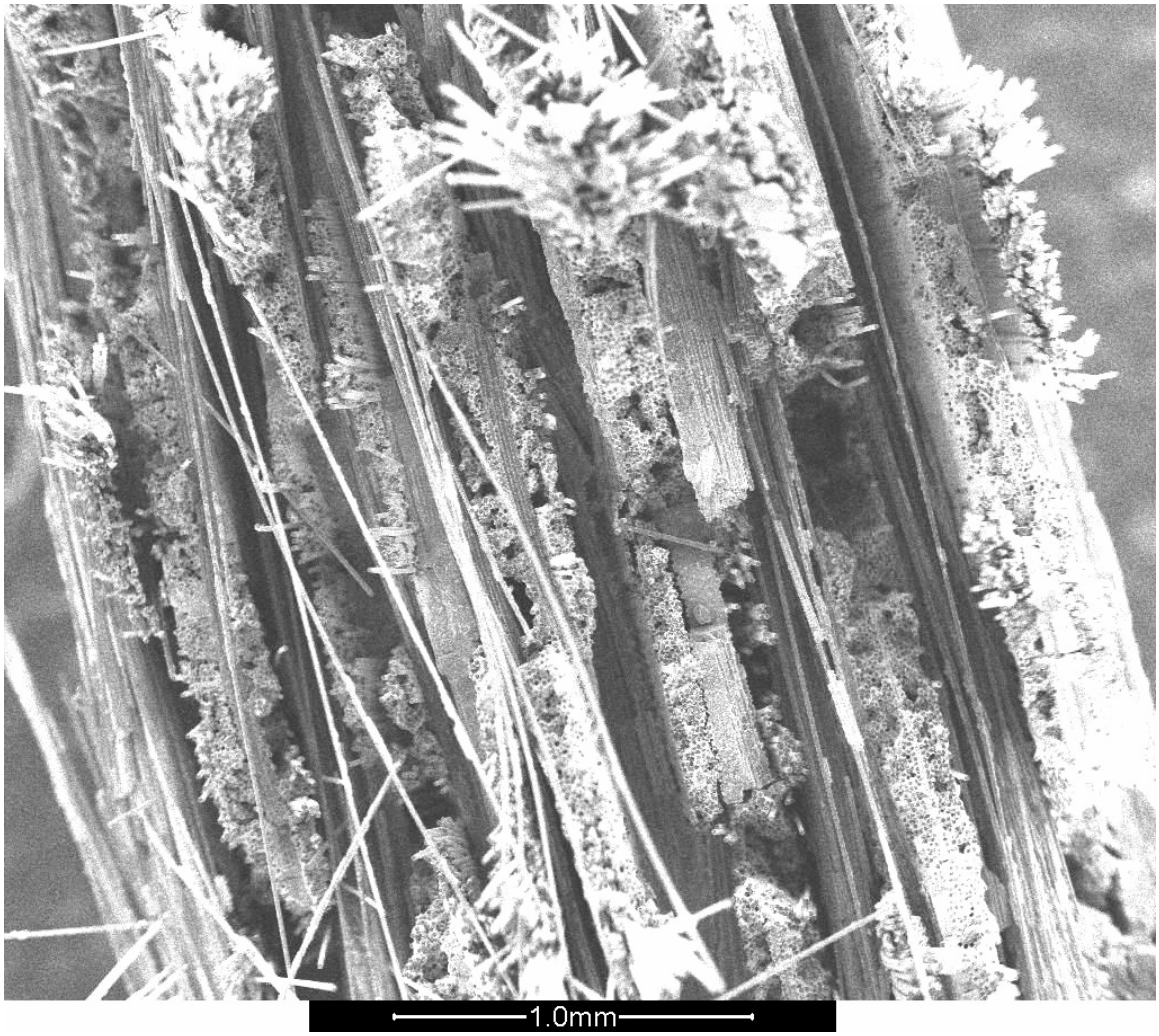

Figure 30. SEM micrograph of Specimen 2, failed in monotonic tension at 1200°C.

Figure 31 shows a failed fiber bundle from a specimen failed under monotonic tension at 1200°C. As with the less magnified view, areas where the matrix and fiber remain well-bonded and areas where the fibers seem to have separated from the matrix are clearly visible.

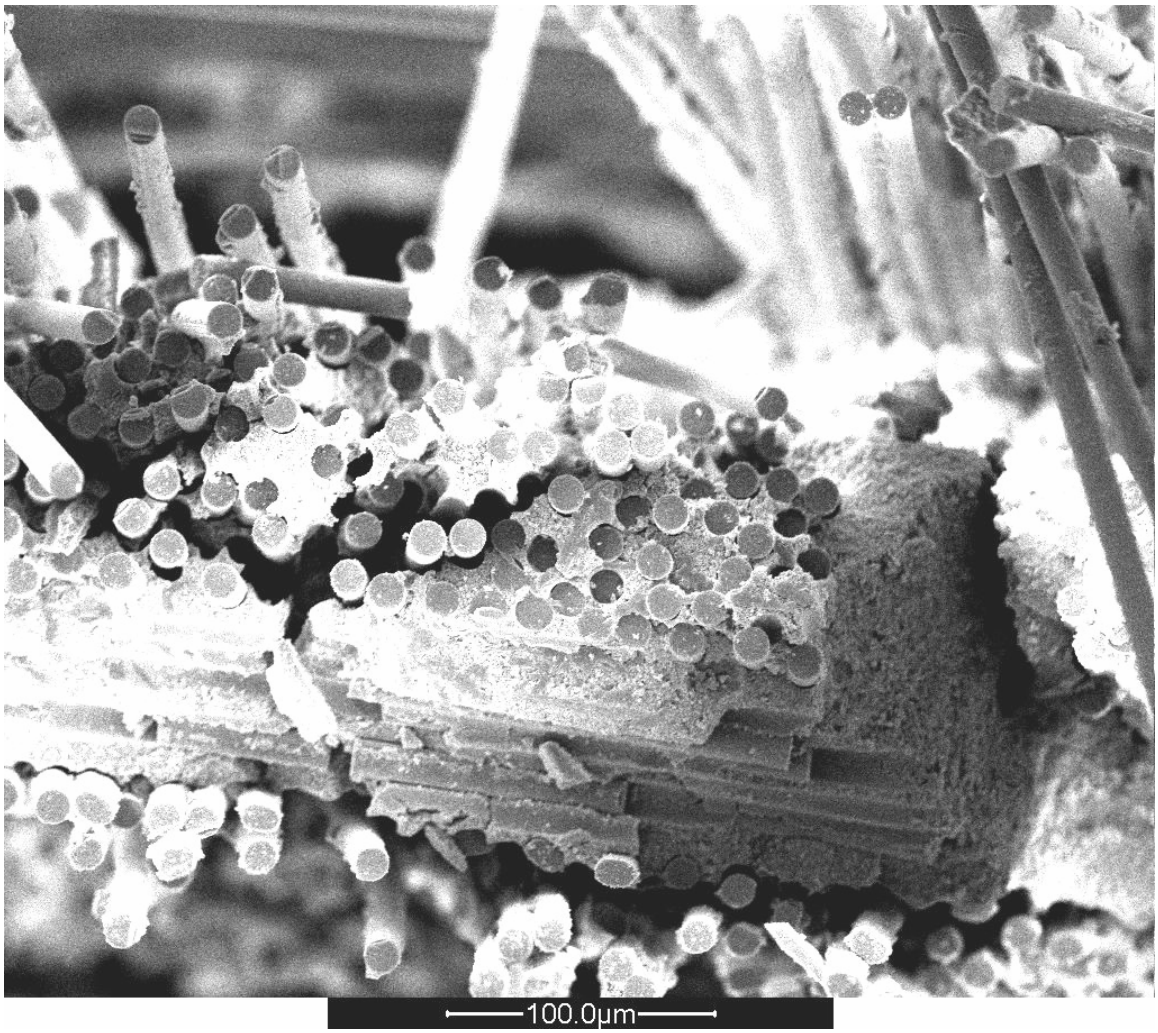

Figure 31. SEM micrograph of Specimen 9, failed in monotonic tension following 109,436 fatigue cycles with maximum stress of 170 MPa in air at 1200°C.

Figure 32 shows a portion of the fracture surface that appears nearly flat at a lower magnification. The closer examination shows that it is not exactly flat, although many fibers failed at nearly the same levels. It is seen that the matrix remains well-bonded to the fibers with a few exceptions.

It is interesting to note the presence of a crack running perpendicular to the fracture surface through the matrix (Figure 32). Although this crack did not contribute to the failure of the specimen, it does serve to illustrate how the porous matrix allows a crack to propagate through the matrix and around the fibers.

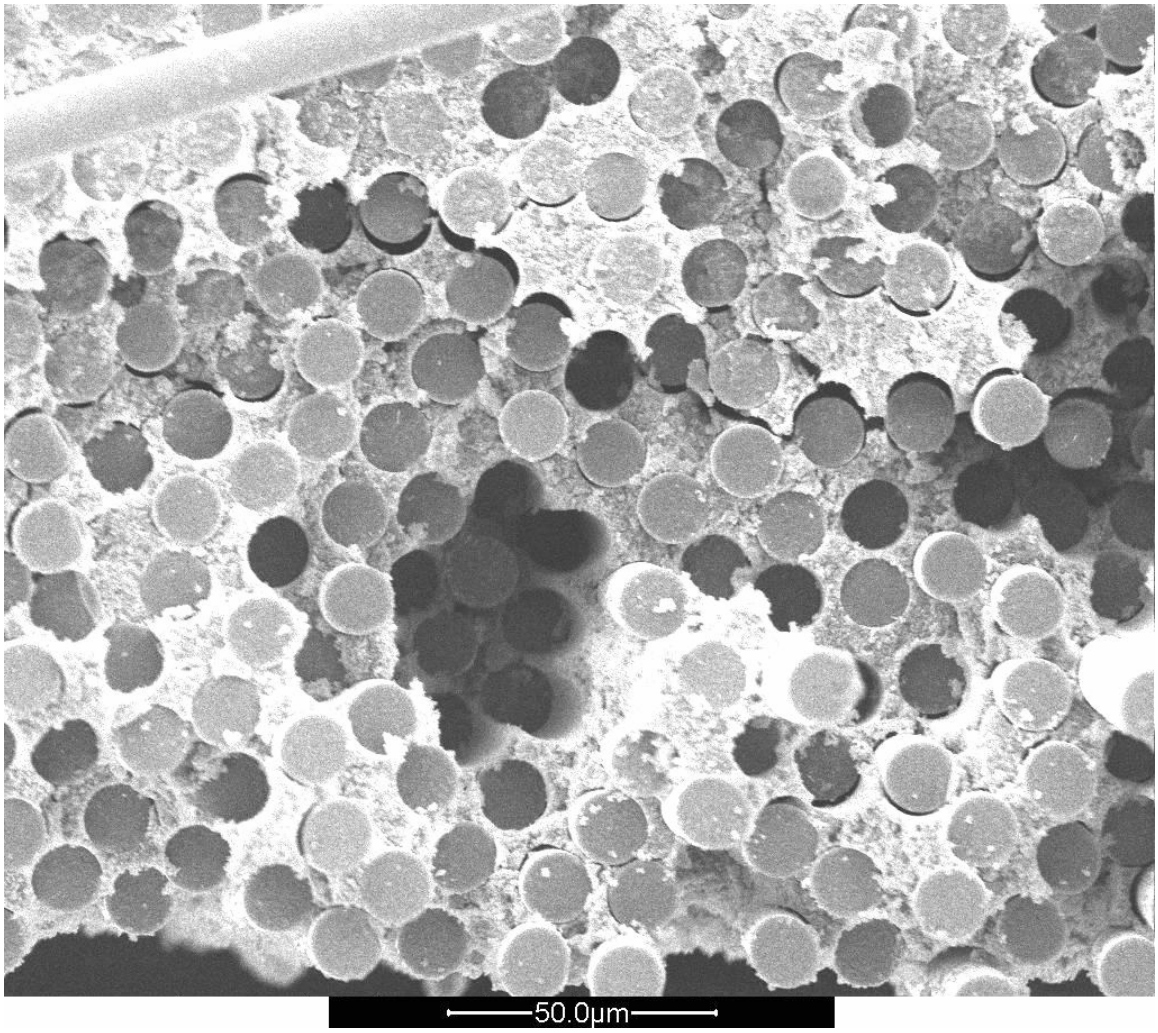

Figure 32. SEM micrograph of Specimen 17, failed under fatigue loading in steam at 100 MPa at 1330°C.

Figure 33 is also representative of areas found in a typical fracture surface. In this micrograph, it can be seen that several fibers broke at about the same level, while others fractured at different planes. Again, the matrix is generally still well-bonded to the fibers, with a few exceptions where spacing between fiber and matrix is visible.

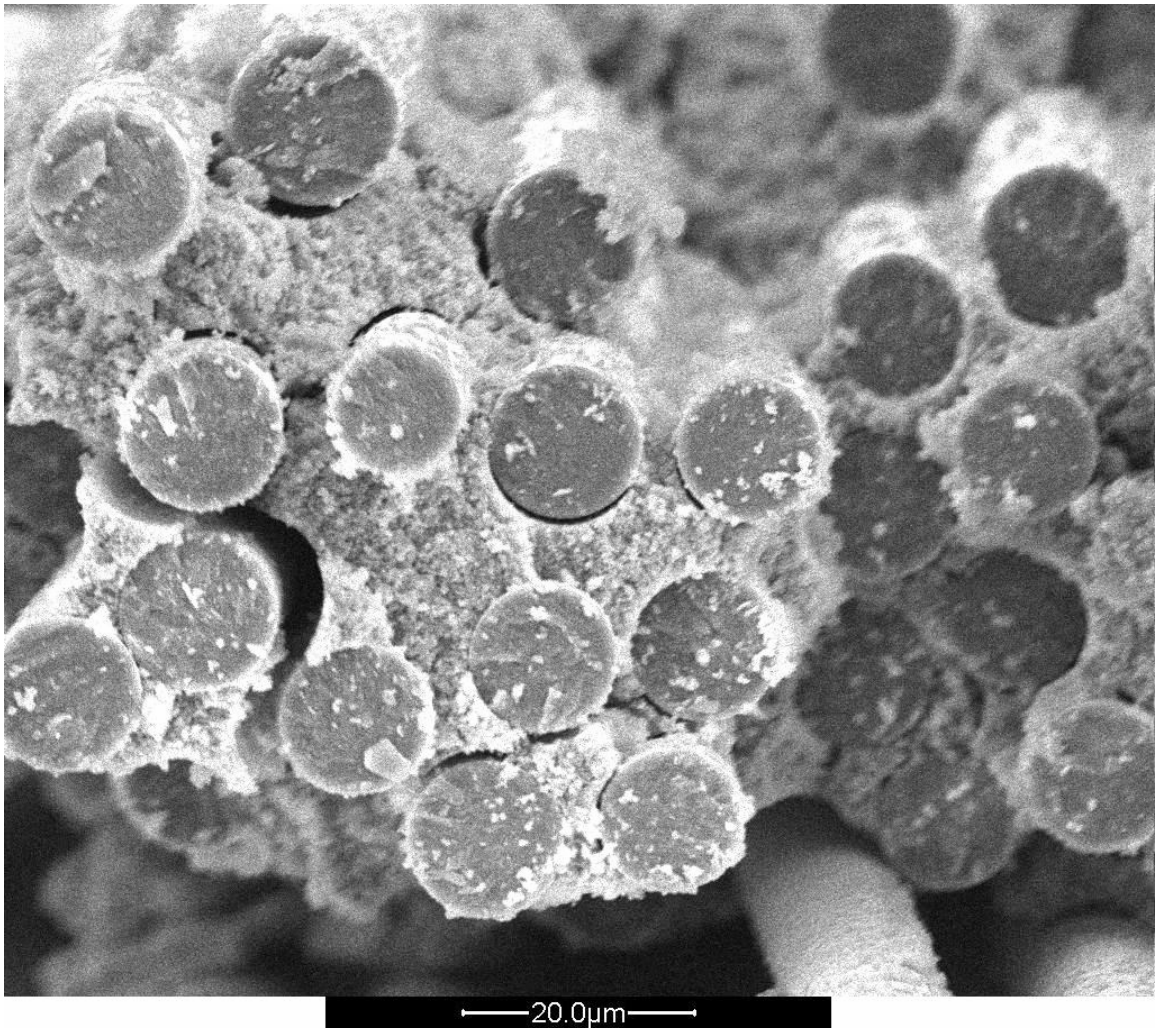

Figure 33. SEM micrograph of Specimen 6, failed in monotonic tension testing following 120,199 cycles of fatigue loading with maximum stress of 100 MPa in air at 1200°C.

Figure 34 shows a region of the fracture surface where individual fiber pullout is dominant. In this region of the fracture surface, the matrix is not visible between the individual fibers.

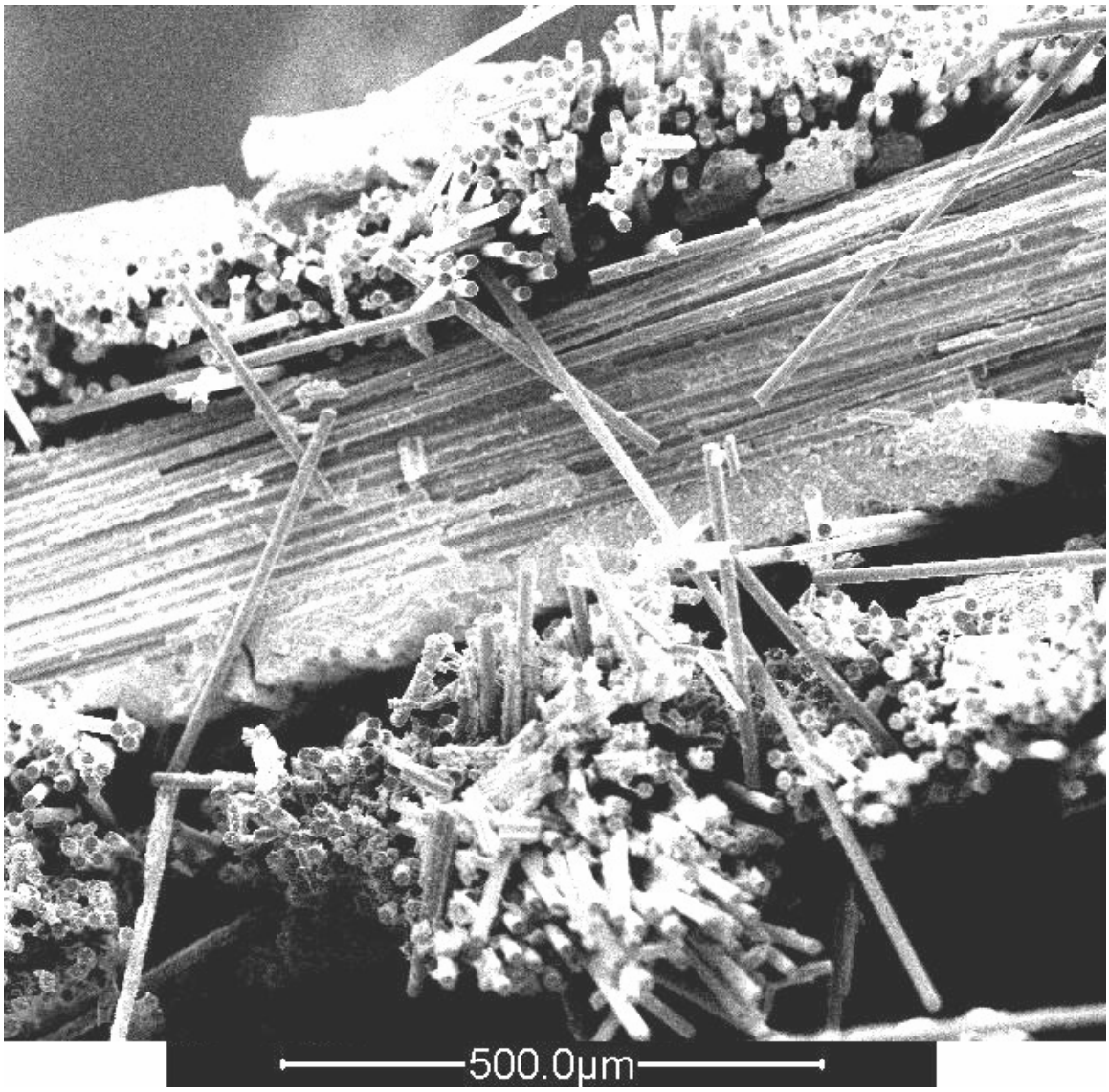

Figure 34. SEM micrograph of Specimen 15, failed under fatigue loading conditions in steam at 170 MPa at 1200°C.

The SEM micrographs shown here, coming from specimens tested in fatigue under a variety of conditions, do not reveal a trend in the failure mechanisms of the oxide-oxide material as it is exposed to higher stress levels with and without steam.

IV. Conclusions and Recommendations

4.1. Conclusions

The Nextel 720/Alumina material exhibits excellent fatigue resistance at 1200°C in the laboratory air environment. As expected, the fatigue life of the material decreases as the maximum load is increased. Exposure to a steam environment and/or higher temperature (1330°C) results in reduced fatigue life. Therefore, even though the material is already oxidized, it is not immune to the corrosive effects of steam.

A decrease in stiffness of the oxide-oxide material was observed for tests conducted in both 1200 and 1330°C as the cycles progressed. The modulus decreased at a higher rate in the presence of steam. At 1200°C, the modulus generally decreases faster at higher stress levels. At 1300°C, reduction in modulus was independent of fatigue stress level.

The hysteretic energy density decreases as the cycles progress until reaching saturation at both 1200 and 1330°C. Presence of steam does not significantly affect the HED behavior with cycling.

All specimens showed accumulation of strain with cycles. The tests conducted at 1330°C accumulated more strain than those conducted at 1200°C. The strain accumulation was greater in air (which had longer fatigue life) than in steam, indicating that strain accumulation may not provide reliable criteria for fatigue life prediction.

Optical and SEM micrographs of the material reveal that there is no distinct trend in the fracture surfaces of the specimen with either increasing stress or in air or steam environments. Both fiber bundle failure and individual fiber pullout is visible in fracture surfaces produced by all of the specimens tested in this effort.

The material retains 100% of its strength when subjected to prior fatigue at 1200°C in air. The presence of steam noticeably degrades its fatigue performance. While N720/A shows considerable improvement in performance when compared to other CMCs, caution must be exercised when considering this material for application, where it would be subjected to repetitive loading at elevated temperatures in oxidizing environments.

4.2. Recommendations for Future Research

As was noted in Section 3.5.4, residual strength testing showed that the ultimate strength of the material was lower when the fatigue test achieving run-out was conducted in a steam environment. This indicates that there is some degradation of the material, even though it did achieve run-out. Future studies could include high-cycle fatigue to determine fatigue life at the given stress levels.

In addition, this effort only tested one specimen at each load level in the varying temperature and steam environments. Although these tests produced consistent results, repeating the tests with a greater number of specimens for each test condition would serve to further validate and give statistical significance to the results presented here.

Appendix A: Addition SEM Micrographs

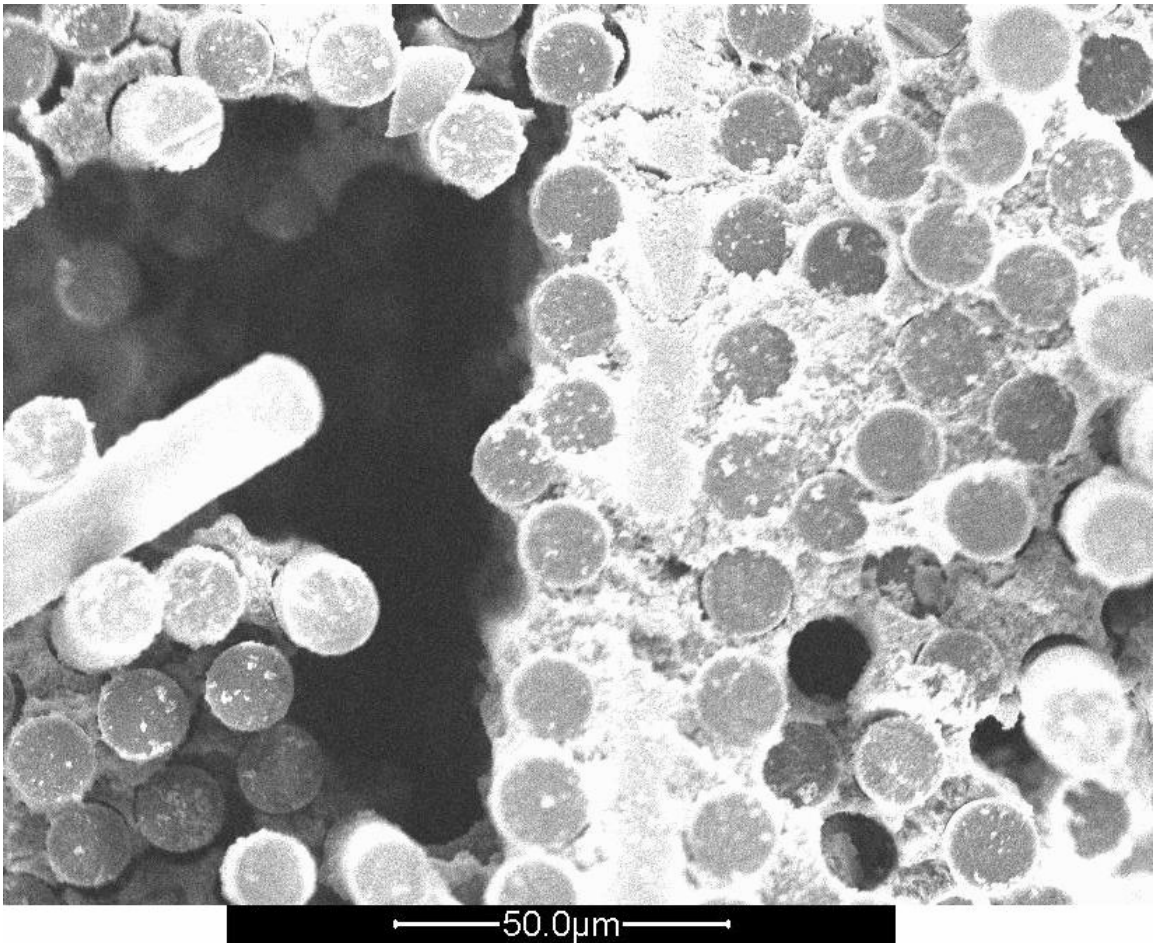

Figure 35. SEM micrograph of a fracture surface of Specimen 2, monotonic tension to failure at 1200°C. Shows both fiber tow pullout and individual fiber pullout.

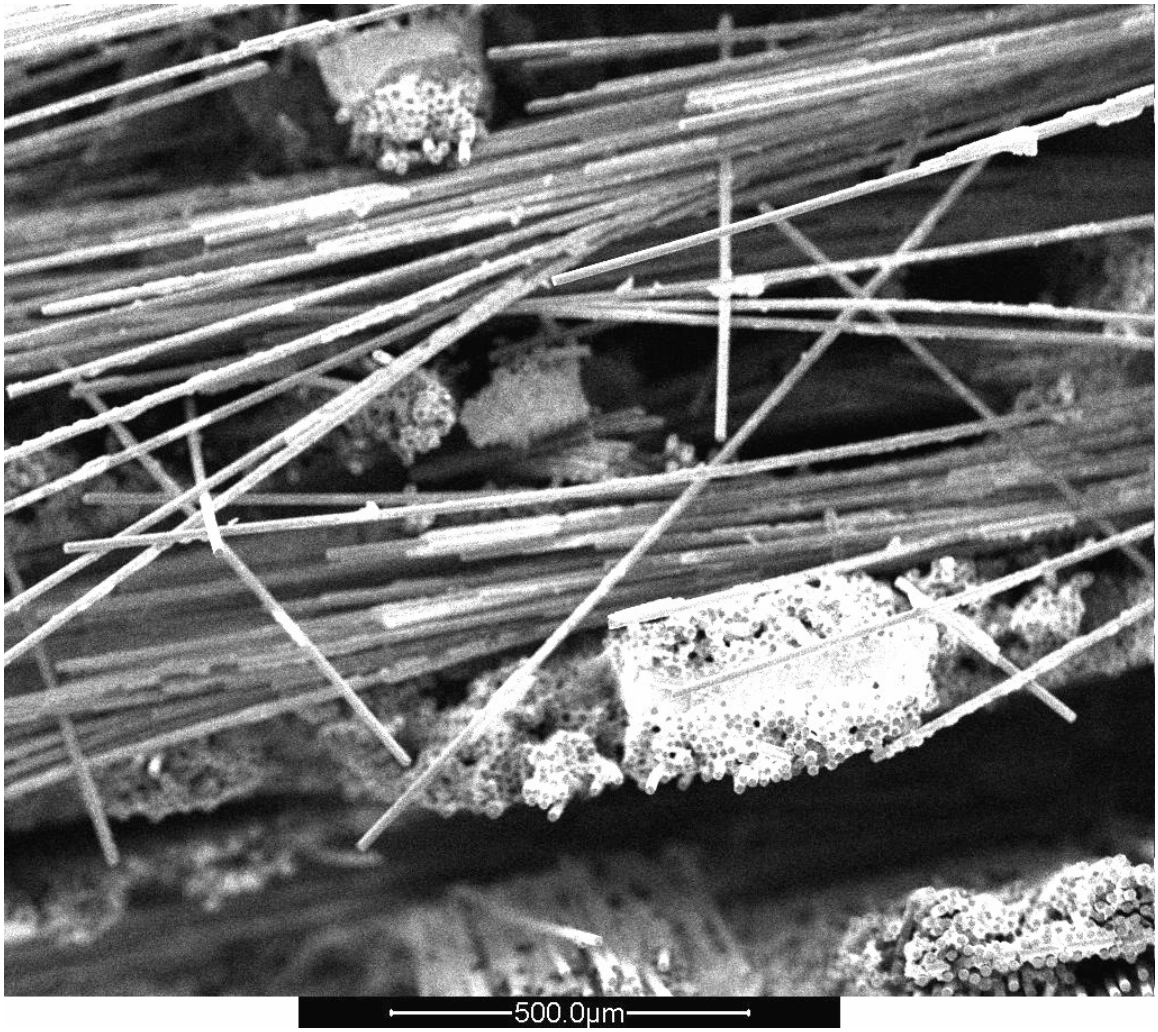

Figure 36. SEM micrograph of Specimen 6, failed in monotonic tension testing following 120,199 cycles of fatigue loading (defined as a run-out) with maximum stress of 100 MPa in air at 1200°C.

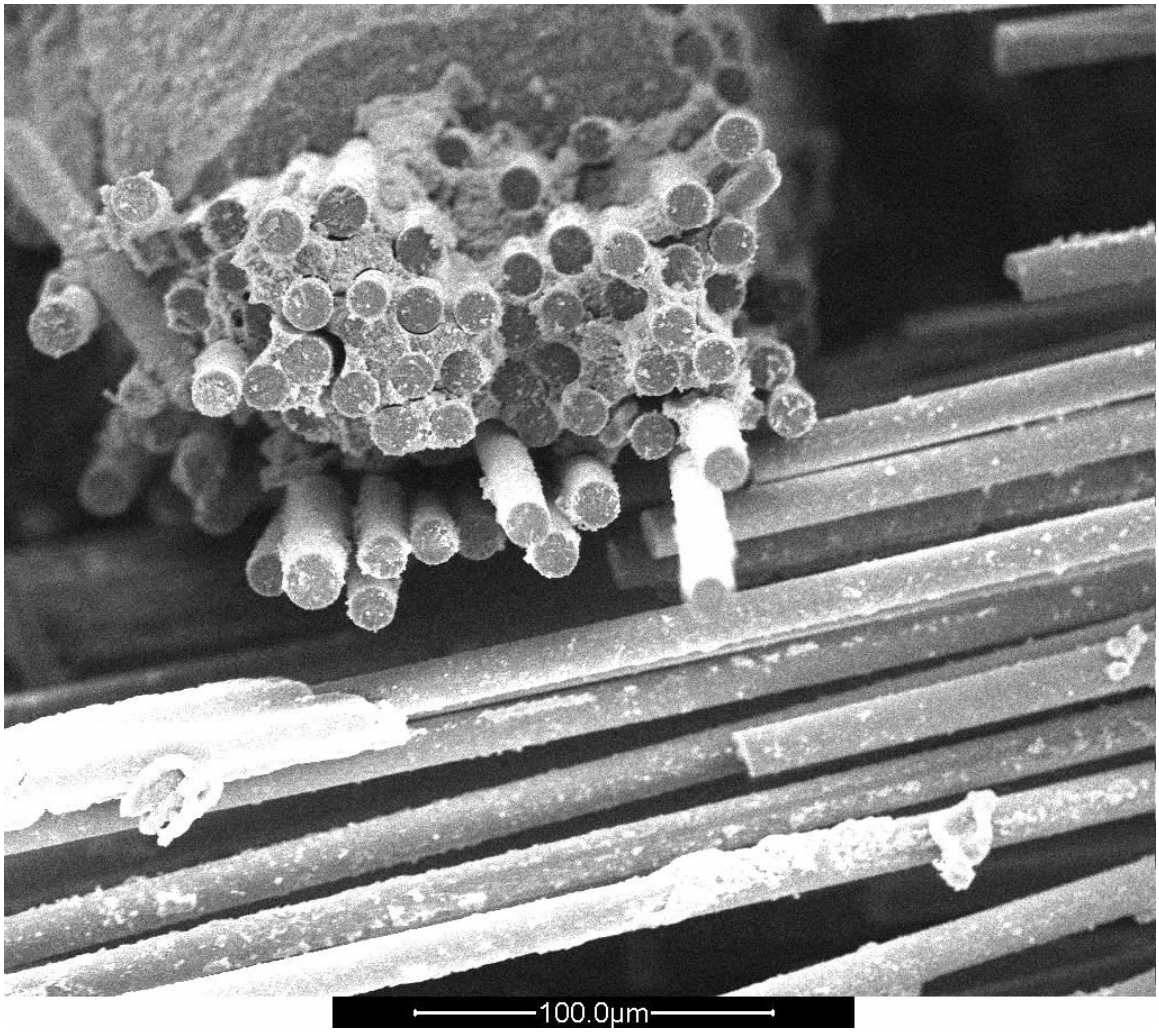

Figure 37. SEM micrograph of Specimen 6, failed in monotonic tension testing following 120,199 cycles of fatigue loading (defined as a run-out) with maximum stress of 100 MPa in air at 1200°C.

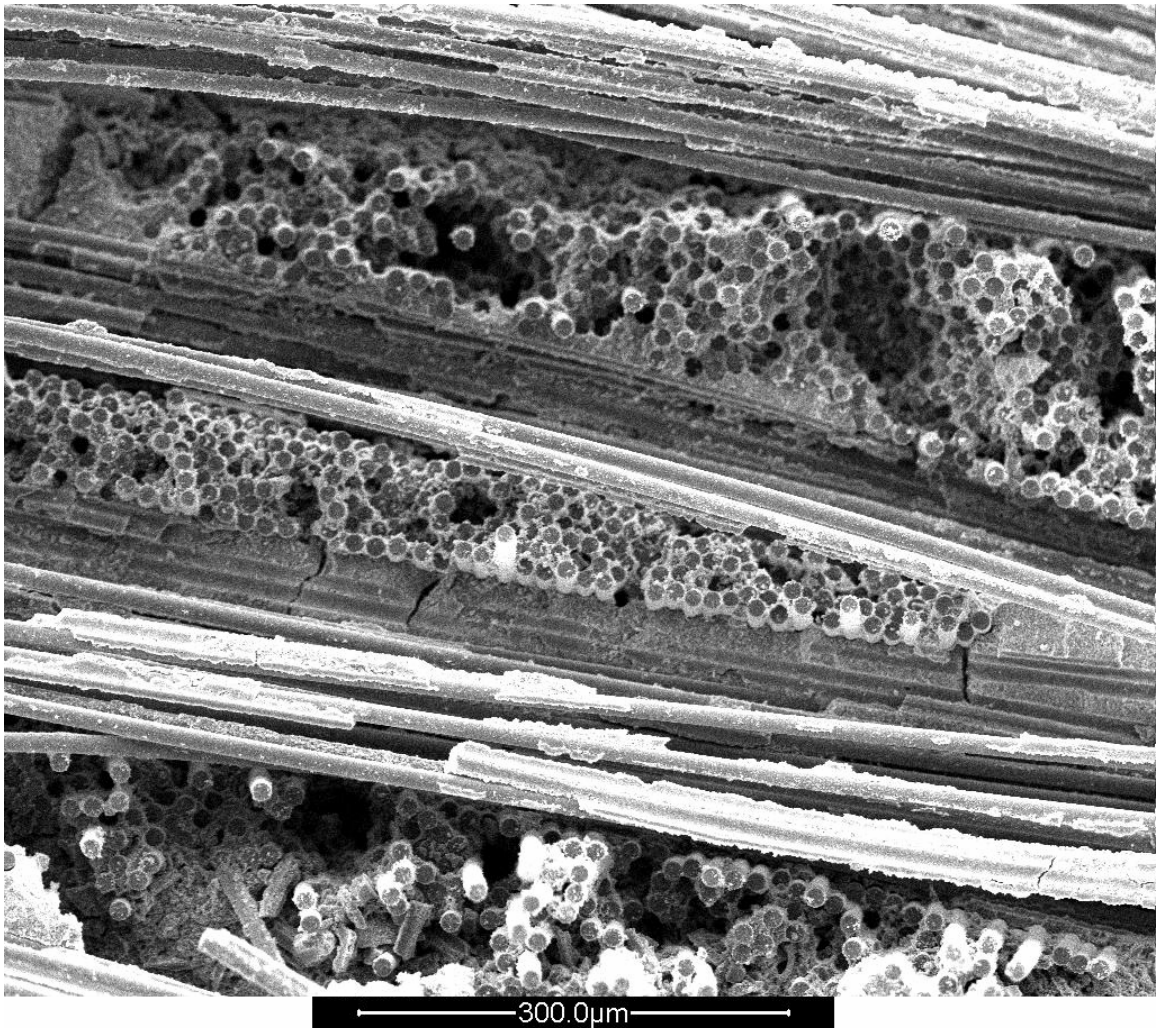

Figure 38. SEM micrograph of Specimen 7, failed in monotonic tension testing following 146,392 cycles of fatigue loading (defined as a run-out) with maximum stress of 125 MPa in air at 1200°C.

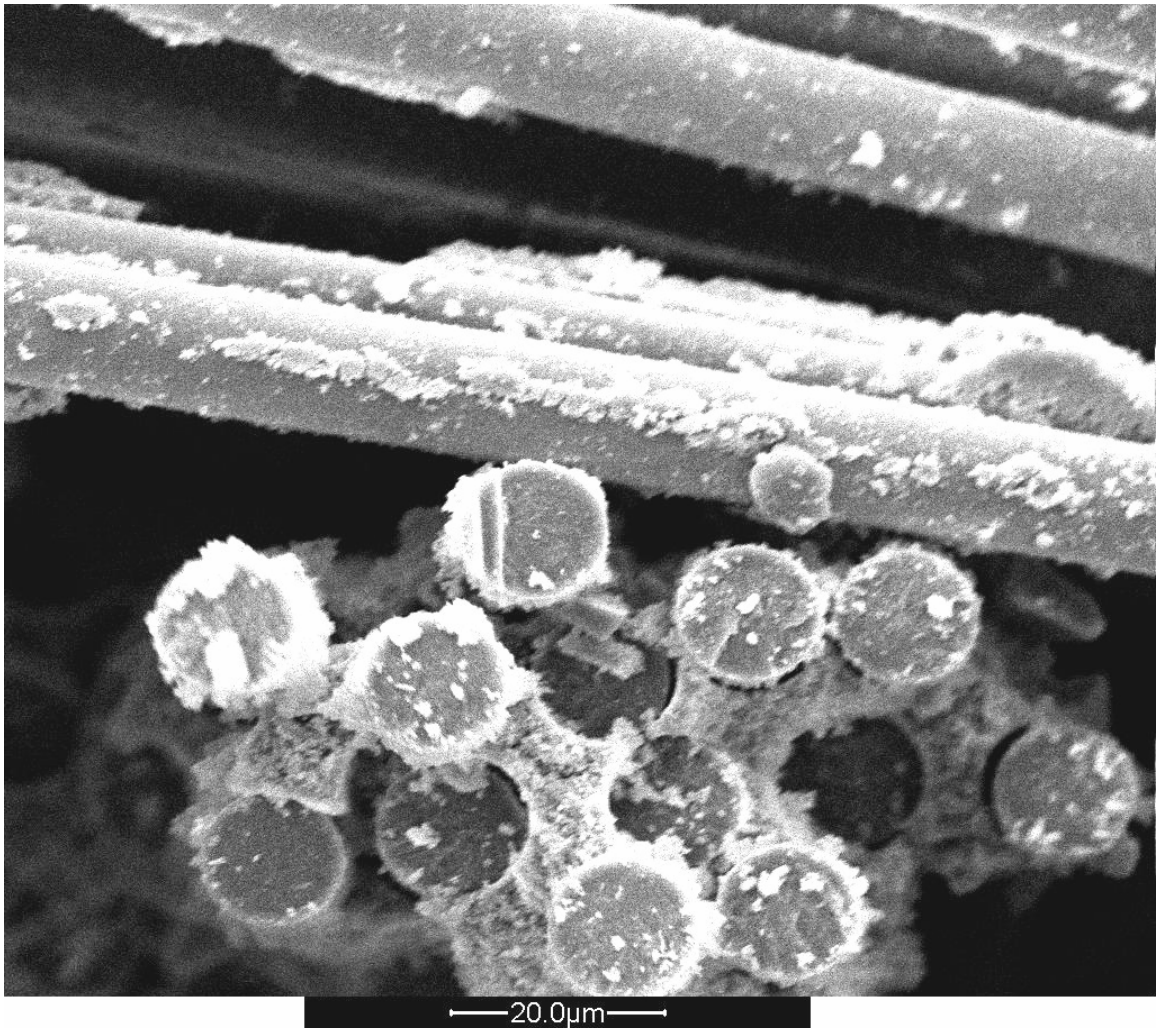

Figure 39. SEM micrograph of Specimen 7, failed in monotonic tension testing following 146,392 cycles of fatigue loading (defined as a run-out) with maximum stress of 125 MPa in air at 1200°C.

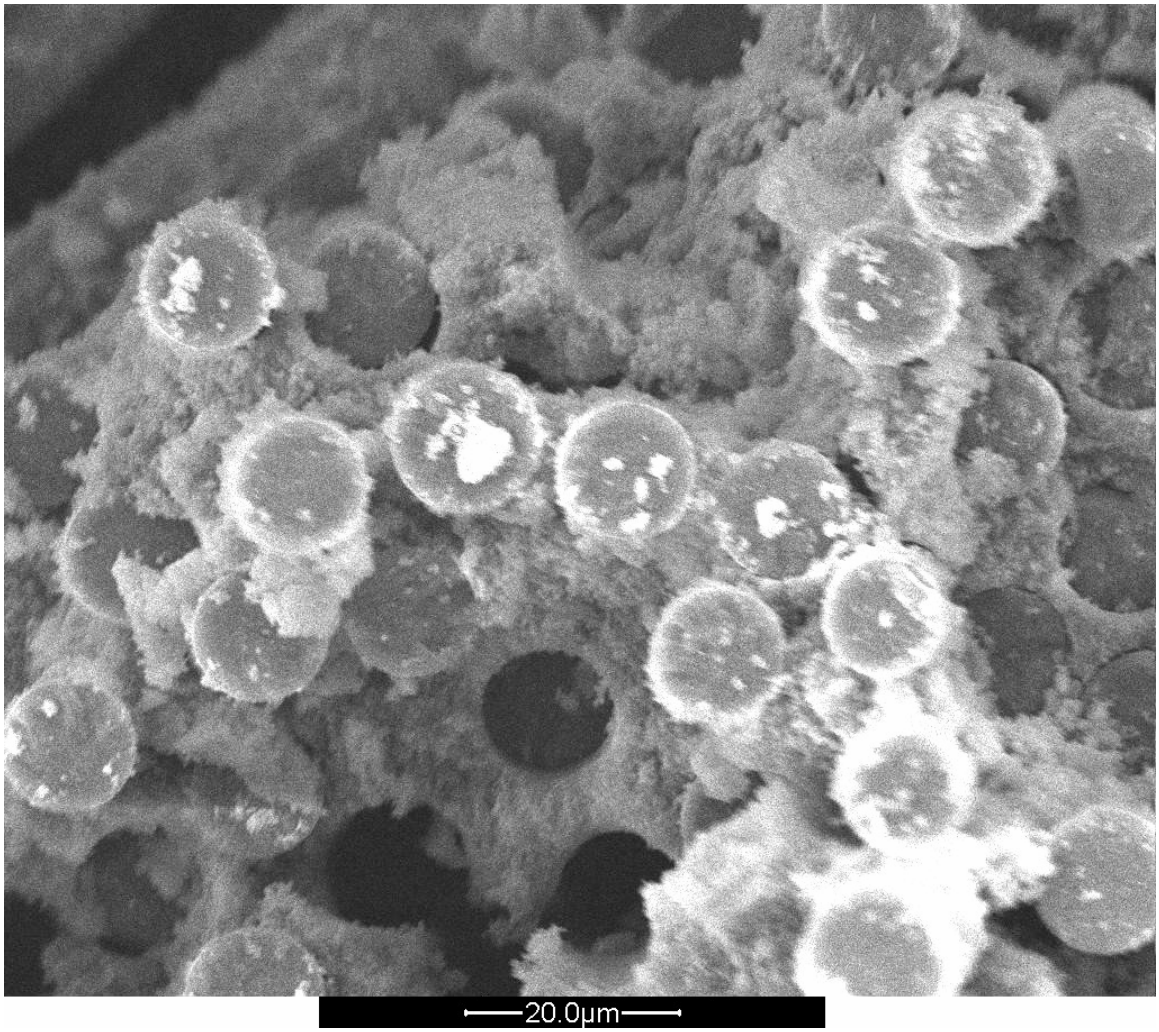

Figure 40. SEM micrograph of Specimen 8, failed in monotonic tension testing following 167,473 cycles of fatigue loading (defined as a run-out) with maximum stress of 150 MPa in air at 1200°C.

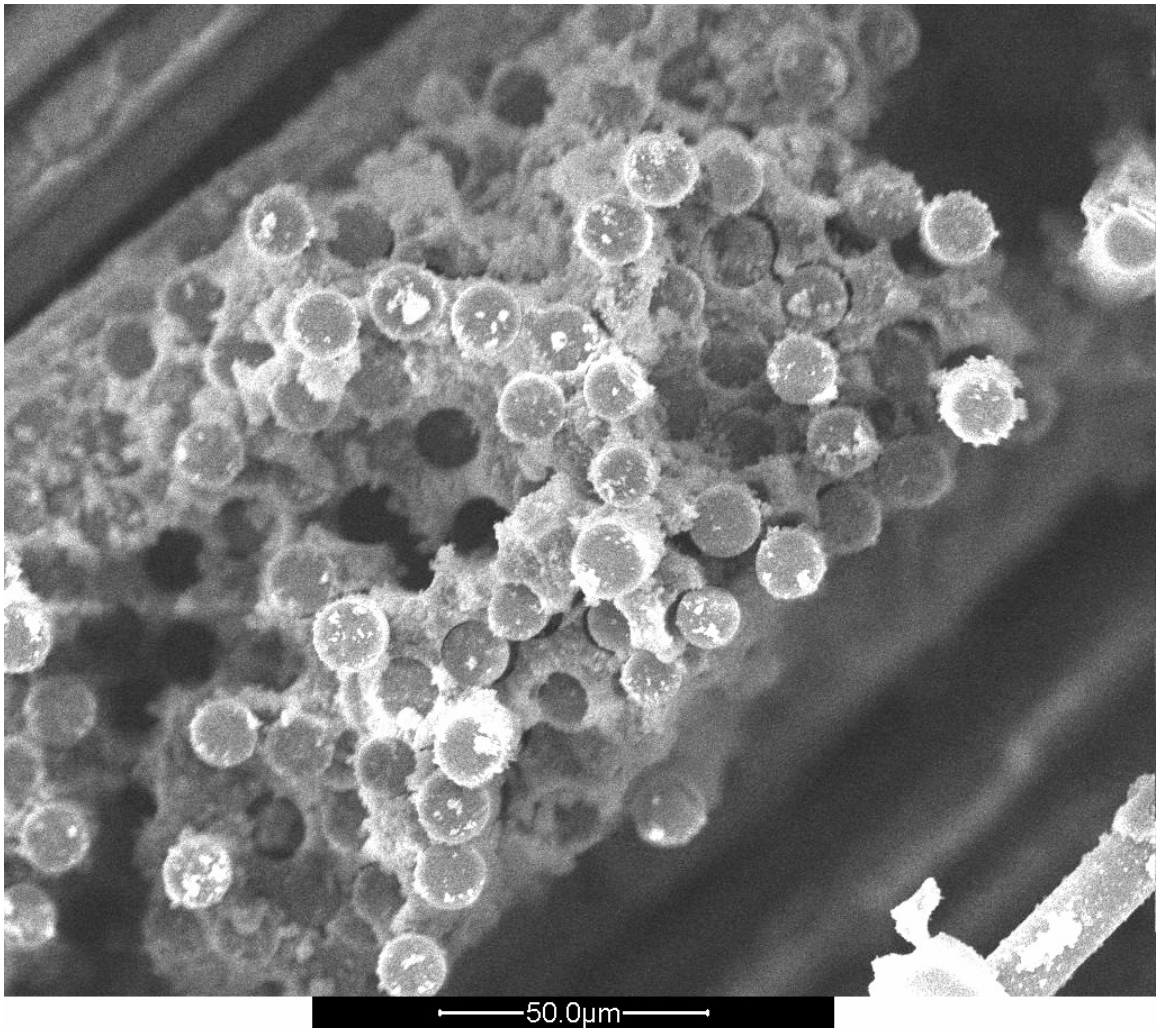

Figure 41. SEM micrograph of Specimen 8, failed in monotonic tension testing following 167,473 cycles of fatigue loading (defined as a run-out) with maximum stress of 150 MPa in air at 1200°C.

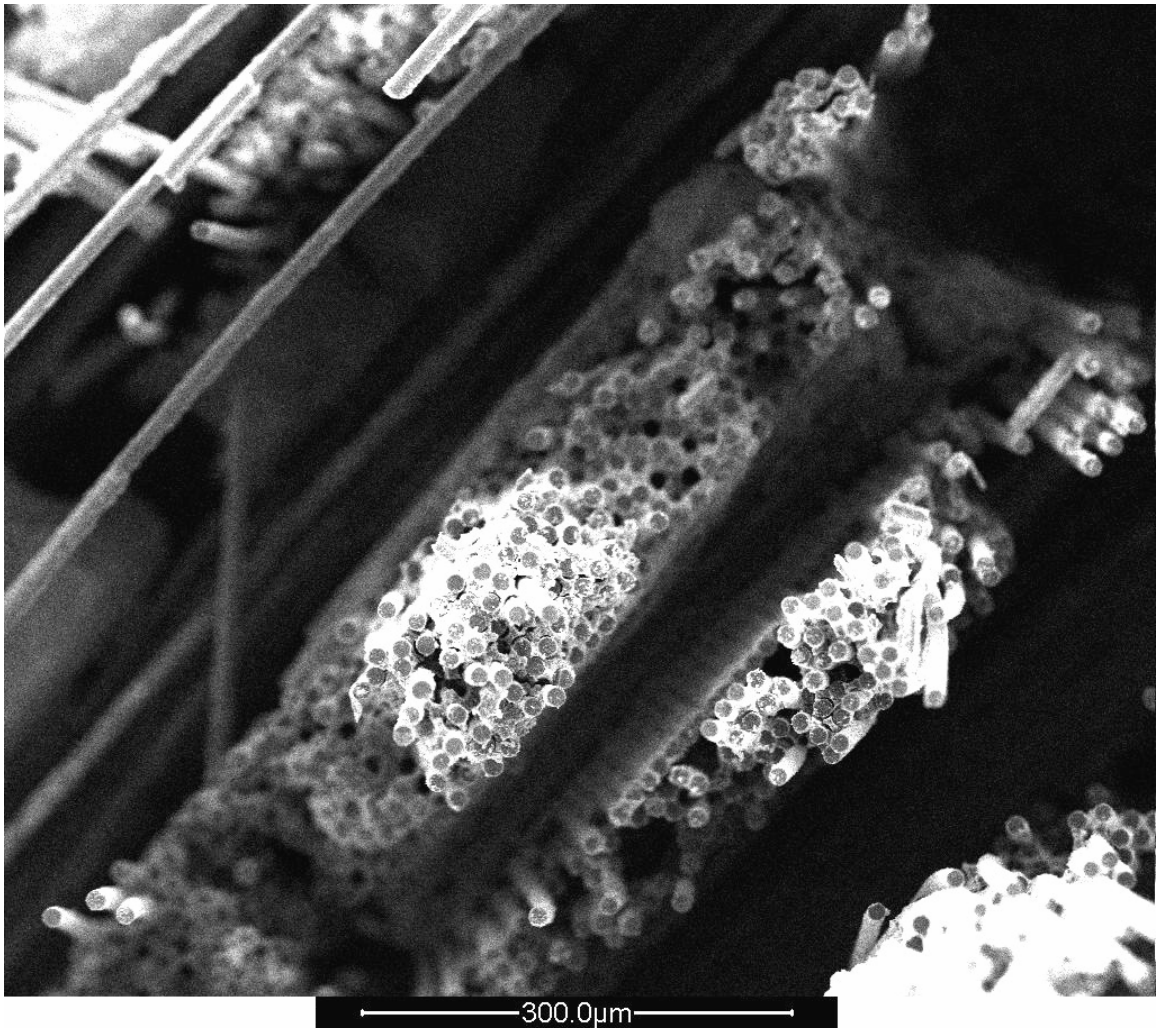

Figure 42. SEM micrograph of Specimen 8, failed in monotonic tension testing following 167,473 cycles of fatigue loading (defined as a run-out) with maximum stress of 150 MPa in air at 1200°C.

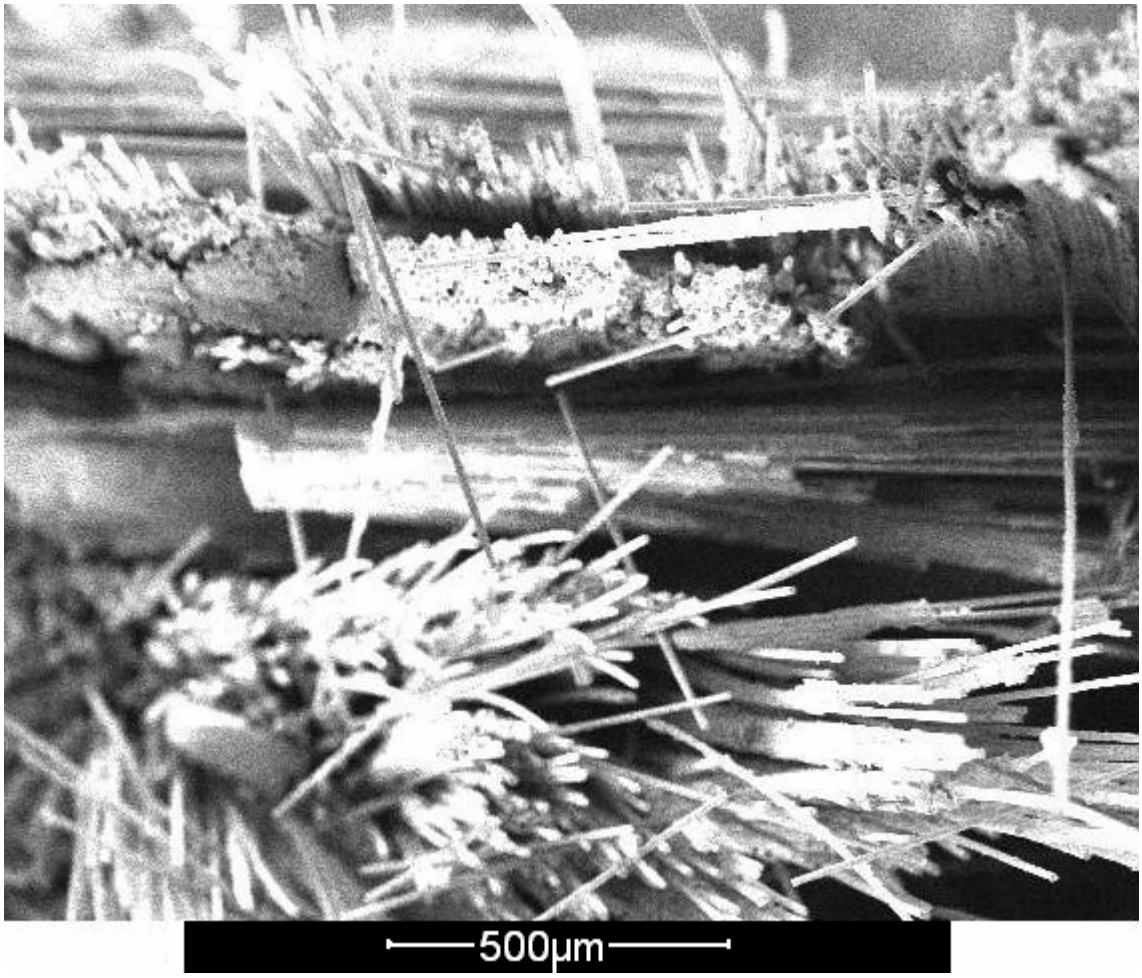

Figure 43. SEM micrograph of Specimen 9, failed in monotonic tension testing following 109,436 cycles of fatigue loading (defined as a run-out) with maximum stress of 170 MPa in air at 1200°C.

Figure 44. SEM micrograph of Specimen 12, failed in monotonic tension testing following 100,780 cycles of fatigue loading (defined as a run-out) with maximum stress of 100 MPa in steam at 1200°C.

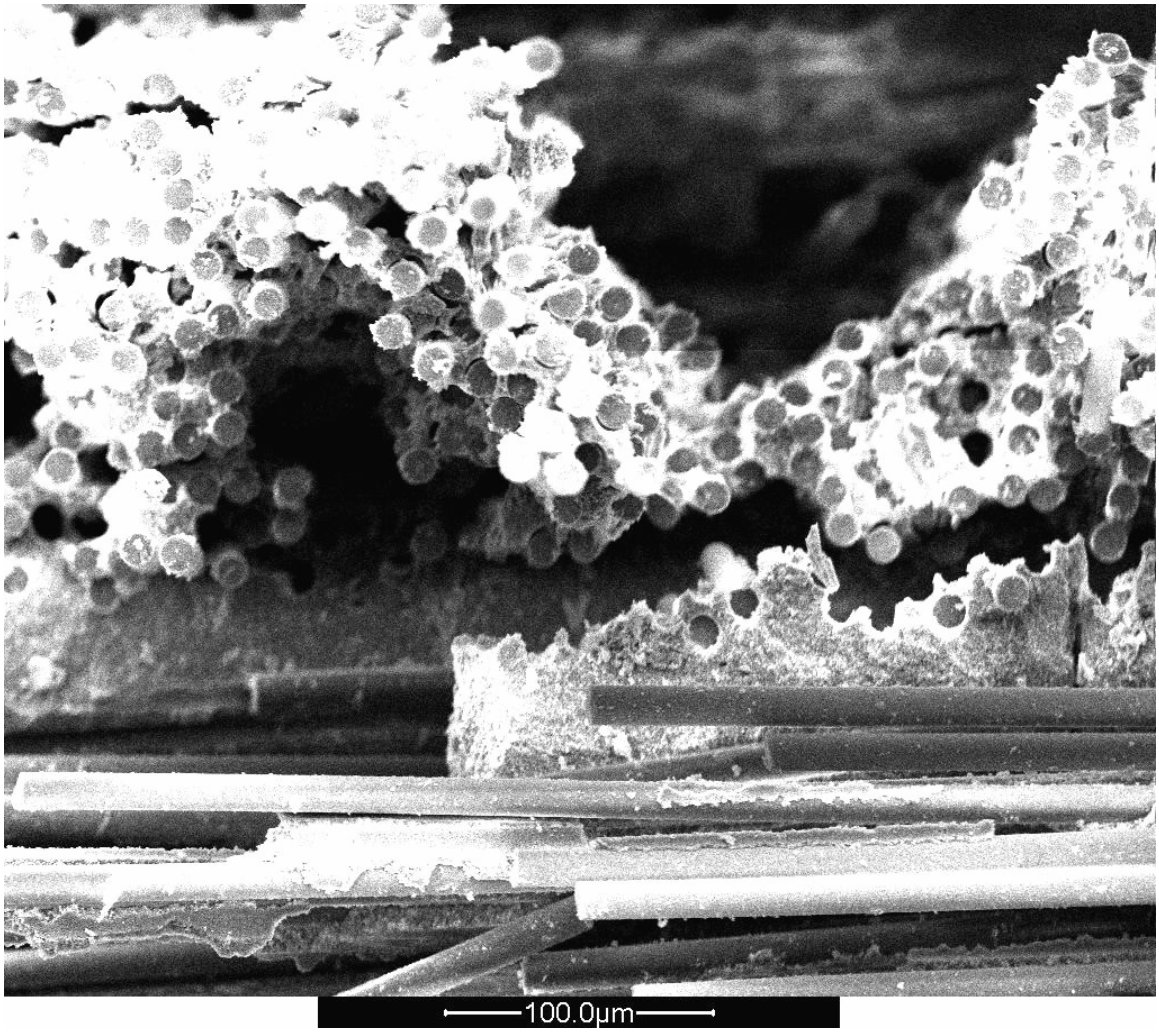

Figure 45. SEM micrograph of Specimen 12, failed in monotonic tension testing following 100,780 cycles of fatigue loading (defined as a run-out) with maximum stress of 100 MPa in steam at 1200°C.

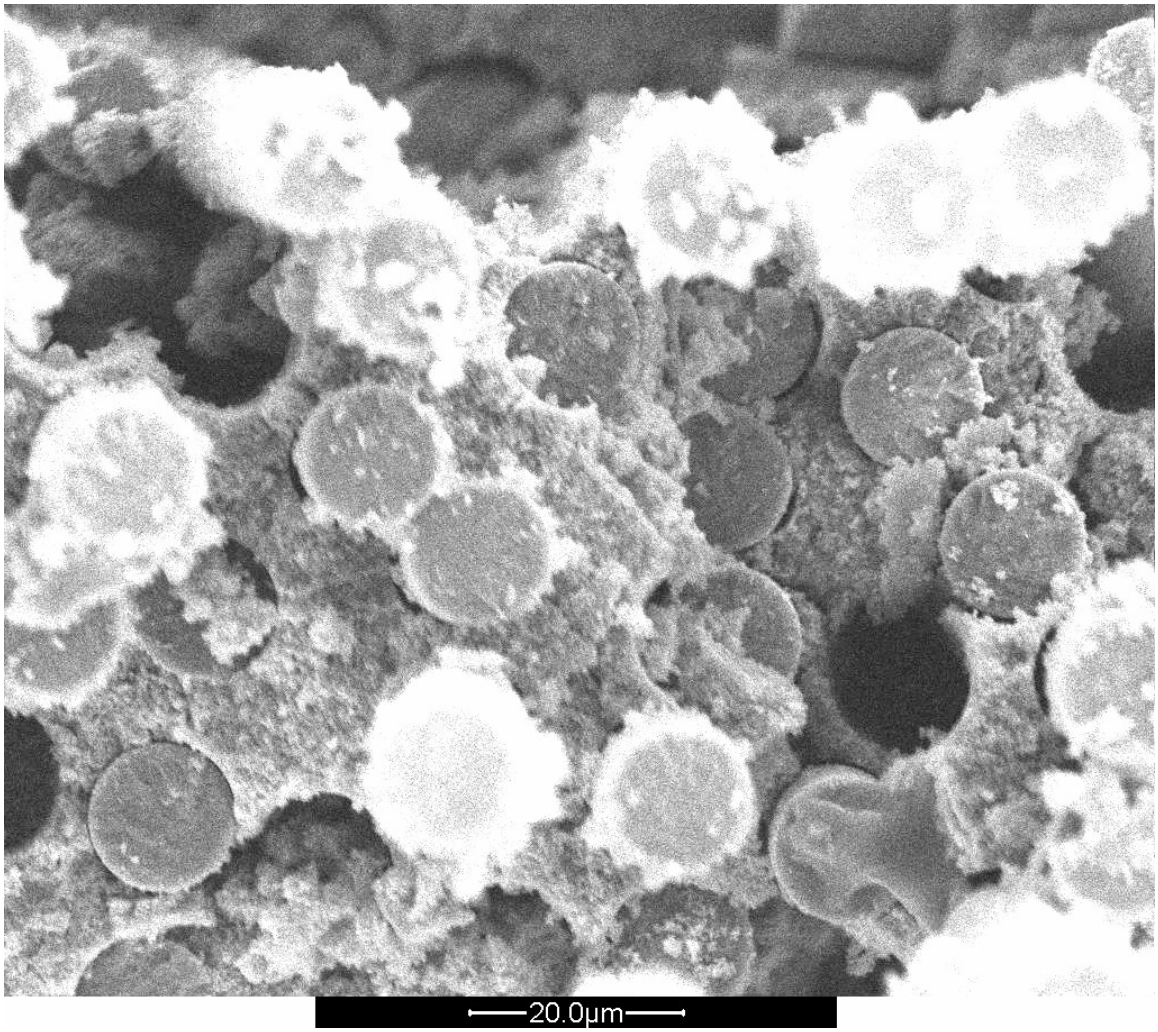

Figure 46. SEM micrograph of Specimen 13, failed in monotonic tension testing following 166,326 cycles of fatigue loading (defined as a run-out) with maximum stress of 125 MPa in steam at 1200°C.

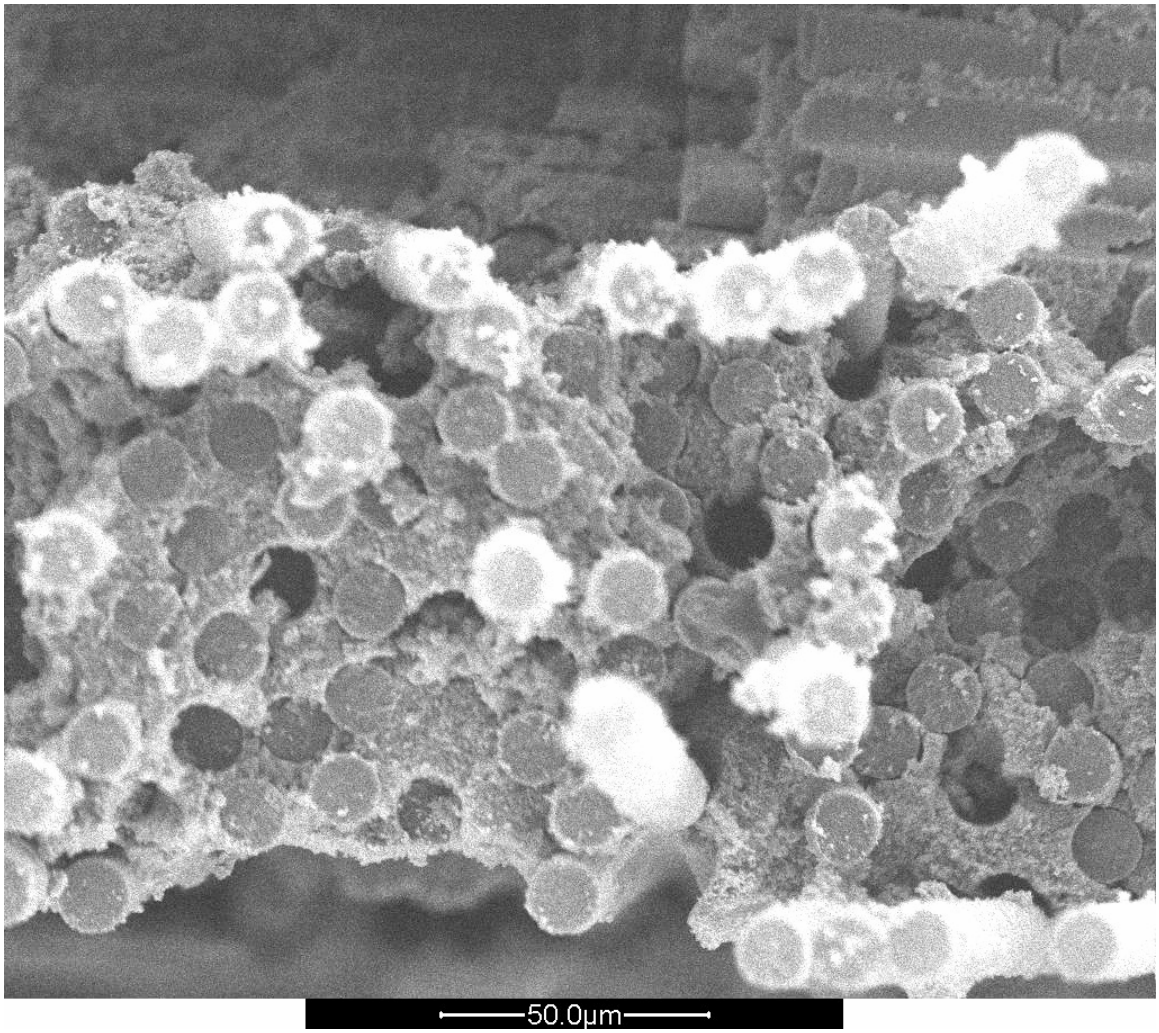

Figure 47. SEM micrograph of Specimen 13, failed in monotonic tension testing following 166,326 cycles of fatigue loading (defined as a run-out) with maximum stress of 125 MPa in steam at 1200°C.

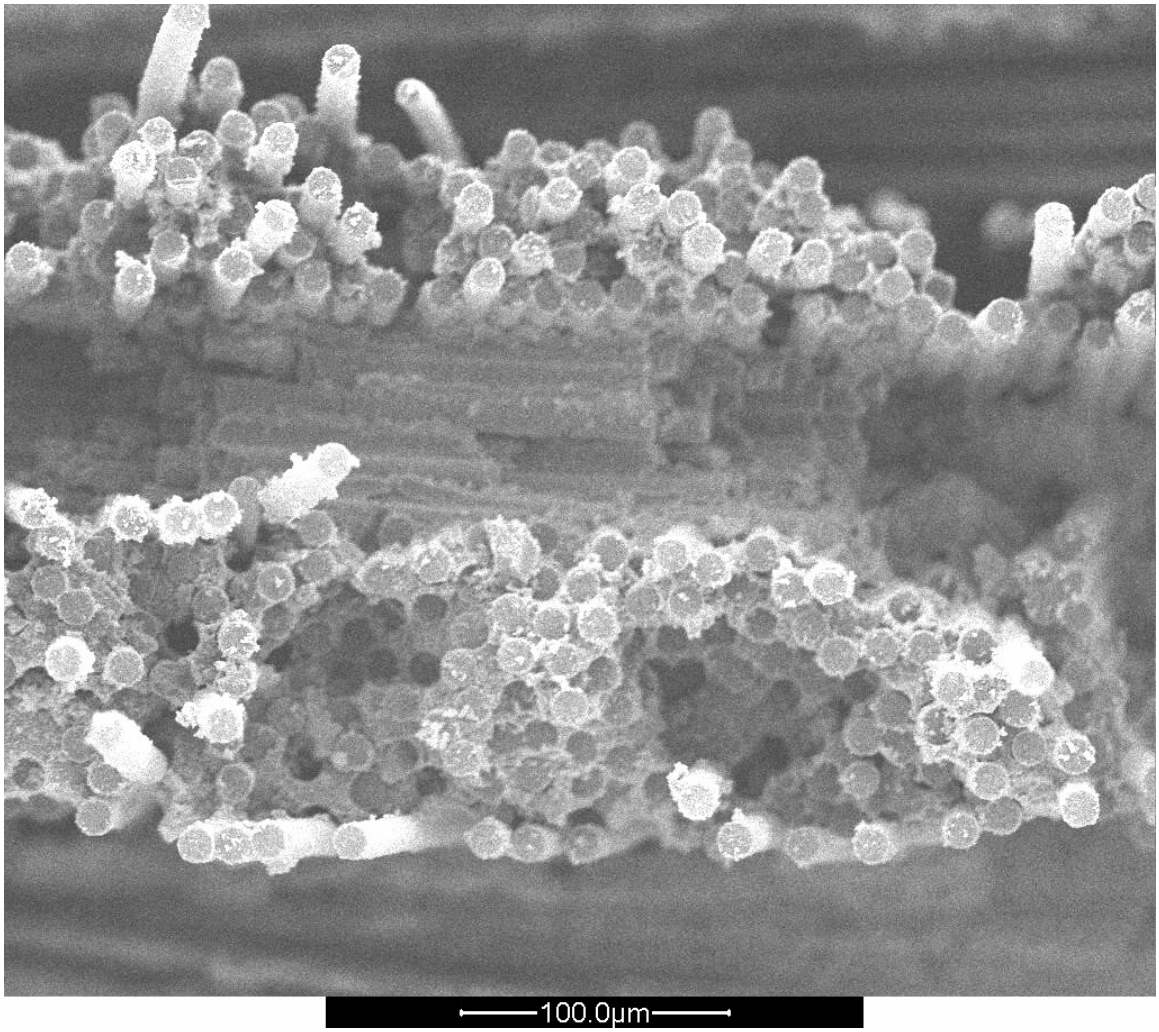

Figure 48. SEM micrograph of Specimen 13, failed in monotonic tension testing following 166,326 cycles of fatigue loading (defined as a run-out) with maximum stress of 125 MPa in steam at 1200°C.

Figure 49. SEM micrograph of Specimen 14, failed in fatigue loading at 150 MPa in steam at 1200°C.

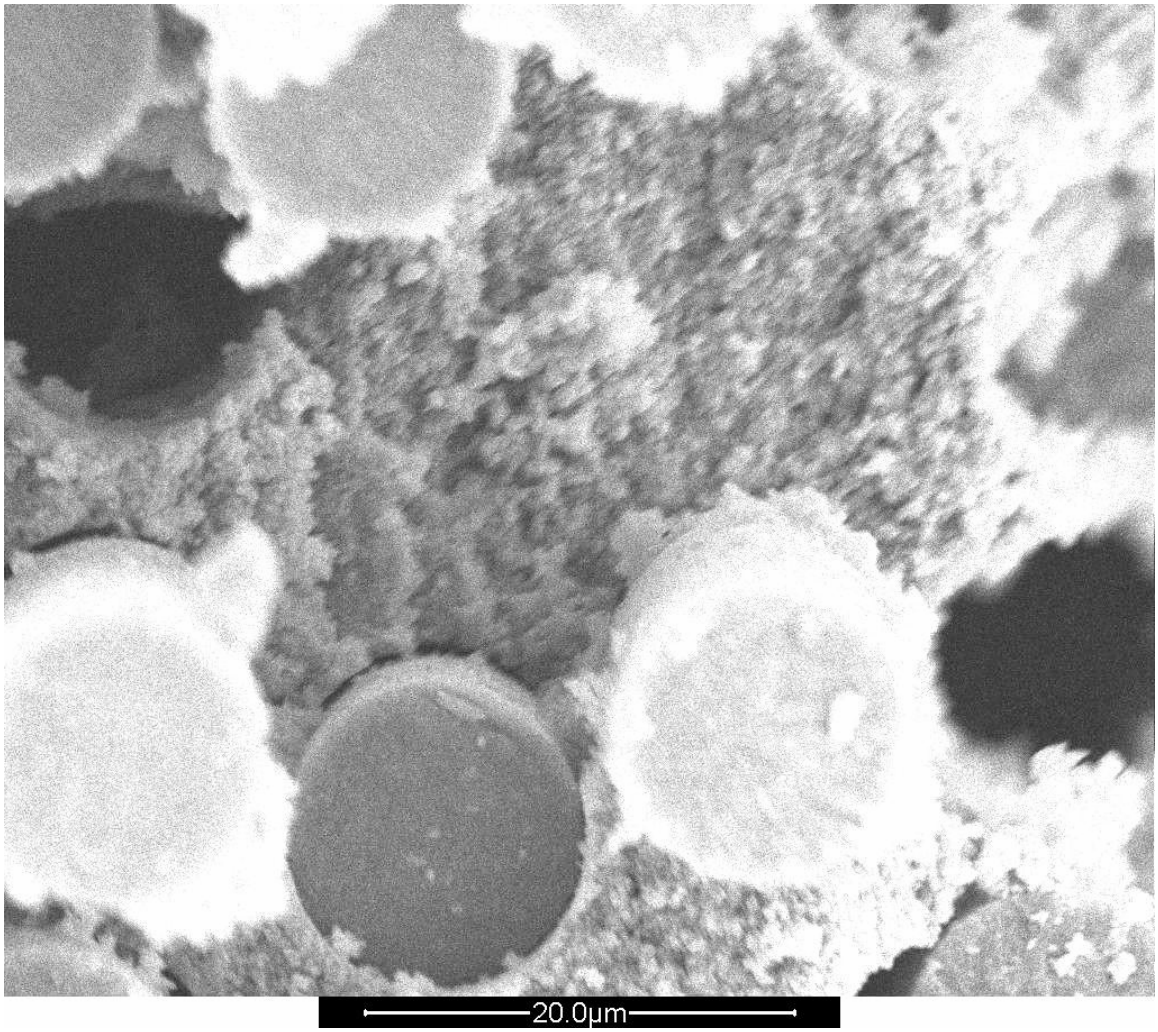

Figure 50. SEM micrograph of Specimen 14, failed in fatigue loading with maximum stress of 150 MPa in steam at 1200°C.

Figure 51. SEM micrograph of Specimen 15, failed during fatigue loading at 170 MPa in steam at 1200°C.

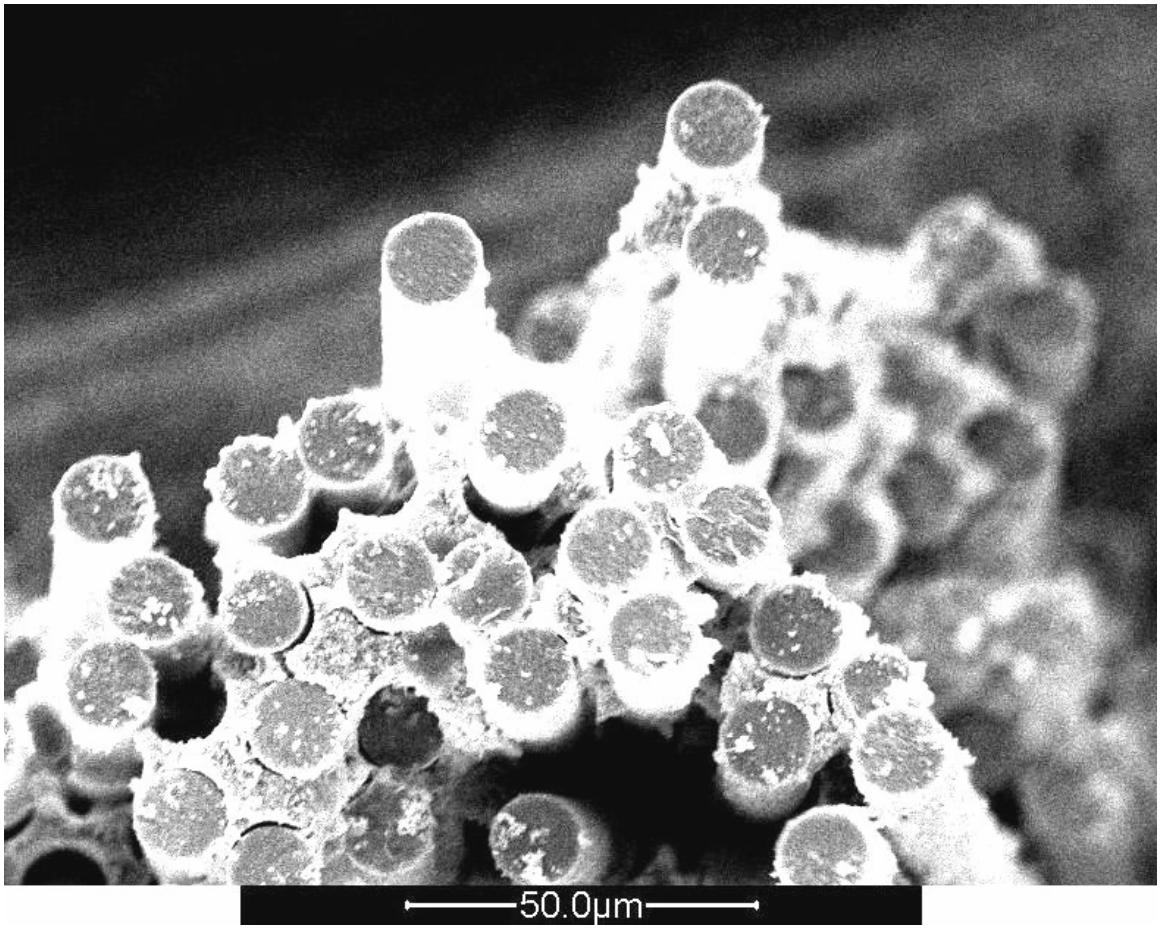

Figure 52. SEM micrograph of Specimen 15, failed in fatigue loading with maximum stress of 170 MPa in steam at 1200°C.

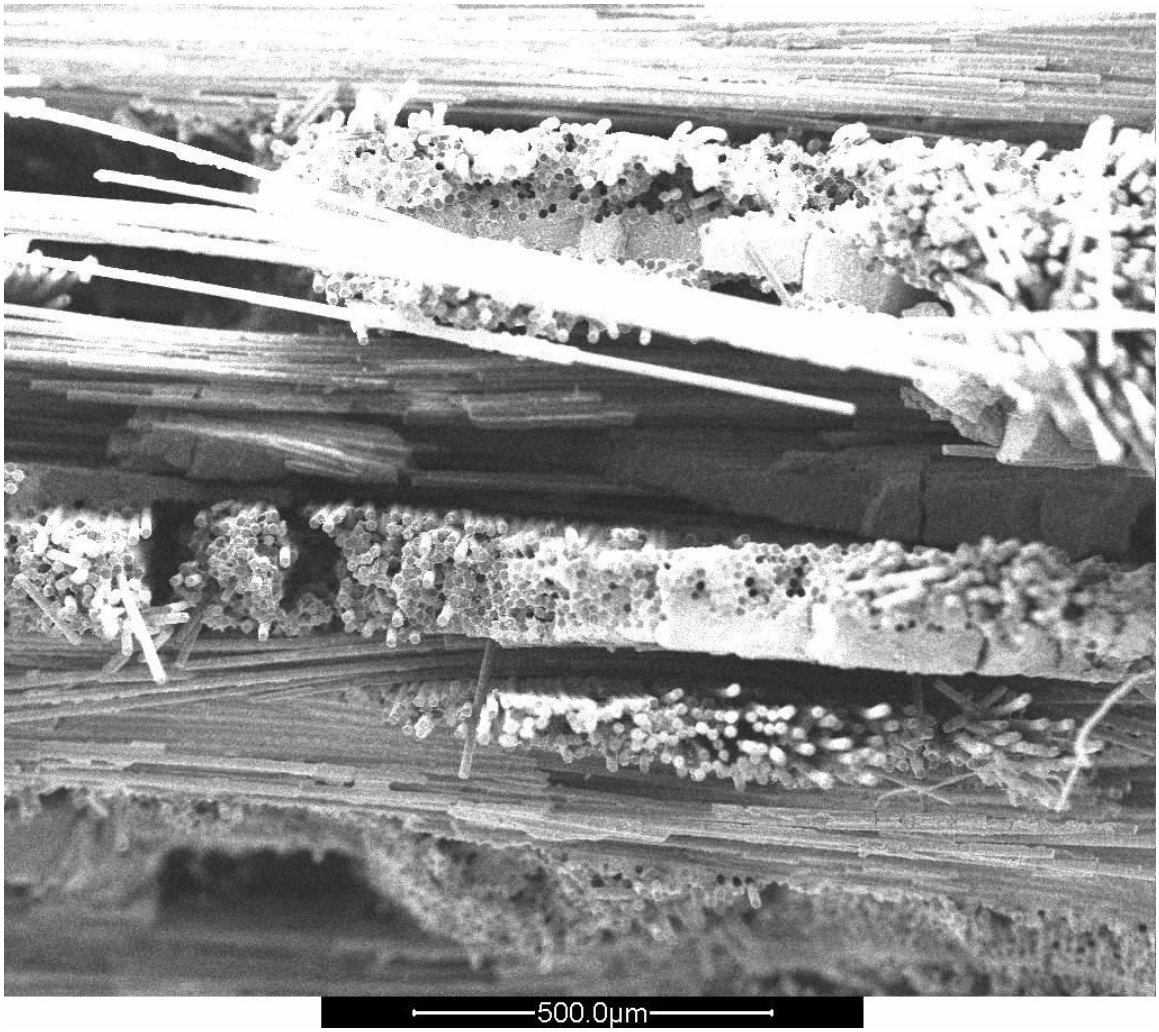

Figure 53. SEM micrograph of Specimen 3, failed in monotonic tension at 1330°C.

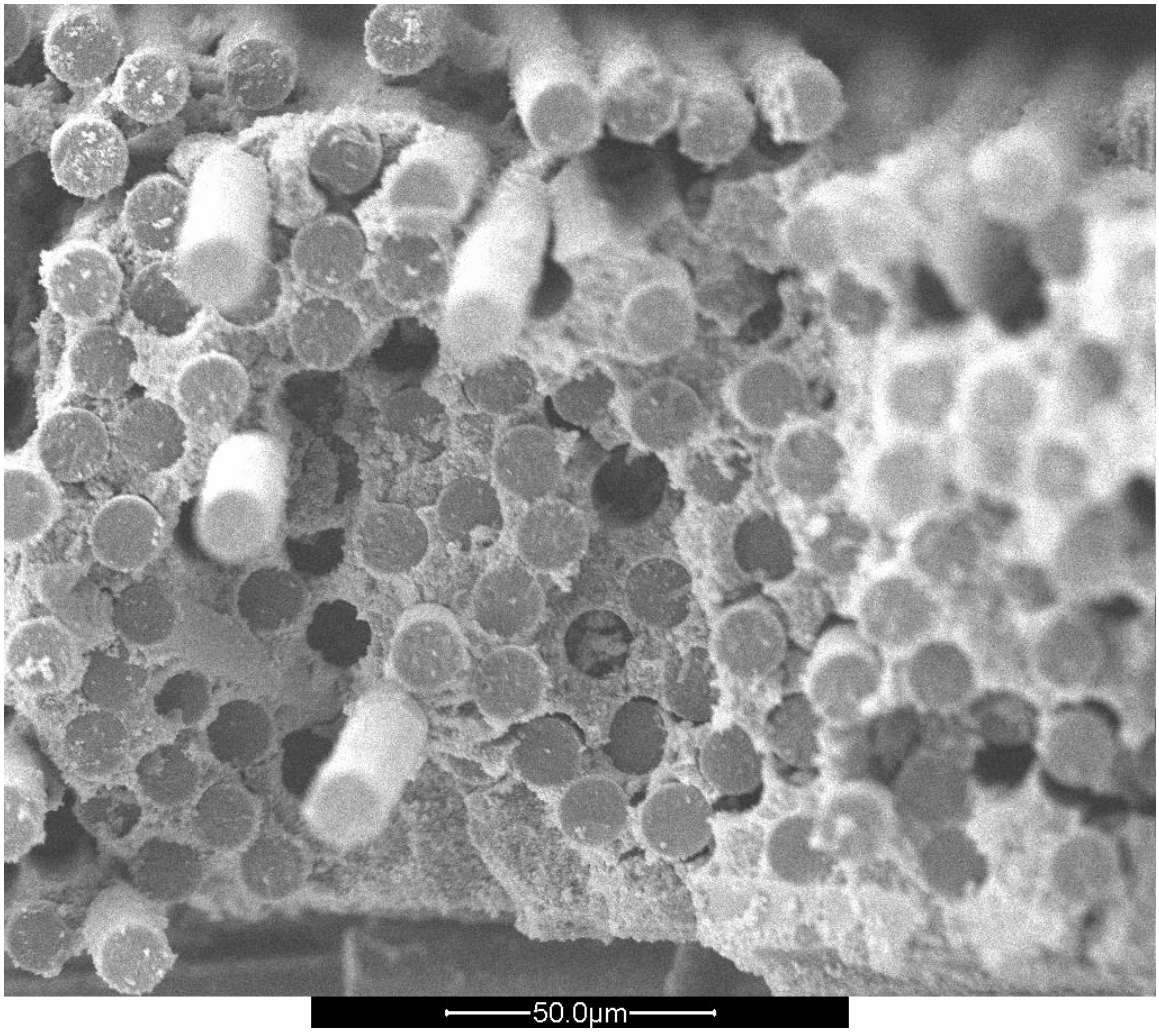

Figure 54. SEM micrograph of Specimen 3, failed in monotonic tension at 1330°C.

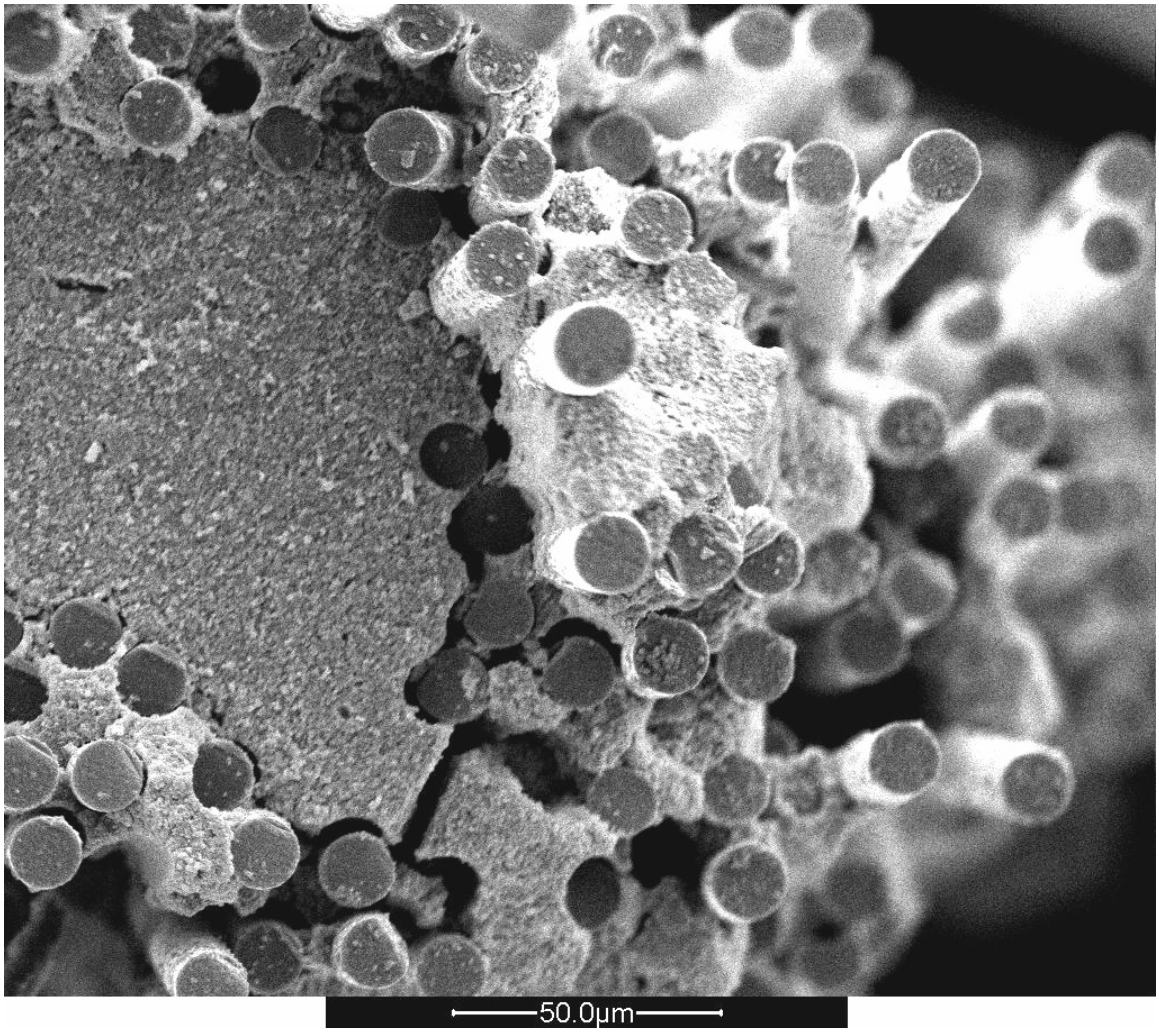

Figure 55. SEM micrograph of Specimen 4, failed in monotonic tension at 1330°C.

Figure 56. SEM micrograph of Specimen 10, failed under fatigue loading conditions with maximum stress of 50 MPa at 1330°C in air.

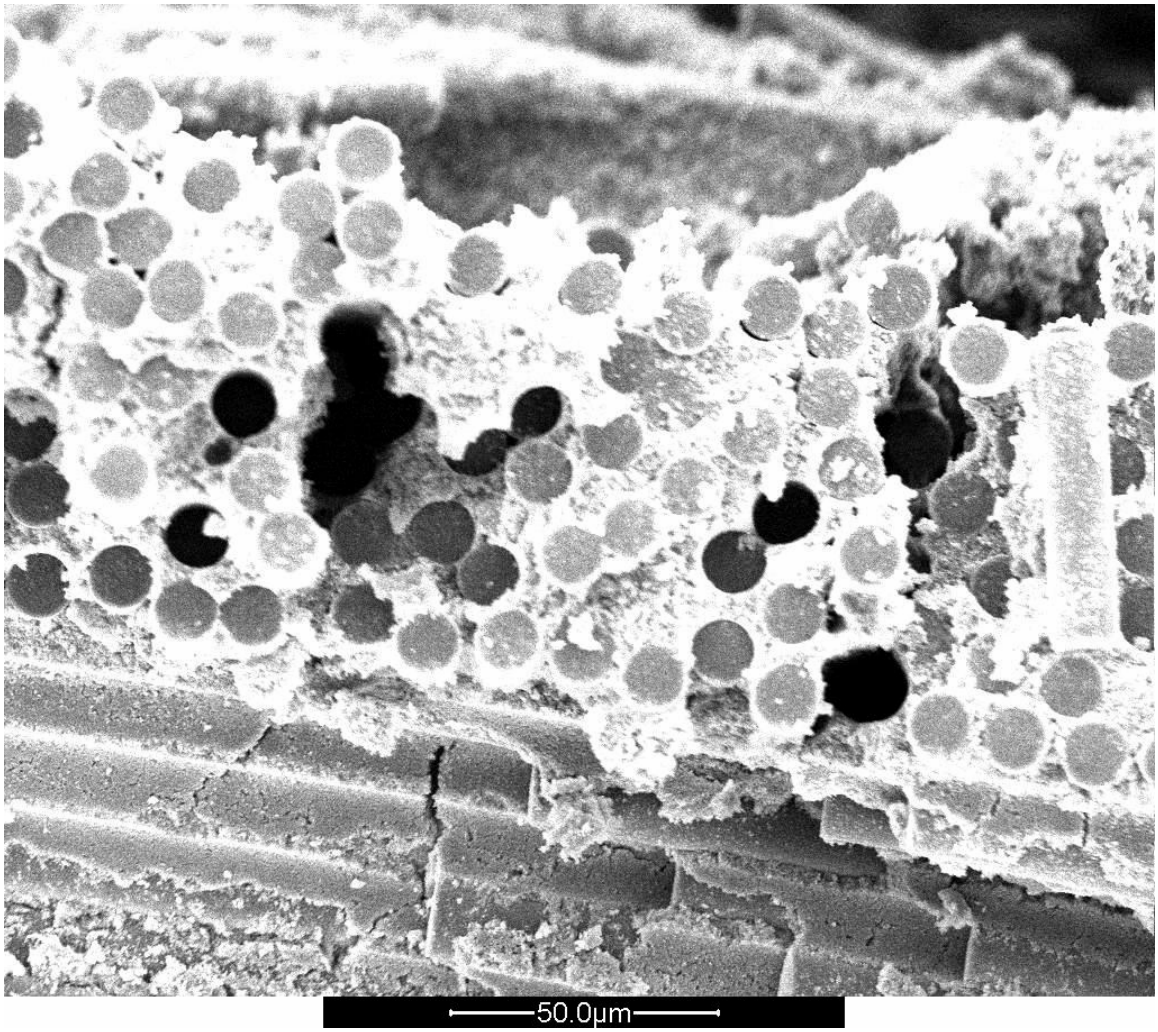

Figure 57. SEM micrograph of Specimen 10, failed during fatigue loading conditions in air at 50 MPa at 1330°C.

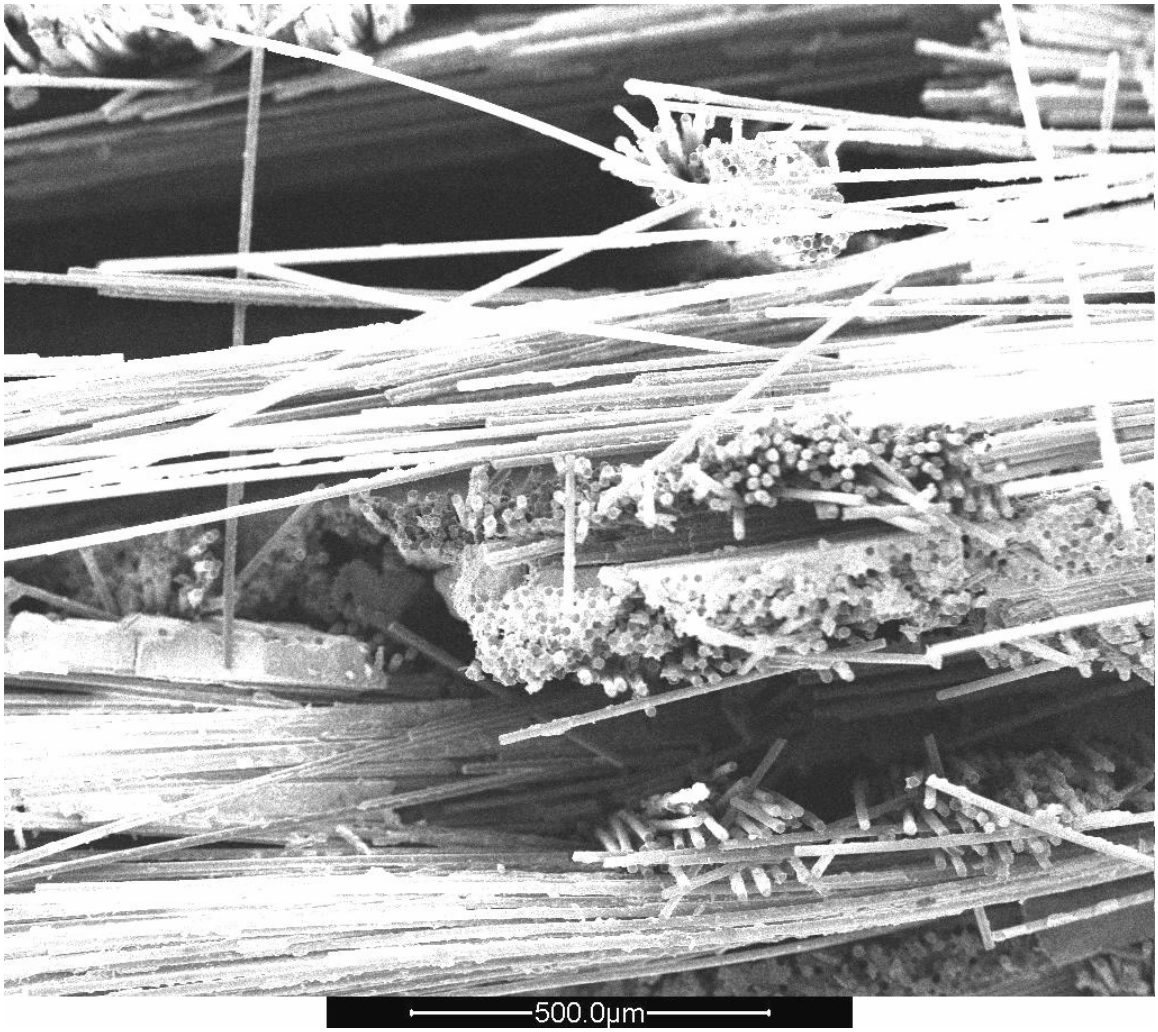

Figure 58. SEM micrograph of Specimen 11 failed under fatigue loading conditions with maximum stress of 100 MPa at 1330°C in air.

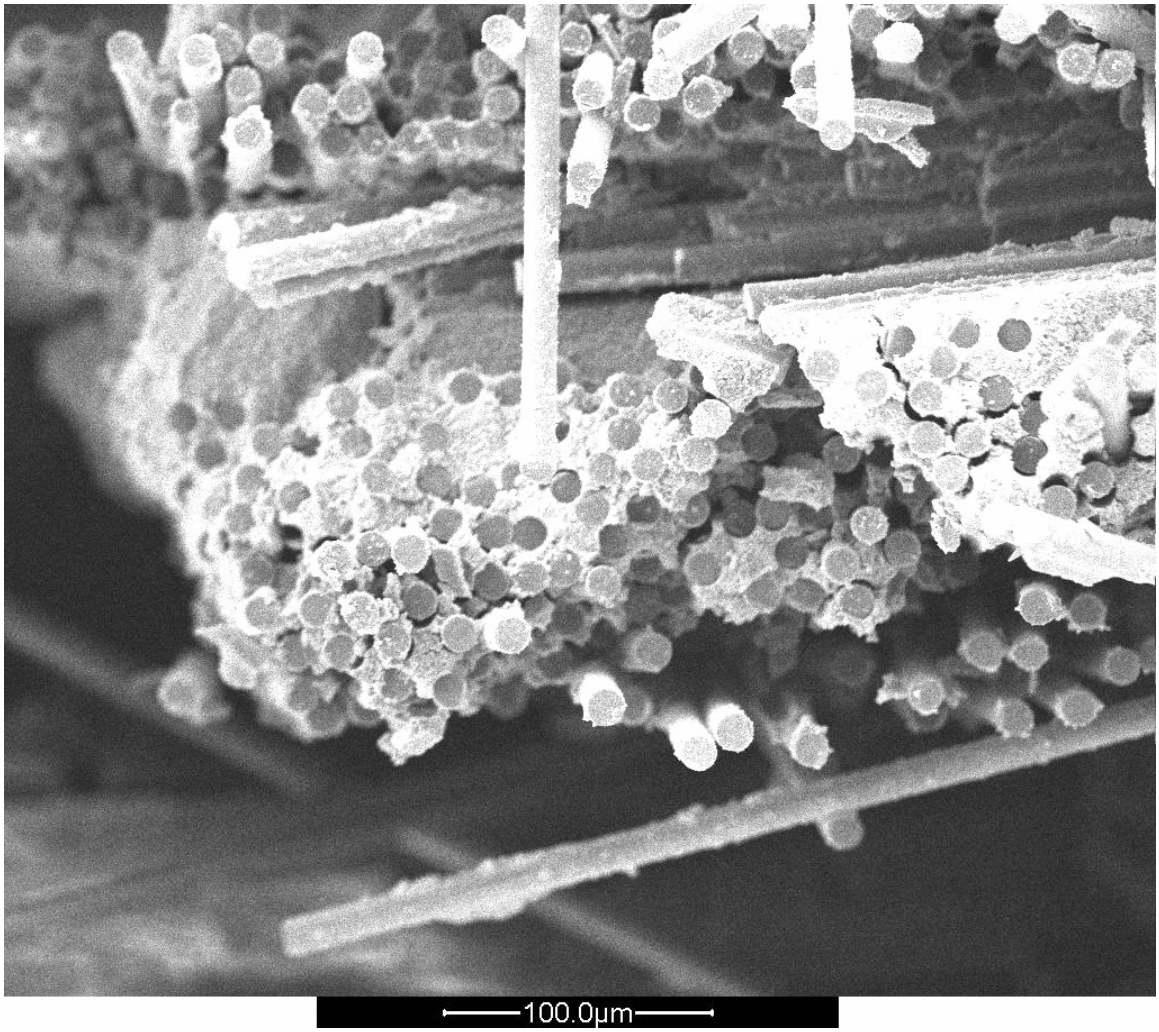

Figure 59. SEM micrograph of Specimen 11 failed under fatigue loading conditions with maximum stress of 100 MPa at 1330°C in air.

Figure 60. SEM micrograph of Specimen 16 failed under fatigue loading conditions with maximum stress of 50 MPa at 1330°C in steam.

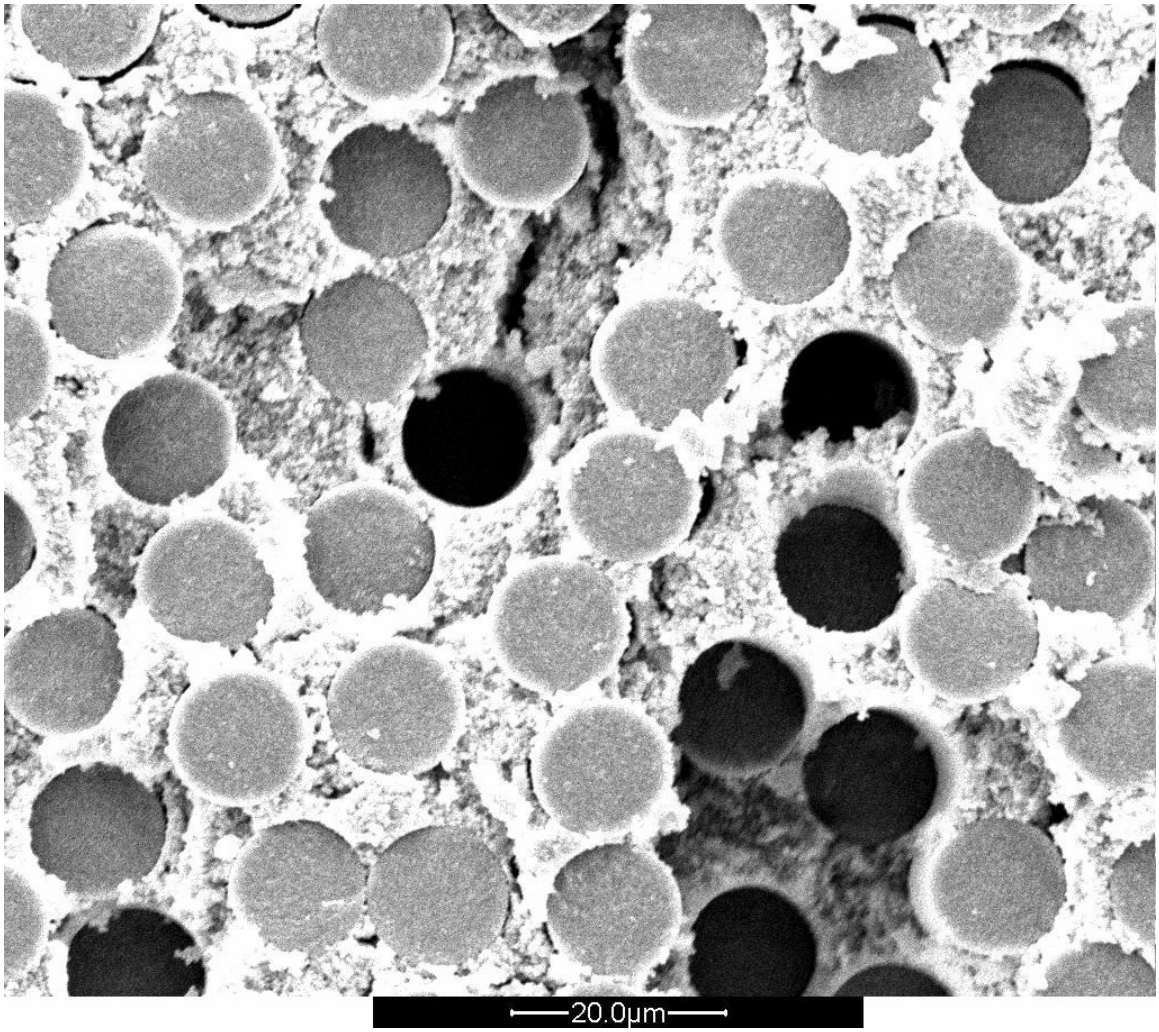

Figure 61. SEM micrograph of Specimen 16 failed under fatigue loading conditions with maximum stress of 50 MPa at 1330°C in steam.

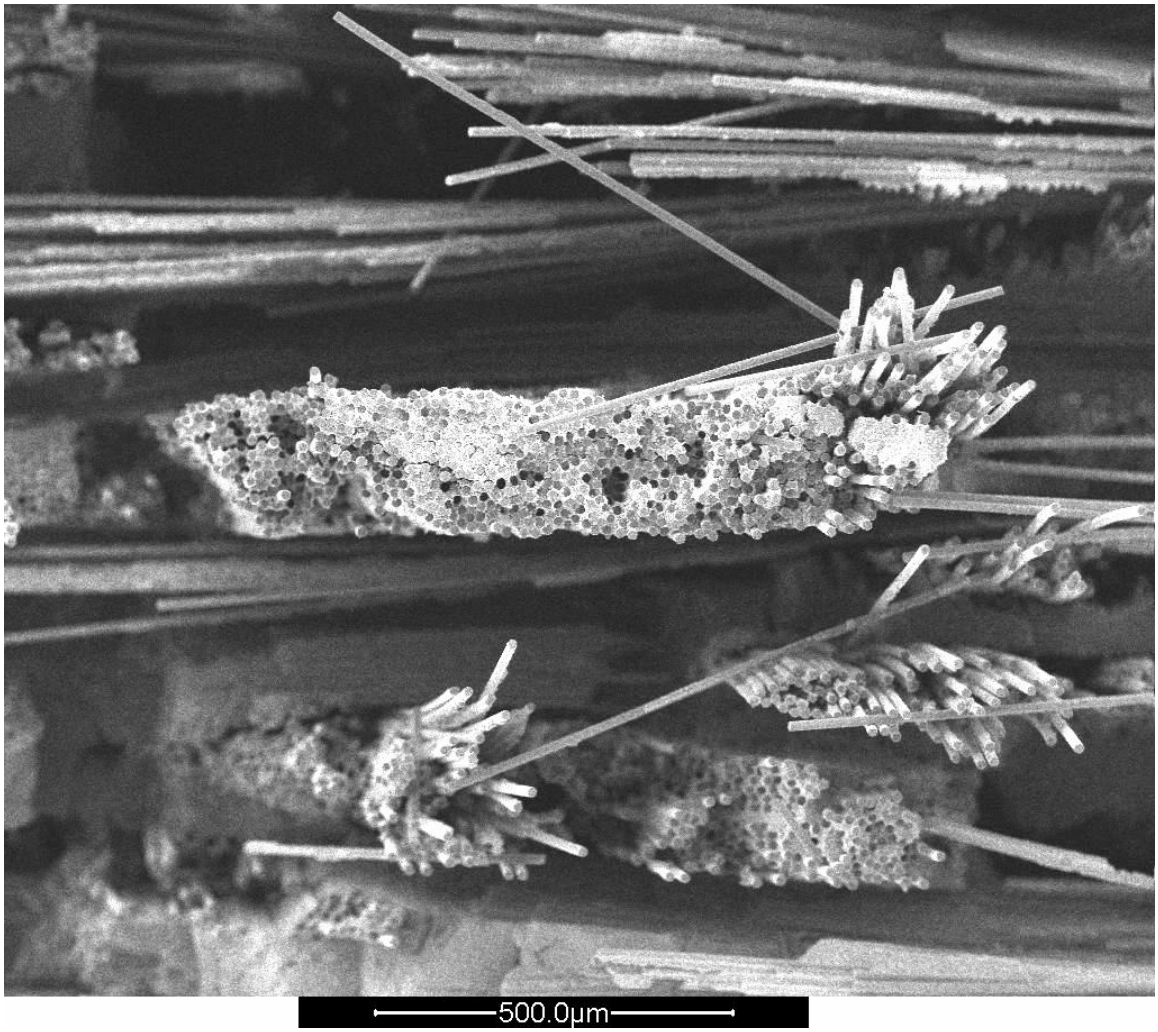

Figure 62. SEM micrograph of Specimen 17 failed under fatigue loading conditions with maximum stress of 100 MPa at 1330°C in steam.

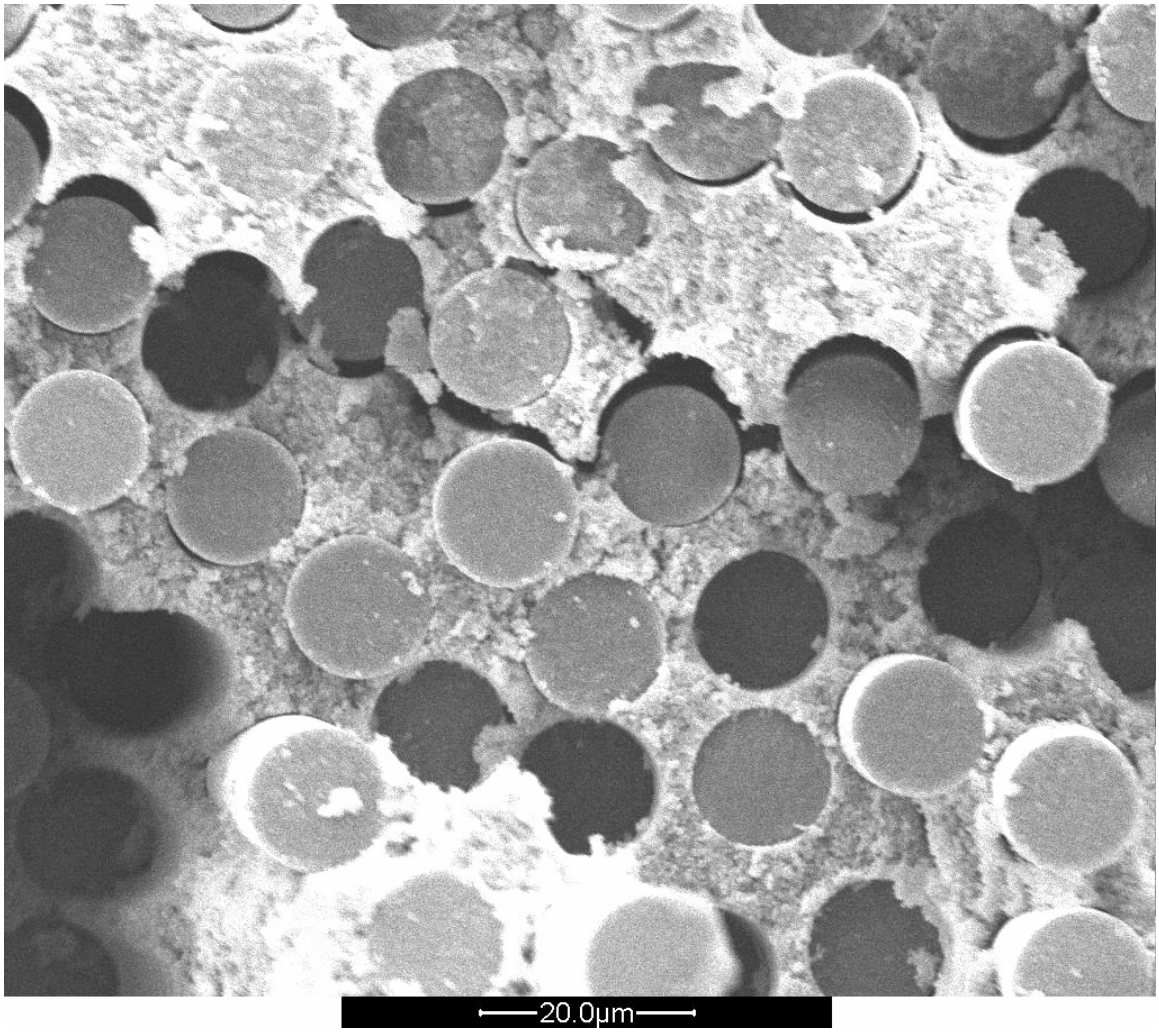

Figure 63. SEM micrograph of Specimen 17 failed under fatigue loading conditions with maximum stress of 100 MPa at 1330°C in steam.

Bibliography

1. Antti, M.-L., E. Lara-Curzio and R. Warren. “Thermal degradation of an oxide fibre (Nextel 720)/aluminosilicate composite,” *Journal of the European Ceramic Society*, 24:565-578 (2004).

2. Buchanan, Dennis J., Reji John and Larry P. Zawada. “Creep-Rupture Behavior of ±45° Oxide/Oxide Nextel 720/AS Composite,” *Ceramic Engineering and Science Proceedings*, 24[4], 451-458 (2003).

3. Casas, L. and J.M. Martínez-Esnaola. “Microstructural characterization of an alumina/mullite composite tested in creep,” *Materials Science and Engineering*, A368:139-144 (2004).

4. Chawla, K. K., *Ceramic Matrix Composites.* London: Chapman & Hall, 1993.

5. COI, unpublished data.

6. Dassios, Konstantinos G., Marc Steen, and Constantina Filiou. “Mechanical properties of alumina Nextel 720 fibres at room and elevated temperatures: tensile bundle testing,” *Materials Science and Engineering*, A349:63-72 (2003).

7. Engesser, John Mark. “Monotonic, Creep-Rupture, and Fatigue Behavior of Carbon Fiber Reinforced Silicon Carbide (C/SiC) at an Elevated Temperature,” AFIT Thesis AFIT/GMS/ENY/04-M01, (March 2004).

8. Harada, Yoshihisa, Takayuki Suzuki and Kazumi Hirano. “Influence of Moisture on Ultra-High-Temperature Tensile Creep Behavior of *in Situ* Single-Crystal Oxide Ceramic Alumina/Yttrium Aluminum Garnet Eutectic Composite,” *Journal of the American Ceramics Society*, 86[6], 951-958 (2003).

9. Haslam, J.J., K.E. Berroth and F.F. Lange. “Processing and properties of an all-oxide composite with a porous matrix,” *Journal of the European Ceramic Society*, 20:607-618 (2000).

10. Herakovich, Carl T. *Mechanics of Fibrous Composites.* New York: John Wiley & Sons, 1998.

11. Jacobson, Nathan S. “Corrosion of Silicon-Based Ceramics in Combustion Environments,” *Journal of the American Ceramics Society*, 76[1]:3-28 (1993).

12. Jacobson, Nathan and Serene Farmer. “High-Temperature Oxidation of Boron Nitride: I, Monolithic Boron Nitride,” *Journal of the American Ceramics Society*, 82[2], 393-398 (1999).

13. Jacobson, Nathan S. and Gergory N. Morscher. “High Temperature Oxidation of Boron Nitride: II, Boron Nitride Layers in Composites,” *Journal of the American Ceramics Society*, 82[6], 1473-1482 (1999).

14. Jenkins, Michael G. and Larry P. Zawada. “Elastic Modulus and Proportional Limit Stress in Ceramic Matrix Composites: Comparison of Methods and Results,” *Ceramic Engineering and Science Proceedings*, 22[3]:503-511 (2001).

15. Karandikar, Prashant G. and Tsu-Wei Chou. “Damage Development and Moduli Reduction in Nicalon-Calcium Aluminosilicate Composites under Static Fatigue and Cyclic Fatigue,” *Journal of the American Ceramics Society*, 76[7]:1720-1728 (1993).

16. Kaya, C., E.G. Butler, A. Selcuk, A.R. Boccaccini and R.H. Lewis. “Mullite (Nextel 720) fibre-reinforced mullite matrix composites exhibiting favourable thermomechanical properties,” *Journal of the European Ceramic Society*, 22:2333-2342 (2002).

17. Lee, S. Steven, Larry P. Zawada, James M. Staehler and Craig A. Folsom. “Mechanical Behavior and High-Temperature Performance of Woven Nicalon/Si-N-C Ceramic-Matrix Composite,” *Journal of the American Ceramic Society*, 81 [7]:1797-1811 (1998).

18. Lemaitre, Jean and Jean-Louis Chaboche. *Mechanics of Solid Materials*. Cambridge: Cambridge University Press, 1994.

19. Levi, Carlos G., James Y. Yang, Brian J. Dalgleish, Frank W. Zok and Anthony G. Evans. “Processing and Performance of an All-Oxide Ceramic Composite,” *Journal of the American Ceramic Society*, 81 [8]:2077-86 (1998).

20. More, Karren L., Peter F. Tortorelli, Mattison K. Ferber and James R. Keiser. “Observations of Accelerated Silicon Carbide Recession by Oxidation at High Water-Vapor Pressures,” *Journal of the American Ceramics Society*, 83[1]:211-0213 (2000).

21. Ogbuji, Linus U.J.T. “A Pervasive Mode of Oxidative Degradation in a SiC-SiC Composite,” *Journal of the American Ceramics Society*, 81[11]:2777-2784 (1998).

22. Opila, Elizabeth J. "Oxidation Kinetics of Chemically Vapor-Deposited Silicon Carbide in Wet Oxygen," *Journal of the American Ceramics Society*, 7[3]:730-736 (1994).

23. Opila, Elizabeth J. "Paralinear Oxidation of CVD SiC in Water Vapor," *Journal of the American Ceramics Society*, 80[1]:197-205 (1997).

24. Opila, Elizabeth J. "Variation of the Oxidation Rate of Silicon Carbide with Water-Vapor Pressure," *Journal of the American Ceramics Society*, 82[3]:625-636 (1999).

25. Parlier, Michel and M.H. Ritti. "State of the Art and Perspectives for oxide/oxide composites," *Aerospace Science and Technology*, 7:211-221 (2003).

26. Ruggles-Wrenn, M.B., J.M. Corum and R.L. Battiste. "Short-term static and cyclic behavior of two automotive carbon-fiber composites," *Composites: Part A*, 34, 731-741 (2003).

27. Sandor, Bela I. *Fundamentals of Cyclic Stress and Strain*. Madison: The University of Wisconsin Press, 1972.

28. Schmidt, S., S. Beyer, H. Knabe, H. Immich, R. Meistring, and A. Gessler. "Advanced ceramic matrix composite materials for current and future propulsion technology applications," *Acta Astronautica*, 55: 409-420 (2004).

29. Steel, Steven G. "Monotonic and Fatigue Loading Behavior of an Oxide/Oxide Ceramic Matrix Composite," AFIT Thesis AFIT/GMS/ENY/00M-02, (March 2000).

30. Steel, Steven G., Zawada, Larry P. and Shankar Mall. "Fatigue Behavior of a Nextel 720/Alumina (N720/A) Composite at Room and Elevated Temperature," *Ceramic Engineering and Science Proceedings*, 22[3]:695-702 (2001).

31. Tu, Wen-Chiang, Fred F. Lange and Anthony G. Evans. "Concept for a Damage-Tolerant Ceramic Composite with 'Strong' Interfaces," *Journal of the American Ceramics Society*, 79[2], 417-424 (1996).

32. Verilli, Michael J., Anthony M. Calomino and David N. Brewer. "Creep-Rupture Behavior of a Nicalon/SiC Composite," *Thermal and Mechanical Test Methods and Behavior of Continuous-Fiber Ceramic Composites, ASTM STP 1309,* American Society for Testing and Materials, 158-175 (1997).

33. Verrilli, Michael J., Elizabeth J. Opila, Anthony Calomino and J. Douglas Kiser. "Effect of Environment on the Stress-Rupture Behavior of a Carbon-Fiber-Reinforced Silicon Carbide Ceramic Matrix Composite," *Journal of the American Ceramic Society*, 87 [8]:1536-1542 (2004).

34. Wannaparhun, S., S. Seal and V. Desai. "Surface chemistry of Nextel-720, alumina and Nextel-720/alumina ceramic matrix composite (CMC) using XPS-A tool for nano-spectroscopy," *Applied Surface Science*, 185:183-196 (2002).

35. Wannaparhun, Surasak and Sudipta Seal. "Combined Spectroscopic and Thermodynamic Investigation of Nextel-720 Fiber/Alumina Ceramic-Matrix Composite in Air and Water Vapor at 1100°C," *Journal of the American Ceramic Society*, 86[9], 1628-1630 (2003).

36. Zawada, Larry P. "Longitudinal and Transthickness Tensile Behavior of Several Oxide/Oxide Composites," *Ceramic Engineering and Science Proceedings*, 19[3]:327-335 (1998).

37. Zawada, Larry P. and Shin S. Lee. "The Effect of Hold Times on the Fatigue Behavior of an Oxide/Oxide Ceramic Matrix Composite," *Thermal and Mechanical Test Methods and Behavior of Continuous-Fiber Ceramic Composites, ASTM STP 1309*, American Society for Testing and Materials, 69-101 (1997).

38. Zawada, Larry P., James Staehler and Steve Steel. "Consequence of Intermittent Exposure to Moisture and Salt Fog on the High-Temperature Fatigue Durability of Several Ceramic-Matrix Composites," *Journal of the American Ceramic Society*, 86 [8]:1282-1291 (2003).

Vita

1Lt Chalene Ann Eber graduated from W. J. Palmer High School in Colorado Springs, CO. She then entered the United States Air Force Academy and was commissioned with the Class of 2001 with a Bachelor of Science in Astronautical Engineering, with minors in Spanish and Mathematics.

Following graduation from the Academy, she was assigned to the Test and Evaluation Division of Detachment 9, Space and Missile Systems Center, at Vandenberg AFB, CA where she worked as a Launch Systems Test Engineer and Program Planning Manager. She enrolled at the Air Force Institute of Technology, studying Astronautical Engineering, in August of 2003. After completion of her Master of Science degree in March 2005, she will be assigned to the Air Force Research Laboratory, Space Vehicles Directorate, at Kirtland AFB, NM.

REPORT DOCUMENTATION PAGE

Form Approved
OMB No. 074-0188

1. REPORT DATE *(DD-MM-YYYY)*	**2. REPORT TYPE**	**3. DATES COVERED** *(From – To)*
21-03-2005	Master's Thesis	March 2004 – March 2005

4. TITLE AND SUBTITLE
Effect of Temperature and Steam Environment on Fatigue Behavior of an Oxide-Oxide Continuous Fiber Ceramic Composite

5a. CONTRACT NUMBER

5b. GRANT NUMBER

5c. PROGRAM ELEMENT NUMBER

6. AUTHOR(S)
Eber, Chalene A., First Lieutenant, USAF

5d. PROJECT NUMBER

5e. TASK NUMBER

5f. WORK UNIT NUMBER

7. PERFORMING ORGANIZATION NAMES(S) AND ADDRESS(S)
Air Force Institute of Technology
Graduate School of Engineering and Management (AFIT/EN)
2950 Hobson Way, Building 640
WPAFB OH 45433-7765

8. PERFORMING ORGANIZATION REPORT NUMBER
AFIT/GA/ENY/05-M09

9. SPONSORING/MONITORING AGENCY NAME(S) AND ADDRESS(ES)
Ruth Sikorski, AFRL/PRTC
1950 Fifth Street
Wright-Patterson AFB, OH 45433-7251
Phone: 937-255-7268

10. SPONSOR/MONITOR'S ACRONYM(S)

11. SPONSOR/MONITOR'S REPORT NUMBER(S)

12. DISTRIBUTION/AVAILABILITY STATEMENT
APPROVED FOR PUBLIC RELEASE; DISTRIBUTION IS UNLIMITED.

13. SUPPLEMENTARY NOTES

14. ABSTRACT

There is an ever-increasing need for materials that maintain high strength and fracture toughness at elevated temperatures and in complex environments. Advanced aerospace applications are motivating the development of composite materials that can meet demanding requirements. This research effort investigates mechanical behavior of an oxide-oxide continuous fiber ceramic composite (CFCC) consisting of a porous alumina matrix reinforced with mullite/alumina Nextel 720 fibers developed specifically for advanced aerospace applications. Tension-tension fatigue behavior of this CFCC was studied at 1200 and 1330°C in laboratory air and 100% steam environments. Fatigue resistance and retained strength properties were determined. Effects of environmental degradation was addressed in detail.

15. SUBJECT TERMS
ceramic composite, fatigue, temperature, steam, humidity

16. SECURITY CLASSIFICATION OF:			**17. LIMITATION OF ABSTRACT**	**18. NUMBER OF PAGES**	**19a. NAME OF RESPONSIBLE PERSON**
a. REPORT	**b. ABSTRACT**	**c. THIS PAGE**			Dr. Marina B. Ruggles-Wrenn, ENY
U	**U**	**U**	**UU**	107	**19b. TELEPHONE NUMBER** *(Include area code)* (937) 255-6565, ext 4641 (marina.ruggles-wrenn@afit.edu)

Standard Form 298 (Rev. 8-98)
Prescribed by ANSI Std. Z39-18